

PROCESS INTENSIFICATION THROUGH MULTIFUNCTIONAL REACTOR

CONCEPTS:

REVERSE-FLOW REACTOR AND NANOCOMPOSITE MATERIALS

by

Tengfei Liu

B.S. in Chemical Engineering, Tsinghua University, 1999

M.S. in Chemical Engineering, Tsinghua University, 2002

Submitted to the Graduate Faculty of
School of Engineering in partial fulfillment
of the requirements for the degree of
Doctor of Philosophy

University of Pittsburgh

2007

UNIVERSITY OF PITTSBURGH

SCHOOL OF ENGINEERING

This dissertation was presented

by

Tengfei Liu

It was defended on

February 21, 2007

and approved by

Professor Robert M. Enick, Chemical and Petroleum Engineering Department

Professor Irving Wender, Chemical and Petroleum Engineering Department

Professor Radisav D. Vidic, Civil & Environmental Engineering Department

Dissertation Director: Professor Götz Vesper, Chemical and Petroleum Engineering
Department

Copyright © by Tengfei Liu

2007

PROCESS INTENSIFICATION THROUGH MULTIFUNCTIONAL REACTOR

CONCEPTS:

REVERSE-FLOW REACTOR AND NANOCOMPOSITE MATERIALS

Tengfei Liu, PhD

University of Pittsburgh, 2007

Multifunctional reactor concepts can lead to significant process intensification by integrating more than one unit operation in one reactive system. The integration can occur at both reactor and catalyst / material levels.

In the first part of this thesis, we will demonstrate that heat-integration in a reverse-flow reactor (RFR) can successfully overcome thermodynamic limitations during autothermal reactor operations for catalytic partial oxidation of methane (CPOM) and autothermal reforming (ATR) and results in significantly increased syngas and particularly hydrogen yields; significantly increased reactor throughput as well as significantly increased autothermal reactor operation ranges. Furthermore, although RFR operates at higher temperatures than steady state (SS) operation, it leads to an intrinsic compensation for catalyst deactivation.

In the second part of this thesis, we will report the development of novel nanostructured oxygen carriers. Using a microemulsion-templated sol-gel synthesis route, metal-alumina nanocomposite materials (Me-BHA) were prepared and evaluated in comparison with conventionally prepared Bentonite-based oxygen carriers. Ni-, Fe-, and Cu-based nanocomposites were synthesized, characterized, and evaluated in TGA and reactor studies using a coal-derived syngas as model fuel. Nanostructuring of the oxygen carrier leads to a drastic

acceleration of the oxidation kinetics in Ni- and Fe- based carriers, but only weakly accelerated kinetics for Cu-based materials. The embedding of the nanosized metal particles by the ceramic supports also overcome sintering problems and make these oxygen carriers particularly stable at high temperature applications.

Overall, in both cases, we will demonstrate that process intensification goals can be well achieved via the integrated reactor concepts in a reactive system (reactor level and material level).

TABLE OF CONTENTS

ACKNOWLEDGEMENTS	XV
1.0 INTRODUCTION.....	1
1.1 SYGAS / HYDROGEN PRODUCTION FROM METHANE	3
1.2 FUNDAMENTALS OF REVERSE FLOW REACTOR.....	10
1.3 CHEMICAL LOOPING COMBUSTION (CLC)	12
2.0 CPOM MECHANISM.....	16
2.1 LITERATURE REVIEW	16
2.2 EXPERIMENTAL.....	18
2.3 RESULTS	20
2.3.1 Variation of catalyst length	20
2.3.2 Effect of contact time	23
2.4 DISCUSSIONS.....	29
2.4.1 Effect of gas flow rate	30
2.4.2 Effect of CH₄ to O₂ ratio.....	35
2.4.3 Catalyst deactivation	37
2.5 SUMMARY AND CONCLUSIONS	39
3.0 REVERSE FLOW REACTOR (RFR) OPERATION	42
3.1 EXPERIMENTAL.....	42

3.2	RESULTS AND DISCUSSION	44
3.2.1	Dynamic temperature profiles inside the catalyst and inert zones.....	44
3.2.2	Influence of flow rate on temperature profiles.....	49
3.2.3	Compensation for catalyst deactivation.....	53
3.3	SUMMARY	58
4.0	AUTOTHERMAL REFORMING (ATR) IN A RFR	60
4.1	THERMODYNAMICS	61
4.2	EXPERIMENTAL	67
4.2.1	Experimental setup	67
4.2.2	Reactor safety	68
4.3	RESULTS AND DISCUSSION	69
4.3.1	Variation of H ₂ O addition	69
4.3.2	Variation of O ₂ /CH ₄ ratio.....	71
4.3.3	H ₂ yields	72
4.3.4	H ₂ /CO ratio.....	74
4.3.5	Variation of τ and flow rate	76
4.3.6	ATR Mechanism	78
4.3.7	Autothermal reforming economics.....	79
4.4	SUMMARY	80
5.0	NANOCOMPOSITE OXYGEN CARRIERS FOR CHEMICAL LOOPING COMBUSTION (CLC)	81
5.1	EXPERIMENTAL	82
5.1.1	Synthesis and characterization of oxygen carriers	82
5.1.2	Reactive evaluation	84

5.2	RESULTS AND DISCUSSION	85
5.2.1	TEM	85
5.2.2	XRD	86
5.2.3	BET and pore structure	89
5.2.4	Reactive test.....	93
5.2.5	Shrinking core model.....	97
5.2.6	High temperature stability	105
5.2.7	Results on other metals.....	109
	5.2.7.1 Fe-BHA	109
	5.2.7.2 Cu-BHA	111
	5.2.7.3 Co-BHA	117
5.3	SUMMARY	118
6.0	SUMMARY AND OUTLOOK.....	121
6.1	SUMMARY	121
6.1.1	Syngas / hydrogen production in a reverse-flow reactor (RFR).....	121
6.1.2	Nanocomposite oxygen carriers for chemical looping combustion (CLC)	123
6.2	OUTLOOK.....	124
6.2.1	Mass transfer studies during CPOM	124
6.2.2	Higher weight loading oxygen carriers	124
6.2.3	Integrating RFR concept with CLC	125
	APPENDIX A	127
	APPENDIX B	128

APPENDIX C	129
APPENDIX D	131
BIBLIOGRAPHY.....	135

LIST OF TABLES

Table 1. Calculated mol numbers based on the steam reforming and water gas shift pathway from $\tau = 4$ ms to $\tau = 7.7$ ms	26
Table 2. Relative errors of the calculated concentrations based on the steam reforming and water gas shift pathway and the experimental results over the contact time shown in Figure 8. The amount of H ₂ produced from steam reforming is also shown in the last row as percentages.	27
Table 3. BET surface area of Ni-Bentonite samples and Ni-BHA samples.	92
Table 4. Rate limiting cases for shrinking core model.	100
Table 5. Summary of comparative evaluation of a ‘conventional’ Ni-bentonite carrier and nanocomposite Ni-BHA carriers with different weight loadings.	102
Table 6. Summary of comparative evaluation of a ‘conventional’ Cu-Bentonite carrier and nanocomposite Cu-BHA carriers.	113
Table 7. Summary of nanocomposite oxygen carriers.	119
Table 8. A typical receipee for Ni_BHA oxygen carrier synthesis. The synthesis results in 15.31 wt% (theoretical) NiO loading.	128

LIST OF FIGURES

Figure 1. Summary of methane conversions.....	4
Figure 2. Thermodynamic calculations of syngas yields as a function of temperature. The initial gas mixture is $\text{CH}_4/\text{O}_2 = 2$ in methane/air system at 1 atm.....	7
Figure 3. A schematic diagram of a counter-current heat exchange reactor (CHXR).....	8
Figure 4. Schematic of regenerative heat exchange in an RFR: Temperature profiles along the reactor axis z during one semicycle (clockwise from top left).	11
Figure 5. Schematic of chemical looping combustion (CLC).	14
Figure 6. Cordierite monoliths with 2 mm, 5 mm, and 10 mm length before and after impregnation with Pt.....	19
Figure 7. Temperature profiles inside the catalyst (left graph) for a 2 mm (squares), 5mm (circles) and a 10 mm (triangles) long catalyst along with the corresponding values for S_{CO} (triangles), S_{H_2} (circles), X_{CH_4} (squares) and X_{O_2} (diamonds) (right graph).	21
Figure 8. Relative concentrations of the reactants and main products as a function of catalyst contact time (left). The right graph shows the data for the first 4 ms together with one data point at extremely short contact time (0.21ms) taken from ref [48] (close symbols).	24
Figure 9. Temperature profiles inside the 10 mm catalyst (left graph) at different inlet gas flow rate along with the corresponding values for S_{CO} (triangles), S_{H_2} (circles) and X_{CH_4} (squares) (right graph).	31
Figure 10. Q/K_{eq} as a function of flow rate. Q is calculated based on exit concentrations, K_{eq} is the reaction equilibrium constant corresponding to the catalyst exit temperature.....	33
Figure 11. Temperature profiles (left) and corresponding CH_4 conversion (right, square), H_2 selectivity (right, circle) and CO selectivity (right, triangle) on 10 mm Pt catalyst at different inlet CH_4/O_2 ratios. Total flow rates were 4 slm, and the vertical lines mark the start and the end of the catalyst.	36

Figure 12. Left: Temperature profiles on the fresh (squares) and aged (circles) 10 mm Pt catalyst. Right: S_{CO} (triangles), S_{H_2} (circles) and X_{CH_4} (squares) as a function of time on stream.....	38
Figure 13. Schematic of the experimental reverse-flow reactor system used for investigating the partial oxidation of methane.	43
Figure 14. Spatio-temporal temperature profiles inside the catalyst ($z = 0-10\text{mm}$) and one inert zone during four half-periods (i.e. four flow reversals) for a flow reversal half-period of 2 s, 25s and 100s, respectively (clockwise from top left). The bottom left g graph shows the corresponding methane conversion (circles), H_2 selectivity (triangles) and CO selectivity (squares) as a function of periodicity. $CH_4/O_2 = 2$ in methane air system.	46
Figure 15. Dynamic temperature profiles in the catalyst and inert zones during one semi-cycle upon flow switch in RFR operation. The flow rate is 2 slm with $CH_4/O_2 = 2$ in methane/air system, $\tau/2 = 25\text{s}$	47
Figure 16. CH_4 conversion (X_{CH_4} left), H_2 selectivity (S_{H_2} middle), and CO selectivity (S_{CO} , right) as a function of the total volumetric gas flow rate for steady-state (SS, open symbols) and RFR (solid symbols) operation.	50
Figure 17. Temperature profiles in two full cycles on the Pt catalyst and one inert zone at 1 slm (left) and 2 slm (right) at RFR operations, $CH_4/O_2 = 2$ in methane/air system, $\tau/2 = 25\text{ s}$	52
Figure 18. Catalyst deactivation at SS operation vs. RFR operation: methane conversion and syngas selectivities are shown vs. time on stream while switching between SS reactor operation (cross symbols and dotted lines) and RFR operation (close symbols and solid lines) for the Pt catalyst. Inlet gas composition was $CH_4/O_2=2$ in methane/air system at a total inlet gas flowrate of 4 slm, $\tau/2=15\text{s}$	54
Figure 19. Temperature profile on the fresh and aged Pt catalyst at 1slm at SS operations. The deactivation was operated at total flowrate 4slm, $CH_4/O_2=2$ in methane/air system for 6 hours. 55	
Figure 20. Temperature profile on the fresh and aged Pt catalyst at 1slm at RFR operations. The deactivation was operated at 4slm, $CH_4/O_2 = 2/1$ in methane/air system, $\tau/2=15\text{s}$ for 6 hours.....	57
Figure 21. Thermodynamic calculations of hydrogen yield as a function of H_2O/CH_4 and isothermal temperature. Dashed line - adiabatic temperature of the system started at 100°C	62
Figure 22. Thermodynamic calculations for adiabatic temperature (T), top left, methane conversion (X_{CH_4}), top right, H_2 selectivity (S_{H_2}), bottom left and CO selectivity (S_{CO}), bottom right as function of O_2/CH_4 and H_2O/CH_4 ratios.	63
Figure 23. Thermodynamic calculations for hydrogen yields (left) and concentration (in molar fraction) in the equilibrated gases.	64

Figure 24. Thermodynamic calculations for adiabatic equilibrated H ₂ /CO ratios upon water additions.....	66
Figure 25. Thermodynamic calculations for adiabatic equilibrated H ₂ /CO ratios upon CO ₂ additions.....	67
Figure 26. Methane conversion (square, left), hydrogen selectivity (circle, middle) and CO selectivity (triangle, right) as a function of water addition at both SS (open symbols) and RFR (closed symbols) operations. CH ₄ /O ₂ ratio was kept at 3, the inlet gas (CH ₄ + O ₂ + H ₂ O) flow rate was 2 slm.....	70
Figure 27. Methane conversion (square, left), hydrogen selectivity (circle, middle) and CO selectivity (triangle, right) as a function of O ₂ /CH ₄ at both SS (open symbols) and RFR (closed symbols) operations. H ₂ O/CH ₄ ratio was kept at 2, the inlet gases (CH ₄ + O ₂ + H ₂ O) flow rate was 2 slm.....	72
Figure 28. H ₂ yields at SS (left) and RFR (right) operations. O ₂ /CH ₄ ratio was changed from 0.25 to 0.6; H ₂ O/CH ₄ ratio was changed from 0 to 4. Total inlet gases flow rate was 2 slm and the flow reversal switching period in RFR was $\tau/2 = 25s$	74
Figure 29. Comparison of product syngas H ₂ /CO ratio at SS (blue surface) and RFR (red surface) operations. O ₂ /CH ₄ ratio was changed from 0.25 to 0.6; H ₂ O/CH ₄ ratio was changed from 0 to 4. Total inlet gases flow rate was 2 slm and the flow reversal switching period in RFR was $\tau/2 = 25s$	75
Figure 30. Left: Hydrogen yields at SS operations (horizontal lines) and RFR operations at different flow rate (1slm – 3slm) and different flow reversal switching periods ($\tau/2$). The feed gas composition was O ₂ /CH ₄ /H ₂ O = 0.5/1/2. Right: Temperature at catalyst entrance and exit during SS operations as well as average temperature at catalyst ends during RFR operations at different flow rates. The flow reversal switching period ($\tau/2$) was 25 seconds and the feed gas composition was O ₂ /CH ₄ /H ₂ O = 0.5/1/2.	76
Figure 31. Synthesis schema of nanocomposite oxygen carriers.	84
Figure 32. TEM images of Ni-BHA (15wt%, upper left, 26wt%, upper right) and Ni-Bentonite (lower).....	86
Figure 33. XRD spectra for a 15wt% Ni-BHA nanocomposite sample after oxidation (top) and reduction (bottom).	88
Figure 34. XRD spectra for 15wt%, 26 wt% and 37wt% Ni-BHA nanocomposite samples.	89
Figure 35. N ₂ adsorption isotherm for Ni-BHA and Ni-Bentonite.....	90
Figure 36. BJH pore structure for Ni_BHA and Ni_Bentonite.	91

Figure 37. Results from cyclic-TGA for a ‘conventional’ 60wt% Ni-bentonite sample (top) and a nanocomposite 15wt% Ni-BHA nanocomposite sample (bottom). Sample weight is shown versus time.	93
Figure 38. Overlay of a single redox cycle from TGA experiments at 800°C for a nanocomposite carrier (‘Ni-BHA’) and a ‘conventional’ carrier (‘Ni-Bentonite’).	95
Figure 39. Schematic of shrinking core model.	99
Figure 40. A typical fitting result for the experimental data (circle points) with three fitted lines based on different controlling mechanisms.	101
Figure 41. τ as a function of Ni weight loading during the oxidation of Ni-BHA samples at 800°C.	104
Figure 42. TGA reactive evaluations for Ni-BHA with 37wt% NiO loading at 900°C and Ni-Bentonite sample with 20 mesh particle size and 60wt% NiO loading at 700, 800 and 900°C respectively.	107
Figure 43. TGA reactive evaluations for 20, 30, 60 and 200 mesh Ni-Bentonite carriers with 60wt% NiO loading at 900°C.	108
Figure 44. Results from cyclic-TGA for 16wt% Fe-BHA nanocomposite sample. A single redox cycle result is shown in the upper graph.	110
Figure 45. Comparison of re-oxidation kinetics for Fe-BHA (16wt%) and Fe-Bentonite (60wt%) at 800°C.	111
Figure 46. Comparison of a single redox cycle from TGA experiments at 800°C for a nanocomposite carrier Cu-BHA and a conventional Cu-Bentonite.	112
Figure 47. Oxygen diffusivity in different metal oxides at different temperatures (adapted from I. Gallino, Ph.D. thesis, Oregon State, 2003).	114
Figure 48. Ellingham diagram for Ni, Fe, Cu and Co oxidation reactions.	115
Figure 49. Principle of RFR_CLC.	126

ACKNOWLEDGEMENTS

I would foremost like to thank my advisor Dr. Götz Vesper for his constant support, the important, detailed and inspiring discussions about my work and his exceptionally friendly and personal way of leading the research group. It has been an absolute pleasure working in his group.

I would also like to thank my lab mates Dirk, Tom, Katie, Sudipta, Anthony, Venessa, Michael, Cynthia and Hakan for the fun we had in the lab, which made work more productive and enjoyable.

Furthermore, I would like to thank Dr. Ranjani Siriwardane, Dr. Thomas Simonyi and Dr. Karuna Chaudhari from DOE – NETL for their support, collaboration and invaluable discussions. Financial support from DOE – NETL is also gratefully acknowledged.

In addition, I would like to thank the faculty, staff and students of the Chemical Engineering Department and Material Science Department at the University of Pittsburgh for their friendly support and help and for the fun we had during my stay in Pittsburgh.

A big hug and kiss to my parents, my sister and brother and Yanping for their love and support all the time.

1.0 INTRODUCTION

Process intensification generally denotes a trend in the chemical industry towards more efficient and sustainable processes [1-3]. Although there is no universally accepted definition of process intensification, increased process conversion and/or selectivity, reduced energy consumption and/or byproduct formation, decreased equipment size as well as environmental concerns are usually emphasized.

Multifunctional reactors (or reactive systems) allow a unique way to achieve process intensification goals. By definition, a multifunctional reactor integrates several functions (e.g. unit operations) in a single reactor vessel. The integration typically modifies temperature and/or concentration profile in the reactor to a desired one that leads to process intensification goals[3].

Multifunctional reactors are not new to the chemical industry. An example that has been widely applied in industry is catalytic distillation (or reactive distillation), where distillation is integrated with reaction in a reactor column. The reaction heat is used to distill the products to leave the reaction zone, which breaks the thermodynamic limitation (e.g. reaction equilibrium) of the reaction and hence drives the reaction towards more product formation. Another widely acknowledged example is the membrane reactor, where reaction is integrated with selective membrane separation. Again, the membrane selectively separates one of the products, therefore breaks the thermodynamic limitation of the reaction and leads to more product formation. In a more general classification by Dautzenberg and Mukherjee[2], considering the scale where

multifunctionality operates, multifunctional reactor ranges from individual catalyst particles to inter-connected reactors. According to this definition, bi-functional catalysts (metal-acid catalysts) and Fluid Catalytic Cracker (FCC) are also multifunctional reactors. In a typical bi-functional metal-acid catalyst, metallic sites and acid site are incorporated and they are responsible for the catalyzing of different reactions. The different active sites are ‘engineered’ to get optimal product yields. While the FCC integrates and optimizes reaction, catalyst regeneration, heat transfer, solid transportation etc. into a whole dynamic reaction – regeneration system.

Typical scenario toward process intensification via multifunctional reactors involves the following steps:

(1) Understanding the reaction. This includes the basic studies of the reaction mechanism, thermodynamics, kinetics as well as transport.

(2) Identifying the process limitations. Different processes may have different limitations, such as kinetic limitations, thermodynamic limitations, transport limitations etc. This step is to spot the bottleneck of the process.

(3) Overcoming the process limitations through engineering principles, such as improving catalyst design for fast kinetics, breaking thermodynamic limitations, increasing heat/mass transfer etc.

This thesis aims at achieving process intensification goals based on the integrated reactor concept. The reactions we look at are catalytic partial oxidation (CPOM), autothermal reforming (ATR) for the production of synthesis gas (syngas) and hydrogen and chemical looping combustion (CLC) for clean coal/natural gas fired power generation. For CPOM and ATR, we will demonstrate that thermodynamic limitations during autothermal operations can be

successfully overcome via heat-integration in a reverse-flow reactor (RFR). For CLC, we will demonstrate that sintering and slow kinetics that associated with conventionally prepared oxygen carriers can be overcome via nanostructuring of the oxygen carriers.

1.1 SYGAS / HYDROGEN PRODUCTION FROM METHANE

Natural gas is gaining increasing attention due to the unpredictable production of oil. Methane is the main component (~95%) of natural gas. Methane can be converted either directly (i.e. in a one step process) or indirectly (via several steps) into many downstream chemicals. Fig. 1 summarizes some methane utilization routes that have been investigated[4]. It should be pointed out that the direct conversion is still studied at a fundamental level and results in low reaction yields. At this time, the only economically available route for the conversion of methane into more valuable chemicals is via synthesis gas (or syngas, a H₂-CO mixture), followed by different processes to manufacture the desired chemical [5]. While the production of syngas is a required step in the indirect conversion of methane, it is also responsible for a large part of the total investment costs in a large scale industrial plant. Therefore, much research has been devoted to the improvement and development of novel, more efficient processes for the conversion of methane to syngas.

Syngas can be produced from methane via three reactions, steam reforming, dry reforming (or CO₂ reforming) and partial oxidation. To date, the only large-scale process for natural gas conversion is the endothermic reaction known as steam reforming (SRM, Eq. (1)) which is also the major route for the production of H₂:



In SRM, methane is converted with water over Ni catalysts in a strongly endothermic reaction to yield H₂/CO in a molar ratio of 3. The process is conducted in large tubular reformers to achieve high temperatures needed for considerable syngas yields, making steam reforming a major energy consumer. The resulting H₂/CO ratio 3 is not desired for downstream processes where mostly H₂/CO at 2 are favored (e.g. methanol and Fischer-Tropsch syntheses[5]). Therefore, the steam reformer is typically followed by an additional water gas shift (Eq. (2)) reactor to adjust the H₂/CO ratio to the desired value:



As the residence times inside the reactors lie in the range of 1s, large reactor volumes are necessary for high reactor throughputs.

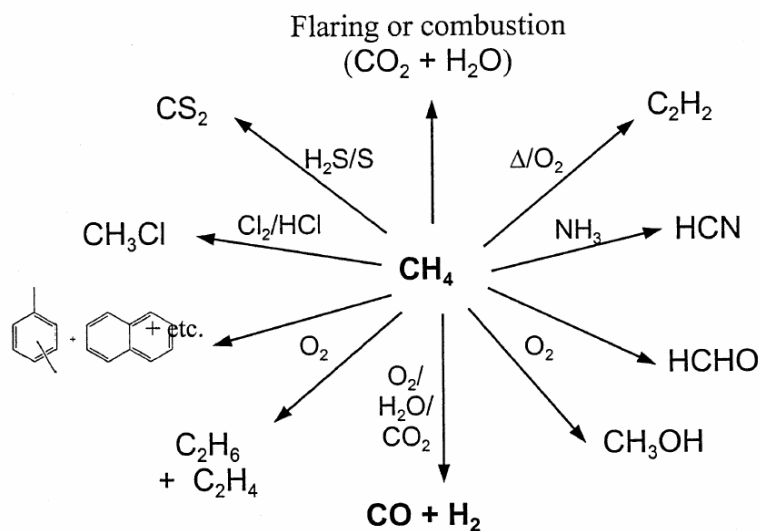


Figure 1. Summary of methane conversions

An alternative process for syngas formation is the exothermic methane partial oxidation, first investigated as early as 1946 by Prettre et al. [6]. In this process, methane is converted with oxygen or air to form H₂ and CO at a ratio of 2 (Eq. (3)) in a one step reaction:



Due to the mild exothermicity of the partial oxidation, this reaction can be conducted autothermally. Furthermore, the H₂/CO ratio of 2 is ideal for most downstream process, making partial oxidation of methane a simple, one-step process. A non-catalytic partial oxidation process was developed by Texaco and Shell which results in high syngas yields at high temperature and pressures [7]. Problems related to the homogeneous process are excessive temperatures, long residence times as well as excessive coke formation, which strongly reduce the controllability of the process. Catalytic partial oxidation of methane (CPOM) thus gains more attention. In this process, methane is converted with oxygen or air over noble metal catalysts (Pt, Rh, Ir) to syngas in a simple, one step reaction. The system is characterized by very high autothermal temperatures exceeding 1000 °C, which results in very high reaction rates and hence very high space-time yields. The contact time needed for CPOM is extremely short, $\tau = 1\sim 50\text{ms}$, several orders of magnitude shorter than steam reforming. The exothermicity of the reaction renders expensive external heating unnecessary. All these advantages allow compact and economic (low energy consumption) reactors feasible, which promotes a decentralized natural gas utilization and syngas (or hydrogen) production, and make it a promising technology for the upcoming gas economy.

CPOM has been studied extensively during the past decade. Many studies have focused on the reaction mechanism [4,8]; reactor configurations [9-14]; reactor simulations [15,16] as

well as novel catalyst synthesis [17,18] to improve the process (i.e. increase reaction yields) efficiency.

Thermodynamic calculations for methane/air mixture show that high autothermal temperatures in excess of 1000 °C are necessary to obtain optimum syngas yields (see Fig. 2). However, due to the mild exothermicity ($\Delta H_r = -36$ kJ/mol) of POM, it only causes an adiabatic temperature rise of 240 K. The adiabatic temperature denotes a temperature a reaction system can reach autonomously, without heat input or removal, i.e. all the reaction heat is used to cause the system temperature rise. In order to achieve the required high temperature (>1000°C), some of the methane feed has to be combusted via total oxidation:



The adiabatic temperature rise caused by reaction (4) is ~2000K. The reaction yield is thus ultimately determined by a complex interplay between partial oxidation and total oxidation reactions. While the combustion of methane results in high adiabatic temperature rise necessary for optimal syngas yields, the combustion products are by definition detrimental to syngas selectivities. Thus, the interaction between partial and total oxidation reactions limits obtainable syngas yields under autothermal operations.

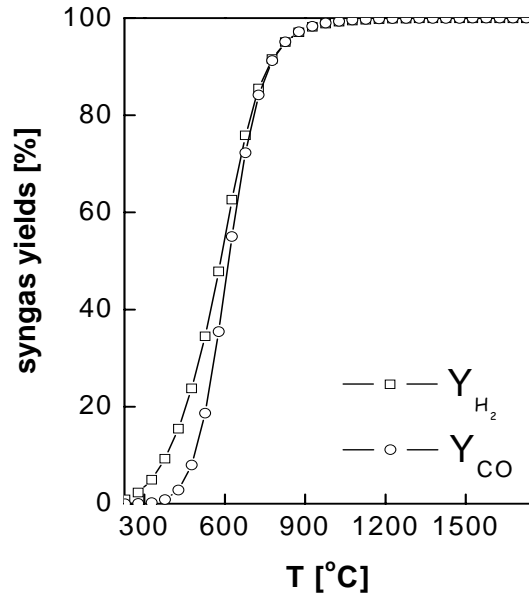


Figure 2. Thermodynamic calculations of syngas yields as a function of temperature. The initial gas mixture is $\text{CH}_4/\text{O}_2 = 2$ in methane/air system at 1 atm.

Initial investigations of CPOM by Hickman and Schmidt [19] showed that preheating of the reactants indeed results in increased syngas yields. While external preheating can be realized easily in a laboratory scale set-up, it is expensive and hence not economical in industrial applications. A much more efficient way is to re-use the sensible heat leaving the reaction zone in a multifunctional reactor concept [12]. Friedle and Vesper [10] observed enhanced syngas selectivities in a counter-current heat exchange reactor (CHXR, with the schematic diagram shown in Fig. 3). In this reactor configuration, the reactant gas is continuously fed through the inner tube of the reactor; the exit hot gas in the annular tube is used to heat up the feed gas in the inner tube. An even more efficient heat-integration (compared to the recuperative heat-exchange

in CHXR) reactor is achieved by regenerative heat-exchange in a dynamically operated reverse-flow reactor (RFR) [1,9,13,14]. In this reactor configuration, the flow-direction is periodically switched; heat generated from the reaction is efficiently integrated into the catalyst through the solid-state reservoirs placed on either side of the catalyst bed upon flow switching, instead of being simply effused from the reactor at steady state operations. Enhanced temperatures are achieved inside the catalyst, which is favorable for the syngas production. Significant process improvement was observed in RFR over steady-state (SS) operation. The improvement was shown to be solely an effect of heat integration, independent of the different mechanism or kinetics on a specific catalyst [9].

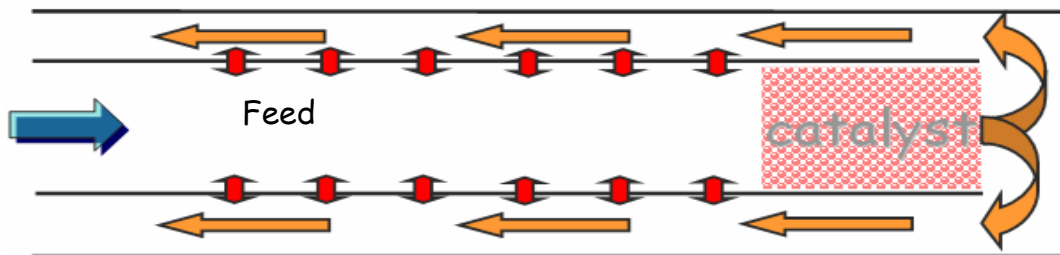


Figure 3. A schematic diagram of a counter-current heat exchange reactor (CHXR).

Engineering problems such as heat and mass transfer control, reactor optimization and reactor simulation as well as catalyst improvement all require a clear understanding of the mechanisms. However, much debate exists in the scientific community whether the syngas is produced through a direct partial oxidation (DPO) mechanism (Eq. (3)) or rather an indirect one,

in which methane is first converted to carbon dioxide and H₂O through combustion (Eq. (4)) and then syngas is produced by steam reforming (Eq. (1)), CO₂ (dry) reforming (Eq. (5)) and water gas shift reactions (Eq. (2)):



Unfortunately, the extreme reaction conditions as well as the intricate interplay between total oxidation and partial oxidation complicate the development of an understanding of the reaction mechanism. Due to the high reaction exothermicity and extreme temperature gradient of up to 10⁶ K/m on the catalyst, isothermal conditions which are necessary for conventional kinetics studies can not be achieved. Despite many years of intense research on this reaction, the reaction mechanism for CPOM at high-temperature millisecond contact time conditions is therefore still unresolved.

Starting from understanding the reaction process, in chapter 2, we developed an *in-situ* reaction mechanism on the Pt monolith catalyst for CPOM. Then in chapter 3, we studied the heat integration through dynamic temperature measurements at RFR operation and showed that this reactor configuration is particularly beneficial for the short contact time conditions of CPOM. We also studied the performance of different catalysts at RFR operations and found this reactor configuration leads to an intrinsic compensation for catalyst deactivation. Later in chapter 4, we extended reverse flow reactor operations to autothermal reforming for the production of hydrogen.

1.2 FUNDAMENTALS OF REVERSE FLOW REACTOR

The improvement of reactor performance by integrating several unit operations into a single reactor vessel has distinct advantages over the conventional sequential arrangement such as higher efficiency and lower cost. These so called multifunctional reactor concepts have been an intense research topic in the last two decades. One frequently used multifunctional reactor concept incorporates the integration of heat released by an exothermic reaction either by recuperative heat-exchange in a countercurrent heat-exchange reactor [10] or by regenerative heat-exchange in a reverse-flow reactor (RFR) [9,13,14]. The highly efficient heat-integration in the RFR makes it a particularly suitable reactor configuration for a process which is limited by the adiabatic temperature rise.

Matros and coworkers [20,21] performed pioneering work on the reverse-flow reactor concepts, which has been implemented in industry for SO₂ oxidation. Further large-scale applications have been realized in the incineration of waste gases [22]. Several studies have also been carried out on the production of sulfur in the Claus process [3,23,24], the production of HCN [3,23] as well as methane reforming [3].

In a typical RFR configuration, inert packing materials, so called inert zones, are placed on either side of the catalyst and act as regenerative heat exchanges in addition to the catalyst bed. Fig. 4 shows a schematic of the temperature profile along the reactor axis in a RFR at operating conditions. Cold reactants enter the catalyst bed and react exothermically on the catalyst surface. Hot product gases exit the reaction zone and exchange heat with the inert zone downstream of the catalyst. (Fig. 4, panel 1, $t=0$). In panel 2, the flow direction is reversed and cold reactants enter the reactor and exchange heat with the hot inert zone that has already been heated up, which is now located upstream of the catalyst. The reactants enter the catalyst bed in

an elevated temperature, which adds to the heat of reaction and leads to an overall increase of the catalyst temperature. (Fig. 4 panel 2, previous temperature profiles are represented by the dashed line). Hot product gases exit the reaction zone and exchange heat with the cold inert zone downstream of the catalyst bed. The continuous heat exchange now leads to a cooling of the heat reservoir upstream and a heating of the heat reservoir downstream of the catalyst (Fig. 4 panel 3-4).

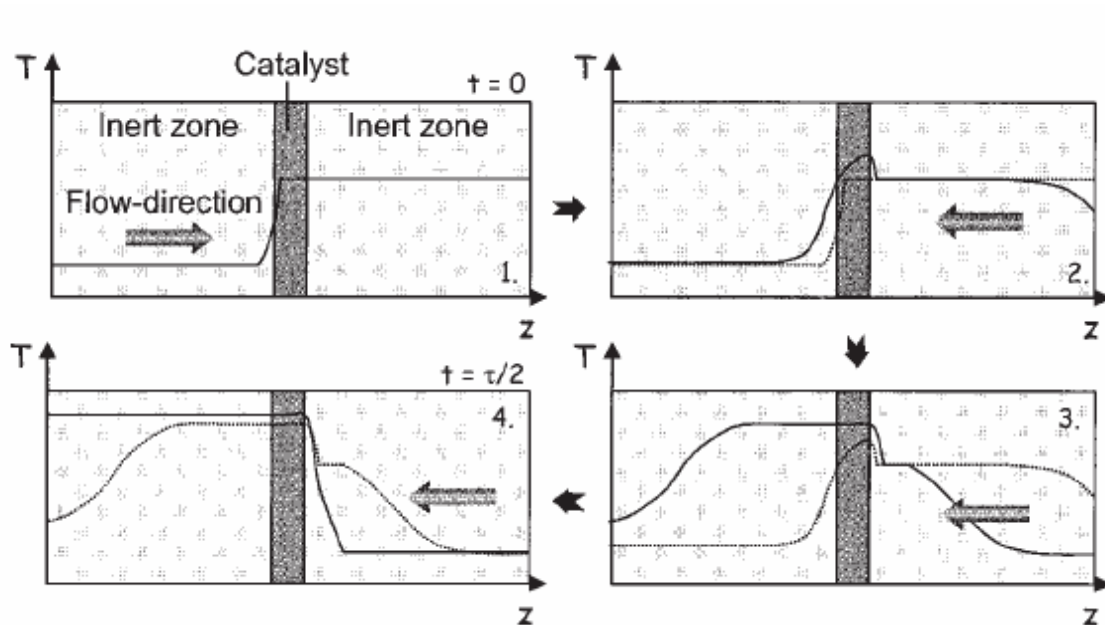


Figure 4. Schematic of regenerative heat exchange in an RFR: Temperature profiles along the reactor axis z during one semicycle (clockwise from top left).

Once the inert zone upstream has been cooled down, the flow is reversed periodically (with $t = \tau/2$, where $\tau/2$ denotes the duration of one half-period, the time during which the gas flows in one direction only), resulting in a very efficient heat integration. If the flow reversals are

repeated frequently enough, the characteristics (temperatures, product concentrations) of a full cycle are identical to the preceding one and the system has reached the so-called periodic steady state.

In addition to regenerative heat-exchange, dynamic reactor operation also leads to transient surface coverage changes by a temporal distribution of the feed gas. Upon each flow switching, the catalyst entrance which was the exit in the previous semi-cycle is exposed to an oxygen rich gas stream as well as an elevated temperature. The dynamic temperature as well as temporal stream concentration profile both contributes to the increased process efficiency in the RFR, which will be discussed in detail in Chapter 3.

1.3 CHEMICAL LOOPING COMBUSTION (CLC)

The dynamic reactor operation in a RFR integrates reaction with regenerative heat exchange. The efficient heat-integration breaks thermodynamic limitations at autothermal operations and results in significant process intensification. In this part, we will study a similar process, the chemical looping combustion (CLC). CLC is similar to RFR in that both reactors operate in dynamic, cyclic modes. While in a RFR, catalyst is fixed in the reactor and gas flow directions are switched, in CLC, gas flow directions are fixed while solid materials (oxygen carriers) are circulated between two interconnected reactors. The concept of CLC was proposed to obtain clean and more efficient fuel combustion / power generation.

In conventional coal or natural gas fired power plants, fuel and air are mixed directly and react at high temperatures. The reaction heat is used to drive turbines for electricity. This process generates significant NO_x , which is a major air pollutant. Also, carbon dioxide is a well-known

greenhouse gas and contributes to global warming; therefore a substantial reduction in atmospheric CO₂ is desired. To sequester the CO₂ emissions from the stationary power plants, high-concentration CO₂ is needed. However, to separate CO₂ from bulk mixed N₂ from air requires significant amount of energy and thereby reduces the overall electricity generate efficiency. Theoretically, using pure oxygen could avoid the above problems, however, building an air separation unit is a very capital intensive project and the oxygen plant itself is a large energy consumer.

An alternative is chemical looping combustion (CLC). It was first suggested by Ishida and coworkers in the 1990s and is receiving increasing attention in recent years [25,26].

In CLC, the combustion of a fuel is broken down into two, spatially separated steps (see Fig. 5): the oxidation of an oxygen carrier with air in the oxidizer, and the subsequent reduction of this carrier via reaction with a fuel (i.e. combustion) in the reducer. In the oxidizer, air reacts with a metal carrier, turning metal to metal oxide. The reaction heat is used to drive a turbine for electricity. The effluent gas is simply O₂ depleted air. The metal oxide is transferred to the reducer. In the reducer, fuel (syngas or methane) reduces metal oxide back to the metal. The reaction heat is also used to drive a turbine for electricity. The effluent gas contains mainly CO₂ and H₂O. After H₂O is condensed out, high concentration CO₂ is ready for sequestration. The reduced metal is transferred back to the oxidation stage, closing the materials “loop”. Interestingly, for most oxygen carriers, the oxidation step is strongly exothermic while the reduction, i.e. the combustion of the fuel, is a weakly exothermic or even endothermic reaction.

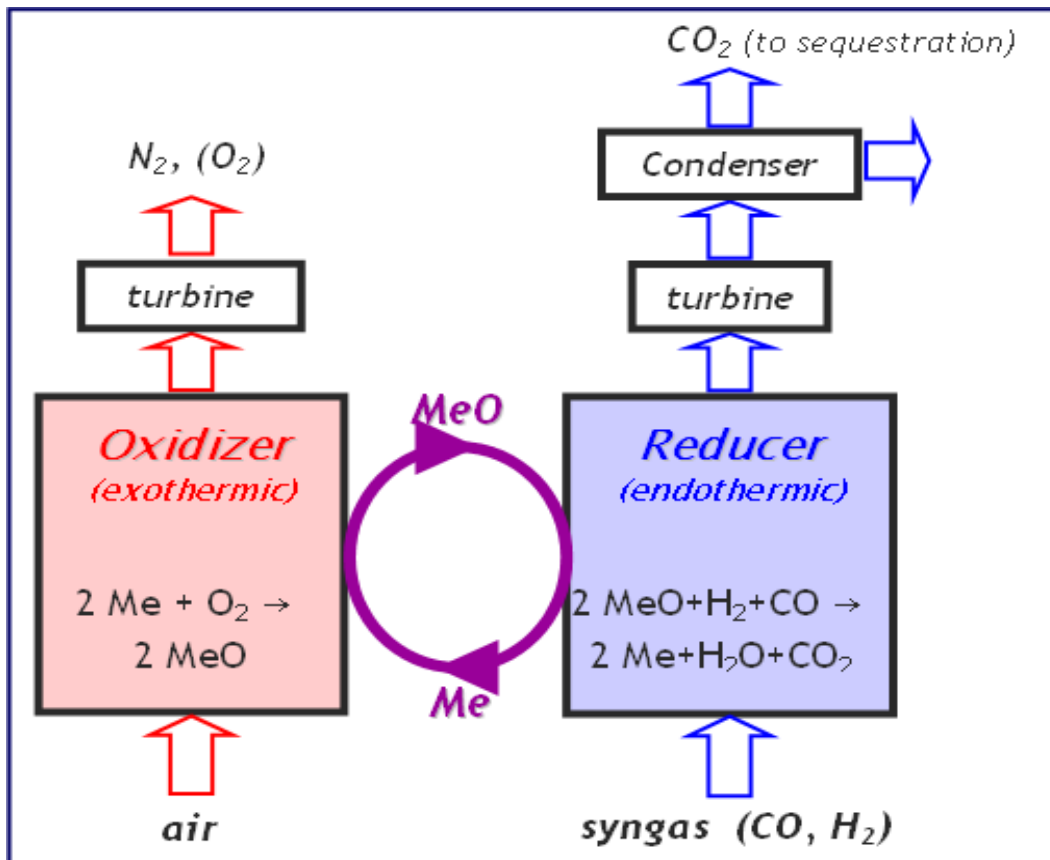


Figure 5. Schematic of chemical looping combustion (CLC).

Among the main advantages of the CLC concept are the fact that the combustion is flame-less, it operates at sufficiently low temperatures to avoid NO_x formation in the air-blown oxidizer, and it produces a mixture of CO₂ and H₂O as combustion gases, from which almost pure (i.e. sequestration-ready) CO₂-streams can be easily produced by simple condensation of water. Thus, the concept results in no significant efficiency penalty for CO₂ capturing, making it rather unique among current and emerging CO₂ capturing technologies. Chemical looping combustion is therefore one of the most promising technologies for improving the environmental ‘footprint’ of fossil fuel-based energy production in the short term, arguably one of the most

pressing needs considering the key role of these fuels for world energy production. However, it should be pointed out that the technology is also directly applicable towards combustion of renewable fuels, where it opens the possibility of highly efficient energy production with a ‘negative CO₂ footprint’.

The fundamental principle of CLC has already been demonstrated in a number of studies. However, significant problems remain on the way towards technical realization of the concept. The main problems are associated with the large solids transport in CLC and with the stability of the oxygen carrier. Ni and Fe have been identified as most promising components for use in CLC [27-34]. However, agglomeration and sintering of the metal component, attrition of the metal support, and slow oxidation kinetics of the carrier remain generally unsatisfactory.

In this thesis, we will report a significant step towards overcoming these hurdles based on novel nanostructured oxygen carriers for chemical looping combustion. Nanocomposite oxygen carriers were synthesized, characterized and redox behavior were tested. Shrinking core model (SCM) was applied to quantitatively analyze the redox behavior, particularly to determine the controlling steps (e.g. diffusion control or kinetic control) and to obtain kinetic and/or transport parameters. Details of these studies will be discussed in chapter 5.

2.0 CPOM MECHANISM

2.1 LITERATURE REVIEW

The mechanism for catalytic partial oxidation of methane to synthesis gas at short contact time conditions has been the subject of much debate which to-date is still not completely settled. Due to the extreme reaction conditions, short contact-time reactions are not amenable to typical spectroscopy-based mechanistic *in-situ* investigations at process conditions. Hence, studies either have to be conducted at ‘unrealistic’ conditions (lower flow rates, pressure and/or temperatures), or conclusions about the mechanism have to be inferred from ‘global’ measurements (inlet versus exit concentrations and temperatures).

A particular focus of the existing debate has been the distinction between direct and indirect reaction pathways in the formation of synthesis gas via CPOM. In direct oxidation, synthesis gas is formed in a single step via $\text{CH}_4 + 0.5 \text{O}_2 \rightarrow \text{CO} + 2 \text{H}_2$. In the indirect oxidation mechanism, part of the methane feed is initially combusted to CO_2 and water, and synthesis gas is subsequently formed via steam reforming of the remaining, unconverted methane feed as well as some water-gas shift reaction.

Hickman and Schmidt suggested that syngas is formed at short contact-time conditions exclusively via direct oxidation, largely based on the striking difference between their results and previous studies: in previous studies, syngas yields showed a strong decrease with decreasing

contact time, while Hickman and Schmidt observed an initial increase followed by a broad plateau in their yields[19,35,36]. They explained this observation based on a direct oxidation mechanism, in which methane is pyrolysed on the catalyst surface to C and H atoms, H radicals recombine to molecular H₂ which desorbs from the catalyst, while the remaining carbon reacts with (dissociatively adsorbed) oxygen to CO.

In contrast to that, a number of studies claim that indirect oxidation must be responsible for the formation of synthesis gas. Typically, evidence in these studies is based on the observed temperature profiles in the catalyst bed, i.e. on the observation that temperatures at the catalyst entrance were significantly higher than at the exit, or on the observation of reduced syngas yields and increasing total oxidation products with decreasing contact times[4,8,37-40]. Another disagreement - even among those studies that identify an indirect reaction mechanism - concerns the dominant reaction pathway in the post-combustion section of the catalyst. Although most studies claim that steam reforming, dry reforming and water gas shift reactions coexist in this part, again clear and convincing evidence is often lacking. Furthermore, most studies are not quantitative in nature, and hence the relative contribution of different reaction pathways to the production of syngas remains unclear.

In this context, much effort has also been devoted to the development of elementary-step kinetics and detailed reactor models[41-47]. However, much uncertainty remains to-date with regard to the accuracy of the kinetic parameters used in these models, and it is hence questionable whether conclusions about the mechanism can be drawn from simulation studies.

Another important question that arises at the very high temperature conditions of CPOM concerns the possible occurrence of homogeneous gas-phase reactions. In a typical catalytic process the catalyst is used to allow a chemical reaction at conditions at which homogeneous

(uncatalyzed) reactions are too slow to be of practical relevance. The extremely high temperatures of CPOM, however, open virtually any reaction pathway, both thermodynamically due to the large entropic contribution to the Gibbs energy of reaction, as well as kinetically by overcoming the large activation energy barriers of homogeneous reactions. Therefore, great care must be taken in any experimental investigation to assure that the observed reactivity is not falsified by homogeneous reactions and conclusions about the catalytic surface mechanism are hence invalidated.

In this chapter, we show results from a simple, but well-defined study which aims to gain a better understanding of the reaction mechanism of CPOM over Pt-coated monolith catalysts by varying the catalyst contact time, and by correlating the obtained syngas yields with in-situ temperature profiles measured throughout the catalyst bed at reaction conditions. In this way, we gain insights into the reaction pathway at different positions along the reactor axis, allowing quantification of the contribution of different reaction steps to the formation of the syngas components CO and H₂.

2.2 EXPERIMENTAL

The reactor consists of a quartz-glass tube (19 mm ID, 22 mm OD, 250 mm length) with catalyst and inert-zones, which is then inserted into stainless steel housing. The reactants (CH₄ and air) are fed with standard mass-flow controllers and product gases are analyzed with a double-oven gas chromatographic system. All experiments were carried out autothermally, i.e. the laboratory reactor was wrapped in several layers of insulation and no additional external heating was applied to the reaction.

The catalysts were supported Pt catalysts. Extruded cordierite monoliths with 400 cpsi and 17 mm diameter were coated with Pt via conventional precipitation from H_2PtCl_6 solution. After impregnation, the catalysts were dried overnight at room temperature and then calcined at 600°C in air for 5 hours, followed by reduction in a gas flow of 5 vol% H_2 in N_2 at 500°C for 2 hours. This resulted in a closed metal film on top of the ceramic monolith (see Fig. 6). Typical weight loadings were ~2 - 4wt%. The length of these catalysts was varied between 2 mm and 10 mm.

A moveable thermocouple allowed for spatial temperature measurements throughout the catalyst as well as the inert zones surrounding the catalyst. The in-situ temperature measurements were then correlated with the corresponding product gas as analyzed by GC.

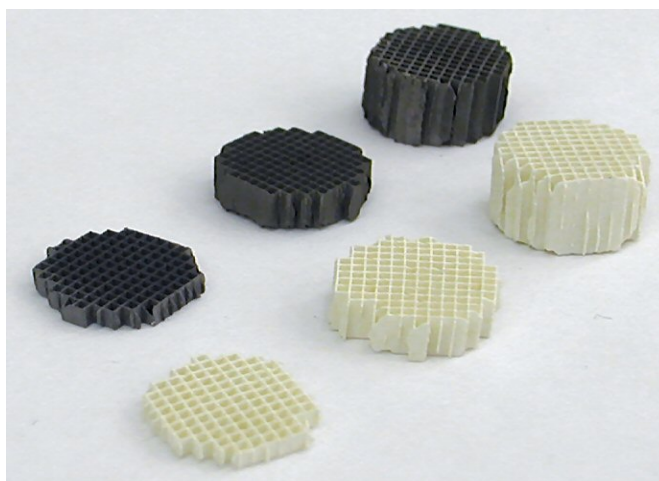


Figure 6. Cordierite monoliths with 2 mm, 5 mm, and 10 mm length before and after impregnation with Pt.

2.3 RESULTS

In order to study the reaction progress, we varied the length of the catalyst as well as the total inlet gas flow rate, resulting in the study of a rather wide range of residence times in two different ways. The overlap between the residence times obtained in these two ways served as a further reassurance that our results are reliable and independent of experimental artifacts and/or the presence and location of the temperature probe. Effluent gas composition as well as temperature profiles throughout the monoliths were measured, and will be discussed in detail in the following.

2.3.1 Variation of catalyst length

Fig. 7 shows temperature profiles (left graph) along with corresponding methane conversions and syngas selectivities (right graph) for a stoichiometric methane-air mixture ($\text{CH}_4/\text{O}_2 = 2.0$) at a total inlet gas flow of 4 slm (standard liters per minute) for three different catalyst lengths of 2 mm (squares), 5 mm (circles), and 10 mm (triangles). In the left graph (temperature profiles), gas flow is from left to right, and the vertical lines indicate the beginning of the catalyst (left-most line at $z = 0$ mm) as well as the end of the 2 mm, 5 mm, and 10 mm catalysts, respectively.

The temperature profiles show strong similarities as well as significant differences between the three catalyst lengths. For all three catalyst lengths, the temperature profiles are identical as long as catalyst is present, i.e. for all three catalysts the temperature profile over the first 2 mm is identical, and the profiles between $z = 2$ mm and $z = 5$ mm are further identical for the 5 mm and the 10 mm catalyst.

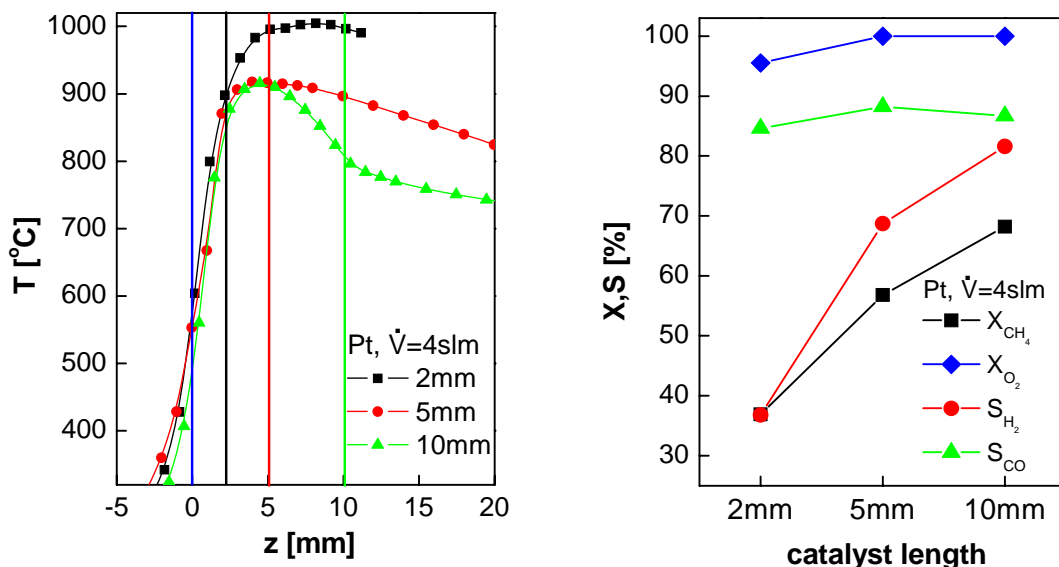


Figure 7. Temperature profiles inside the catalyst (left graph) for a 2 mm (squares), 5mm (circles) and a 10 mm (triangles) long catalyst along with the corresponding values for S_{CO} (triangles), S_{H_2} (circles), X_{CH_4} (squares) and X_{O_2} (diamonds) (right graph).

However, the temperature maximum for the 2 mm catalyst is increased by about $\sim 100^\circ\text{C}$ in comparison to the other two catalysts. Most significantly, this temperature maximum is located downstream of the catalyst, i.e. outside the catalyst zone. Apparently, the extremely short residence time of less than 1 ms at these conditions is not sufficient for the catalytic reaction to go to completion, and hence post-catalytic homogeneous reactions occur. This is also reflected in the conversion and selectivities observed in this case (Fig. 7, right graph): methane conversion and hydrogen selectivity are below 40%, i.e. much below the conversion and selectivity observed with the longer catalysts. Oxygen is not completely converted on the 2 mm catalyst (X_{O_2} is 95%), while the conversion is 100% on both the 5mm and the 10 mm catalyst. Clearly, unconverted

oxygen leads to post-catalytic homogeneous combustion, resulting in increasing temperatures down-streams of the catalyst. Since H_2 is much more reactive than CO and CH_4 , this leads predominantly to water formation, explaining the steep drop in H_2 selectivity. The incomplete oxygen conversion despite this homogeneous reaction can be attributed to poor radial mixing in the straight-channel extruded monolith that serves as post-catalytic radiation shield.

In contrast to this, the 5 mm and 10 mm catalysts show identical temperature curves up to the temperature maximum of about 900°C which is located at about $z= 4.5$ mm, i.e. inside the catalyst zone for both catalysts. However, while the temperature profile for the 5 mm catalyst shows a rather flat, linear decrease following this maximum, the temperature profile for the 10 mm catalyst drops off steeply towards the end of the catalyst zone and then shows the same flat decrease as for the 5 mm catalyst.

The flat, linear decrease in temperature behind the maximum temperature for the 5 mm catalyst can be traced back to heat losses. The temperature maximum is located close to the catalyst end, so that the rather high heat losses from the small laboratory reactor determine temperatures in the inert zones. No indication for post-catalytic reactions can be found in the temperature curve, consistent with the fact that complete oxygen conversion is attained for the 5 mm catalyst. Correspondingly, methane conversion as well as hydrogen selectivity are strongly improved in comparison to the 2 mm catalyst.

In case of the 10 mm catalyst, the steep drop in the catalyst temperatures in the second half of the catalyst is a clear indication of endothermic reactions. The sudden change in the temperature gradient upon transition to the inert zone indicates that these reactions are truly catalytic. The nature of the endothermic reaction becomes apparent from the conversion and selectivity data: both methane conversion and hydrogen selectivity are further increased over the

data for the 5 mm catalyst, but CO selectivity drops slightly. These observations indicate that either steam reforming (Eq. (1)) and/or CO₂ reforming (Eq. (5)) are occurring in the second half of the 10 mm catalyst:



The fact that CO selectivity changes only very slightly seems to indicate CO₂ reforming plays only a minor role, which will be clarified in detail in the following paragraphs.

2.3.2 Effect of contact time

To gain further understanding of the reaction pathways, the flow rate was varied from 1 slm to 4 slm for each of the three catalysts. The catalyst contact time was calculated as the catalyst length divided by the actual gas velocity (adjusted by the mean temperature in the catalyst bed). Fig. 8 shows measured gas phase concentrations in the exit gas stream against calculated catalyst contact time normalized to N₂ concentration of unity (since N₂ does not react under the conditions of these experiments, the mol number for N₂ does not change along the reactor). The left graph shows the data for all experimental runs, while the right-hand graph shows a zoomed view of the first 4 ms.

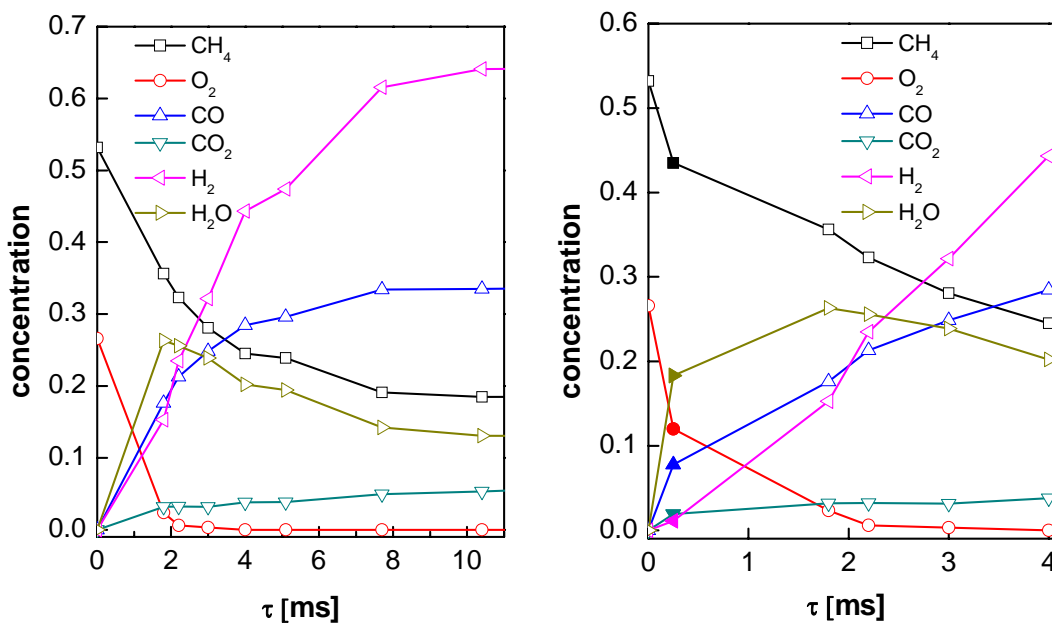


Figure 8. Relative concentrations of the reactants and main products as a function of catalyst contact time (left). The right graph shows the data for the first 4 ms together with one data point at extremely short contact time (0.21 ms) taken from ref [48] (close symbols).

One can distinguish two different reaction zones: an oxidative zone over the first ~ 3 ms, and a reforming zone thereafter. Contact times between 2 and 3 ms are needed to achieve complete oxygen conversion in agreement with our interpretation of the results with the 2 mm catalyst. At longer contact times (> 3 ms) where O₂ has been completely consumed, the reaction pathway shifts to predominant steam reforming as reflected in the parallel trends for CH₄ and H₂O concentrations on one hand, and of CO and H₂ on the other hand. Endothermic steam reforming is hence also responsible for the steep temperature drop observed above in the second half of the 10 mm catalyst. We can exclude CO₂ reforming as cause for this temperature drop

since overall CO₂ concentrations are very low and the absolute mol number of CO₂ increases slightly with increasing contact time. If CO₂ reforming was occurring to a significant degree, the number of moles of CO₂ would have to decrease with increasing contact time. (Note that due to the change in the total number of moles in the course of the reforming as well as the oxidation reactions, this argument does not hold for concentrations.) The observed slight increase in CO₂ can be attributed to the occurrence of some water gas shift (Eq. (2)).



To further corroborate this reaction mechanism, we performed a stoichiometric analysis for our experimental results, assuming only steam reforming and water gas shift reactions along the reactor. A typical result from these calculations is shown in Table 1. Column 2 and 3 in Table 1 show the product distribution on the 5 mm (corresponding to $\tau = 4$ ms in Fig. 8) and 10 mm catalyst at 4 slm (corresponding to $\tau = 7.7$ ms in Fig. 8). The expected product distribution at $\tau = 7.7$ ms is then calculated by assuming that changes in the concentrations between 4 ms and 7.7 ms occur exclusively via steam reforming and water gas shift reactions. CO and H₂ production and H₂O consumption via steam reforming (SR) is calculated based on the decreasing amount of CH₄ from $\tau = 4$ ms to $\tau = 7.7$ ms as shown in column 4, while CO₂ and H₂ production and CO consumption via water gas shift (WGS) is calculated based on the increasing amount of CO₂ as shown in column 5. The calculated product distribution (column 6) is then compared to the experimental data (column 3) and the relative errors are shown in column 7.

Clearly, the proposed mechanism in this regime agrees very well with the experimental data. Relative errors of calculated vs experimental data are below 4%, which is within experimental error. From Table 1, we can calculate that water gas shift adds ~7% H₂ and consumes ~21% CO produced by steam reforming. Hence, the combined effect of steam

reforming and water gas shift results in an H₂-enrichment of the syngas mixture, leading to a H₂:CO ratio of about 2. This ratio has often been interpreted as being indicative of direct partial oxidation, since it is the stoichiometrically expected ratio for this reaction. As our analysis shows, this is not the case. Instead, a complex interplay between oxidation, reforming, and water gas shift is responsible for this result.

Table 1. Calculated mol numbers based on the steam reforming and water gas shift pathway from $\tau = 4$ ms to $\tau = 7.7$ ms

Species	$\tau = 4$ ms (exp.)	$\tau = 7.7$ ms (exp.)	SR	WGS	$\tau = 7.7$ ms (cal.)	(cal.- exp.)/exp \times 100%
CH ₄	0.2453	0.1908	-0.0545	0	0.1908	0
O ₂	0	0	0	0	0	0
CO	0.2846	0.3343	0.0545	-0.0112	0.3279	-1.91%
CO ₂	0.0381	0.0493	0	0.0112	0.0493	0
H ₂	0.4431	0.6156	0.1635	0.0112	0.6178	0.36%
H ₂ O	0.2022	0.1421	-0.0545	-0.0112	0.1365	-3.94%
N ₂	1	1	0	0	1	0

Similar stoichiometric analyses based on steam reforming and water gas shift were then performed for the whole range of contact times shown in Fig.8. The relative errors in CO, H₂, and H₂O concentrations, as well as the contributions of steam reforming to total H₂ formation are summarized in Table 2.

As expected from our previous discussion, the assumption of pure steam reforming and water gas shift results in large errors for the first 2-3 ms. Clearly, in the presence of O₂, the actual reaction pathway cannot be reduced to steam reforming and/or water gas shift. However, as soon

as all O₂ has been consumed, i.e. starting around $\tau = 3$ ms, the calculated product concentrations agree very well with the experimental results with relative errors of less than 5%.

Table 2. Relative errors of the calculated concentrations based on the steam reforming and water gas shift pathway and the experimental results over the contact time shown in Figure 8. The amount of H₂ produced from steam reforming is also shown in the last row as percentages.

τ , ms	0 - 1.8	1.8 - 2.2	2.2 - 3	3 - 4	4 - 5.1	5.1 - 7.7	7.7 - 10.4
CO error, %	-18.27	-1.97	2.90	-2.39	-1.82	-0.30	0.42
H ₂ error, %	265.99	7.40	12.22	-1.87	-2.51	2.29	-0.64
H ₂ O error, %	178.98	-10.17	-10.34	-2.67	0.72	-4.93	1.38
H ₂ (by SR, %)	----	----	----	94.35	93.93	93.00	82.08

Quantitatively, we calculate that steam reforming contributes more than 90% of the total H₂ production in the second part of the reactor and WGS contributes less than 10%. At longer contact times ($\tau > 8$ ms), steam reforming approaches equilibrium and slows down, and the relative contribution of water gas shift increases as indicated by the drop in the H₂ percentage from SR (bottom row, last column in Table 2).

Due to the limitations in our experiments (i.e., the occurrence of post-catalytic homogenous reactions for very short catalysts and high flow rates), we do not have sufficient data at very short contact times to conduct a similar analysis and hence directly identify a reaction mechanism for the initial stages of the reaction. This problem is intrinsic to the reaction system and can be expected to plague any similar investigation unless an active quench is provided immediately following the catalyst zone. Despite these reservations, we included one data point from a previous study by Heitnes et. al. [48,49] in our results in Fig. 8 (right graph),

indicated by the filled symbols at $\tau = 0.21$ ms. These authors reported CPOM on a Pt gauze where extremely short contact times are realized. The included data point was obtained at conditions similar to our experimental conditions (900°C , $\text{CH}_4/\text{O}_2=2$) but at very short contact time of $\tau = 0.21$ ms. One can see that the data point fits well into the trends observed from our data, although methane and oxygen conversions are slightly higher than expected from the trends in our own data, which is consistent with some amount of post-catalytic homogeneous conversion.

As evident from the right-hand graph of Fig. 8, oxygen is rapidly consumed and CO, H₂O, and a small amount of CO₂ is produced directly from these oxidation reactions in the initial milliseconds. In contrast to that, initial H₂ selectivity is very low. While all other product concentration curves can be easily extrapolated without changes in curvature to the origin of the graph (i.e. to zero concentration at $t = 0$ ms), the same extrapolation for H₂ requires the presence of an inflection point, i.e. an S-shaped production curve, which is a characteristic feature indicative for secondary products. We can hence deduce that CO, CO₂, and H₂O are primary reaction products from direct oxidation of methane with oxygen, while H₂ is a secondary product from a sequential reaction.

The simple total oxidation of methane via



can not be a major reaction pathway in this initial catalyst section, since it would generate significant amounts of CO₂, which contradicts experimental observations. Rather, our results indicate that the dominant reactions in the oxidation section are the oxidation of methane via:



followed by steam reforming:



However, we cannot exclude another possible reaction scheme which is also consistent with our experimental data. In this scheme, CH₄ is first directly oxidized to CO and H₂, following a true partial oxidation pathway. Since partial oxidation is a weakly exothermic reaction, it can not result in the sharp temperature increase observed near the front edge of the catalyst. This heat release is due to the oxidation of the produced H₂ with O₂ to form H₂O (which is almost instantaneous at these conditions). Further methane conversion then occurs again due to steam reforming. Overall, this reaction scheme hence consists of the following steps:



Obviously, reaction (6) from the first reaction scheme is obtained by the addition of reactions (3) and (7) in the second scheme, and the two schemes are hence overall identical. A distinction whether the reaction progresses via the first or the second scenario is hence of purely academic nature, since the extremely high rate of reaction for catalytic hydrogen oxidation makes an experimental distinction all but impossible. For all practical purposes, the two reaction schemes have hence to be regarded as identical.

2.4 DISCUSSIONS

Overall, our experiments allowed us to distinguish two different reaction zones: an oxidation zone near the catalyst entrance, followed by a steam reforming zone thereafter. CO is formed mostly in the first part (~70%) via direct oxidation, while a majority of H₂ is formed in the second part (~70%) via steam reforming. In fact, assuming the above discussed first reaction

pathway in the oxidation section (last paragraph of section 2.3.2, reactions (6) + (1)), it seems most likely that essentially all H₂ is formed via steam reforming (with minor contributions from water gas shift in the later part of the catalyst). Thus, the reaction mechanisms are fundamentally different for the carbon and hydrogen components and the question whether syngas is produced via a direct or indirect pathway needs to be answered separately for hydrogen and CO.

In the following discussion, we will show that this mechanism can explain in a very straightforward way some of the early observations and main characteristics of “CPOM” over Pt catalysts, namely, the effects of changing gas flow rate, changing CH₄/O₂ ratio, and the effect of catalyst aging and deactivation. In order to base this discussion on a consistent set of data, the effects will be discussed based on data obtained in the present experimental investigation, although many similar data are available in the literature.

2.4.1 Effect of gas flow rate

As discussed in the introduction, one of the most significant characteristics of CPOM are the extremely high flow rates (i.e. very short contact times) that can be realized in this reaction system. Furthermore, the observation that with increasing flow rates, conversions and selectivities increase were taken as strong indications that CPOM is indeed proceeding via a direct partial oxidation mechanism. We hence examined again the results from our experiments with varying flow rates in light of the above deduced sequential reaction mechanism.

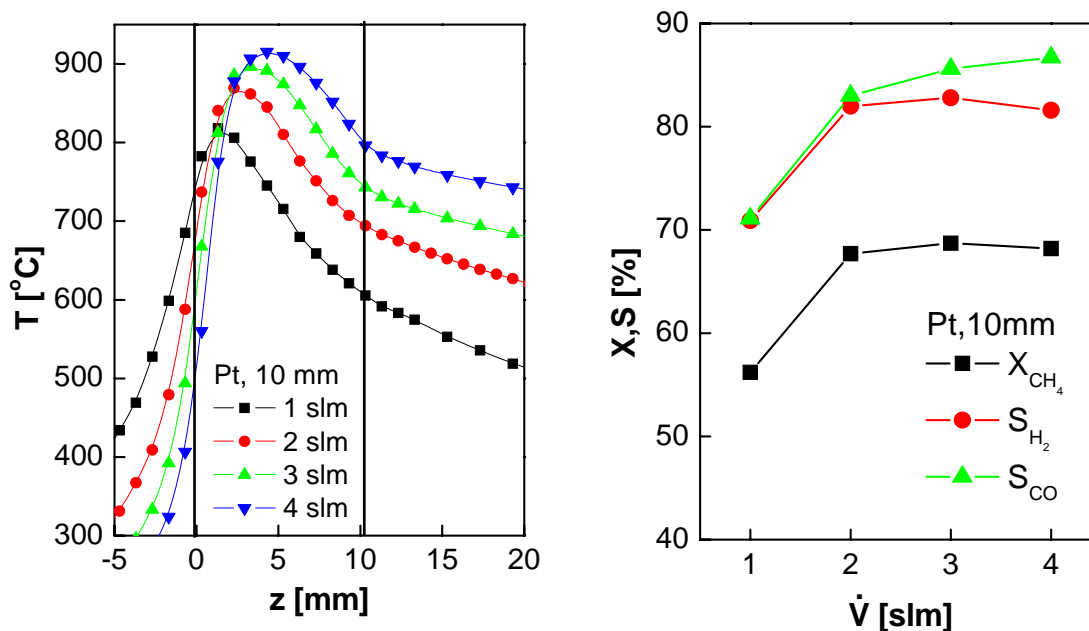


Figure 9. Temperature profiles inside the 10 mm catalyst (left graph) at different inlet gas flow rate along with the corresponding values for S_{CO} (triangles), S_{H_2} (circles) and X_{CH_4} (squares) (right graph).

Fig. 9 shows temperature profiles inside a 10 mm catalyst at different total gas flow rate (left graph). Gas flow is from left to right and the vertical lines mark the entrance and exit of the catalyst. One can see that the gas temperature is significantly increased above room temperature before reaching the catalyst zone and then reaches its maximum in the first part of the catalyst before dropping off steeply from the maximum point toward the catalyst exit. Increasing the flow rate decreases the entrance temperature while increasing maximum and exit temperatures in the catalyst zone. Furthermore, as indicated by the position of the maximum temperature, the

reaction front is pushed further into the catalyst zone from $z \sim 1.5$ mm at 1 slm to $z \sim 4.5$ mm at 4 slm.

At the autothermal conditions of our experiments, reaction temperatures are determined by the heat of reaction, the heat convected with the reactants and conducted in the monolith, and by heat losses from the reactor. Increasing the flow rate increases the heat release by the reaction which results in higher maximum temperatures. On the other hand, increasing the flow rate also increases the convective heat transfer by the gas stream, cooling down the catalyst entrance due to (relatively) cold feed gases while heating up the catalyst exit due to hot product gases. This explains the observed trends in the temperature profiles.

It is interesting to note that for all flow rates the temperature drop inside the catalyst toward the exit is steeper than that in the subsequent inert zone. This difference is more pronounced at higher than at lower flow rate. In section 2.3, we had seen that the steep drop in the catalyst is due to endothermic steam reforming and the mild temperature decrease in the inert zone is due to heat losses. In order to further support this interpretation of our data, we conducted thermodynamic calculations on the product gas compositions over the 10 mm Pt catalyst at different flow rates.

First, we calculated the reaction quotient Q (based on exit concentrations) for steam reforming, water gas shift, and CO_2 reforming. They are calculated by the following formulas:

$$Q_{SR} = \frac{[CO][H_2]^3}{[CH_4][H_2O]} \quad Q_{WGS} = \frac{[CO_2][H_2]}{[CO][H_2O]} \quad Q_{CO_2R} = \frac{[CO]^2[H_2]^2}{[CH_4][CO_2]}$$

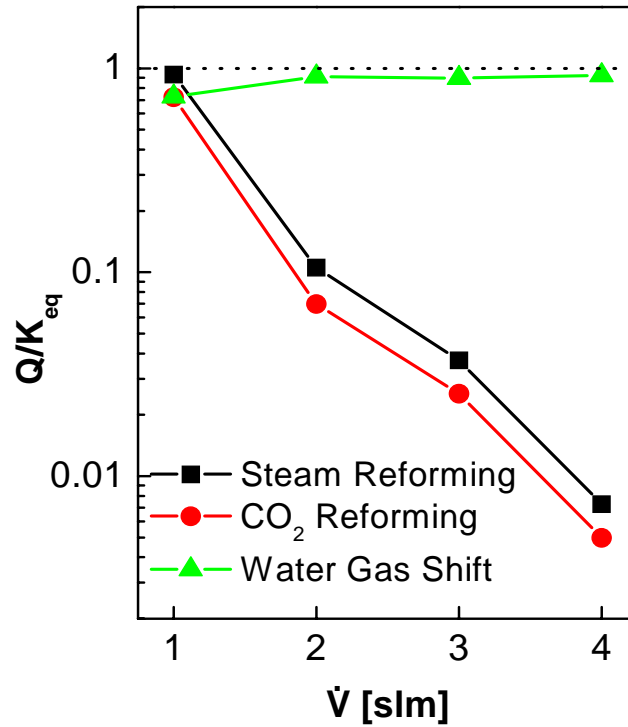


Figure 10. Q/K_{eq} as a function of flow rate. Q is calculated based on exit concentrations, K_{eq} is the reaction equilibrium constant corresponding to the catalyst exit temperature.

These quotients were then compared to the corresponding equilibrium constants K_{eq} , calculated at the measured catalyst exit temperature. Results are shown in Fig. 10, where the ratio Q/K_{eq} is plotted versus total volumetric flow rate (The ratio Q/K_{eq} is a measure for how far the reaction has approached equilibrium).

One can see that at 1slm, Q/K_{eq} for steam reforming is close to 1, which indicates steam reforming is close to equilibrium. As the flow rate increases, Q/K_{eq} for steam reforming drops steeply, i.e. steam reforming is departing from equilibrium with increasing flow rates. Q/K_{eq} for CO_2 reforming is shown for completeness sake and shows similar trends to steam reforming,

although at consistently lower values. As discussed above, however, CO₂ reforming does not play a significant role in the overall reaction due to the very small CO₂ concentrations. Furthermore, the calculations show that water gas shift is virtually at equilibrium at all flow rates with slightly increasing values of Q/K_{eq} with increasing flow rates, most likely due to increasing reaction temperatures and correspondingly accelerated reaction rates.

These thermodynamic calculations help to explain the observed temperature profiles in Fig. 9. At 1slm, the maximum temperature is located at $z \sim 1.5$ mm, indicating the end of the oxidation zone, and hence leaving the majority of the catalyst bed for steam reforming. At these low flow rates, steam reforming has hence enough time to approaches equilibrium, and, once no more endothermic reaction is occurring, the further temperature decrease in the catalyst bed is caused only by heat losses from the reactor. Therefore, a smooth transition of the temperature profile from the catalyst exit to the inert zone is obtained.

In contrast to that, at high gas flow rates ($V = 4$ slm), the maximum temperature is located at $z \sim 4.5$ mm, significantly reducing the catalyst length – and even more the remaining contact time - available for steam reforming. Hence, steam reforming is far from equilibrium when the gases leave the catalyst zone. As a result, a sudden bend in the temperature profile is observed at the transition from the catalyst exit to the inert zone.

Exit conversions and selectivities, shown in the right-hand graph in Figure 4, can be explained in a straightforward manner. At 1slm, the heat production rate is relatively low, resulting in low temperatures, relatively slow kinetics, and an unfavorable equilibrium for steam reforming. Overall conversion and selectivity is hence low. Increasing the flow rate from 1 slm to 2slm significantly increases the heat production rate and hence also the temperature in the catalyst. Due to the resulting increased reaction rates and – most importantly – the favorable shift

in reaction equilibrium for steam reforming, strong improvements of CH₄ conversion and H₂ selectivity are observed, despite the fact that the steam reforming reaction cannot reach the new equilibrium any more. Eventually, however, the quenching of the steam reforming reaction outweighs the improvements due to increasing temperatures, and CH₄ conversion and H₂ selectivity decrease, while the increasing temperatures in the initial oxidation zone still lead to slight increases in CO selectivity.

Hence, the trends observed with increasing flow rate can be explained in a quite straightforward manner based on the shifting temperature profiles and their effect on the sequential reaction mechanism.

2.4.2 Effect of CH₄ to O₂ ratio

Another characteristic of CPOM is the often discussed observation that methane conversion as well as hydrogen selectivity increase with decreasing CH₄/O₂-ratio in the feed, while CO selectivity remains largely unaffected, as shown here in the right graph in Fig. 11. This observation has previously been explained by us and others based on the fact that with decreasing fuel:air ratio oxygen becomes less limiting for the reaction, and hence more methane can be converted. This leads to higher reaction temperatures, which are favorable for partial oxidation, explaining the improved hydrogen selectivity. However, the low sensitivity of the CO selectivity to changes in the CH₄/O₂-ratio remains unexplained.

From the temperature profiles inside the 10 mm Pt catalyst at varying CH₄ to O₂ feed ratios (Fig.11, left graph) one can see that as expected the overall temperatures, including entrance, maximum and exit temperatures, increase with decreasing CH₄/O₂-ratio. At the same time, the location of the reaction front (characterized by the temperature maximum) shift slightly

towards the catalyst entrance, indicating accelerated reactions due to increasing temperatures and the availability of additional oxygen. However, this shift is much less pronounced than the strong shift towards the catalyst exit that was observed above with increasing gas flow rates. The location of the reaction front is hence determined predominantly by the gas flow rather than the feed ratio.

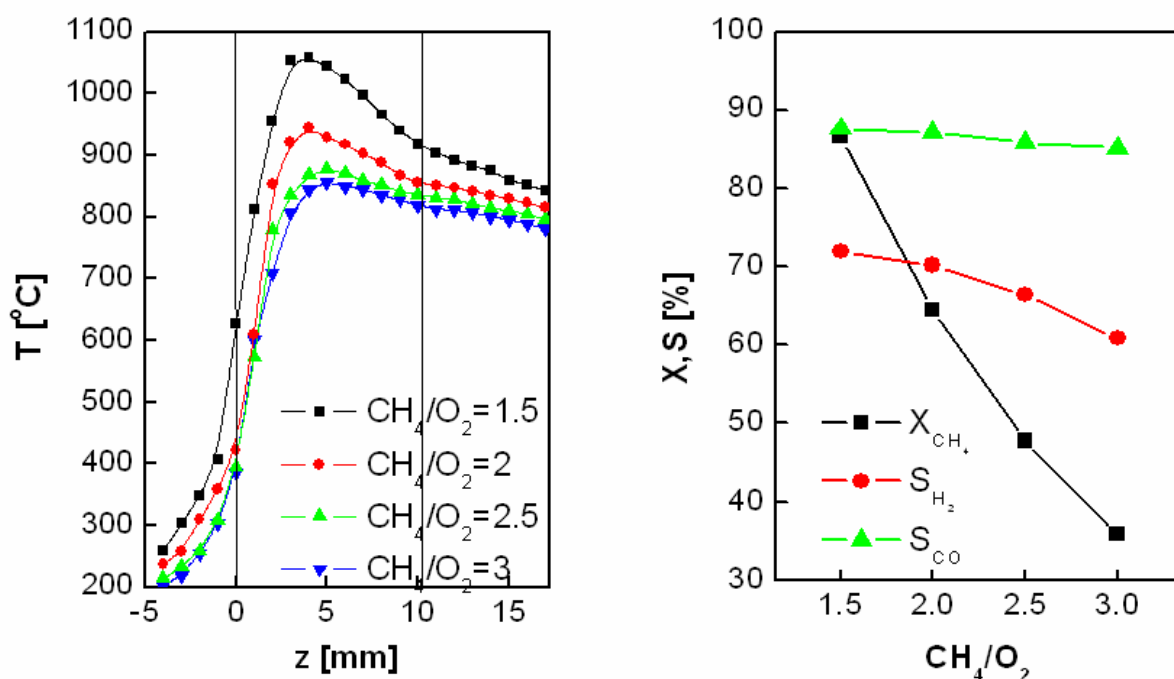


Figure 11. Temperature profiles (left) and corresponding CH₄ conversion (right, square), H₂ selectivity (right, circle) and CO selectivity (right, triangle) on 10 mm Pt catalyst at different inlet CH₄/O₂ ratios. Total flow rates were 4 slm, and the vertical lines mark the start and the end of the catalyst.

One can furthermore see in Fig. 11 that the temperature gradients in the catalyst zone increase with decreasing CH_4/O_2 ratio both at the entrance as well as the exit of the catalyst. The increasing gradient at the catalyst entrance can be explained simply based on the increasing availability of oxygen and hence the increasing amount of (exothermal) methane oxidation along reaction path (6). On the other hand, the steepening temperature drop in the second half of the catalyst suggest increasing amounts of (endothermal) steam reforming. This is consistent with the increasing amount of water formed in the initial part of the catalyst as well as the higher reaction rates due to the increased temperatures. The sequential mechanism can hence explain the observed trends in methane conversion and syngas selectivities in a simple and consistent way: with decreasing CH_4/O_2 ratio, methane conversions increase due to increasing consumption in the primary oxidation with oxygen as well as the secondary reforming with H_2O . Hydrogen selectivities increase due to the strongly increasing amount of steam reforming, shifting reaction selectivity from water to H_2 . CO selectivities, on the other hand, remain essentially unchanged by variations in the feed gas ratio since it is unaffected by the competition between the two reaction pathways, both of which form only CO, and since total oxidation via reaction path (4) remains a minor reaction channel at all conditions.

2.4.3 Catalyst deactivation

As a final test for the proposed mechanism, we consider catalyst deactivation in CPOM over Pt catalysts. Pt is known to deactivate fairly rapidly in CPOM, and this deactivation affects methane conversions and hydrogen selectivities most strongly. This is shown in Fig. 12, where again temperature profiles through the catalyst zone are shown for a fresh and a deactivated Pt catalyst (left graph), along with methane conversion and syngas selectivities vs time on stream

(right graph). The deactivation test was conducted with a 10 mm catalyst at a total feed gas flow rate of 4 slm and a CH_4/O_2 ratio of 2.0. Gas flow in the left graph is again from left to right, and the vertical lines mark the entrance and exit of the catalyst.

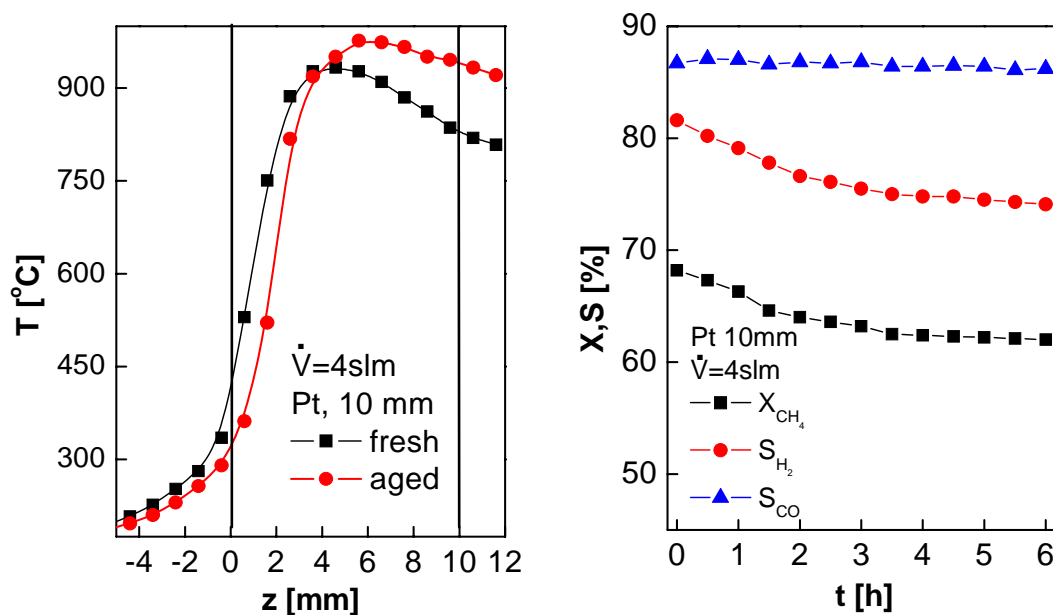


Figure 12. Left: Temperature profiles on the fresh (squares) and aged (circles) 10 mm Pt catalyst. Right: S_{CO} (triangles), S_{H_2} (circles) and X_{CH_4} (squares) as a function of time on stream.

We had previously found that deactivation of Pt catalysts occurs predominantly via metal volatilization, i.e. the loss of active surface area. Due to this loss, the reaction front shifts further downstream in the catalyst zone with progressing deactivation, as seen in Fig.12 (left graph). More importantly, the flattening of the temperature profile in the later part of the catalyst and the

somewhat increased temperature maximum indicate that the loss of active surface area in combination with the reduced length of catalyst available following the delayed oxidation reaction lead to a significantly reduced amount of steam reforming.

In agreement with this, CH₄ conversion and H₂ selectivity decrease in parallel with time-on-stream while CO selectivity is virtually unaffected, following the same reasoning that was outlined above (section 2.4.2). Again, the sequential mechanism can thus explain these observations in a simple and consistent way, since the primary oxidation zone is necessarily less sensitive to deactivation than the subsequent steam reforming zone. It should be noted that these results are similar to our previous report on the deactivation of an alumina-foam supported Pt catalyst[9].

2.5 SUMMARY AND CONCLUSIONS

In this chapter, we studied the mechanism of catalytic partial oxidation of methane over a supported Pt catalyst in which we varied catalyst length and gas flow rate, and correlated global conversion and selectivity data with in-situ temperature profile measurements. In this way, we were able to obtain a detailed understanding of the reaction mechanism in a fairly simple and straight-forward experiment. The measurement of temperature profiles furthermore allowed us to identify conditions at which post-catalytic homogeneous reactions would mask and/or falsify the study of catalytic reactions and enabled us to exclude these data points.

The reaction pathway on the supported Pt catalyst consists of an initial oxidation zone in which predominantly CO and H₂O are formed, followed by a steam reforming zone. The oxidation reactions lead to a sharp temperature increase near the front edge of the catalyst. As

soon as the available oxygen is consumed, the reaction shifts to steam reforming, accompanied by some water gas shift reaction. The endothermic steam reforming reaction results in a steep temperature drop towards the catalyst exit.

The relative extend of the two zones is mostly influenced by the flow rate and much less by the CH₄ to O₂ ratio, i.e. at virtually all conditions the oxidation reactions occurred over the first ~3 ms, and steam reforming over the remaining contact time. The two reaction zones also represent two separate reaction pathways for the formation of the syngas components CO and H₂. CO is produced predominantly via direct oxidation (~70%), while most – and possibly all - H₂ is produced via steam reforming (>70%).

The fundamentally different behavior of H₂ selectivity and CO selectivity can now be explained in a straight-forward and consistent way based on this difference. The overall reaction behavior is dominated by the interplay between the two sequential reaction pathways, i.e. the direct oxidation of methane with oxygen to CO and H₂O, and the subsequent reforming of methane with water from the first reaction step. The sensitivity of the steam reforming reaction versus the relative insensitivity of the oxidation reaction to changes in the reaction conditions leads to the typically parallel behavior of methane conversion and hydrogen selectivity. Since both reaction pathways produce CO, CO selectivity is largely insensitive to any changes.

Total oxidation to CO₂ and H₂O as well as water-gas-shift reactions appear to occur only to a minor degree, and no indication for the presence of dry reforming (i.e. CO₂ reforming) was found at any condition.

While the reported study was limited to Pt catalysts supported on extruded cordierite monoliths, we suspect that the conclusions are much more general than that. While absolute values for syngas yields in catalytic partial oxidation of methane vary significantly with the

choice of catalyst, the key characteristics of CPOM – i.e. the changes in reaction selectivity and conversions with gas flow rates, CH₄:O₂ ratio, and catalyst deactivation – are virtually identical for a wide range of metals (Pt, Rh, Ir, Ni) and different supports (extruded and foam monoliths). This suggests that the same sequential mechanism may be at work over all these catalysts, and the observed differences stem largely from the different degree to which the initial, primary oxidation versus the subsequent, secondary steam reforming is occurring over the specific catalyst system.

3.0 REVERSE FLOW REACTOR (RFR) OPERATION

The mechanism in chapter 2 reveals that increasing feed gas temperature results in increased syngas yields. While this can be realized through recuperative heat-exchange in a CHXR (Fig. 3, chapter 1), a more efficient way is to run the reaction in a RFR. Previous studies in our group, demonstrated that the regenerative heat-integration in RFR operation leads to a strong increase of the feed gas temperature at the catalyst entrance and results in increased CH₄ conversion and syngas yields [1,9,13,14]. The effect of heat-integration can be visualized through the dynamic temperature profiles in the catalyst. However, the irregular structure of the foam monolith used in those studies prevented the measurement of temperature inside the catalyst. To solve this problem we conducted experiments with extruded monolith supports. The straight channels in an extruded monolith made temperature measurement inside the catalyst possible.

3.1 EXPERIMENTAL

The experimental setup used for the investigations is shown in Fig. 13. The hybrid reactor consists of a quartz-glass tube with catalyst and inert-zones, which is inserted into a metal housing. The inert zones consist of cordierite extruded monoliths (1.7 cm diameter, 11 cm long). In contrast to our previous studies, we used Pt-coated *extruded* monolith (1.7 cm diameter, 1 cm long) which had been prepared by standard impregnation procedures [13]. The straight-channel

structure of the extruded monolith (in contrast to the tortuous structure of the alumina foams) allows the insertion of moveable thermocouples and thus the in-situ measurement of the spatio-temporal dynamics of the temperature throughout the reactor and the catalyst zone at operating conditions.

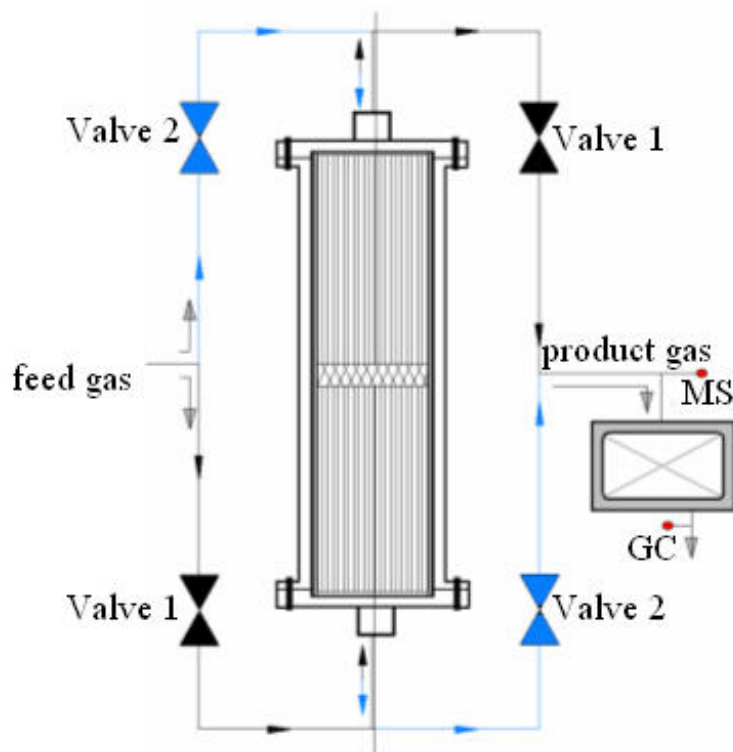


Figure 13. Schematic of the experimental reverse-flow reactor system used for investigating the partial oxidation of methane.

Switching of the flow direction through the reactor tube is accomplished with two sets of two magnetically operated valves (V1 and V2), which are positioned parallel in front of and behind the reactor. By keeping two diagonally positioned valves open while the remaining two

closed, the flow direction of the gases through the reactor is determined. Reversing the flow direction is accomplished by closing the open valves and opening the closed ones. The switching of valves as well as temperature reading is computer controlled (Labview 6.i). The reactants (CH_4 and air) were fed via standard mass-flow controllers and product gases were analyzed with a double-oven gas chromatographic system. For direct comparison of the results at reverse-flow operation with results from conventional (i.e. steady state) reactor operation, the same reactor setup was used excluding flow reversal for steady state experiments. This assured that all differences between steady state (SS) results and reverse-flow (RFR) results were exclusively due to the differences in reactor operation rather than differences in the experimental setup.

3.2 RESULTS AND DISCUSSION

3.2.1 Dynamic temperature profiles inside the catalyst and inert zones

Fig. 14 shows time-dependent temperature profiles throughout the catalyst zone and one of the inert zones at RFR operation. Temperature profiles are shown for two full periods with three different half periodicities (top row and bottom right graph) along with methane conversions and syngas selectivities as a function of half period (bottom left). The catalyst is positioned at $z = 0 - 10$ mm in the temperature profiles. In all graphs flow direction is initially from left to right.

One can recognize strongly increased catalyst inlet temperatures at all three periodicities: the gases reach the catalyst zone at temperatures well above 800°C . However, the flat contour lines for a flow reversal period of 2s (top left graph) indicate that this period is too short to allow the heat integration to function efficiently: flow reversal is too fast for the thermal dynamics of

the inert zones to follow, and an (almost) time-invariant temperature profile develops in the inert zones. Poor heat integration also results in (relatively) low conversion and selectivities as seen in the bottom left graph.

Increasing the period to 25 s, the reverse-flow operation starts to ‘pump’ the heat reservoirs very efficiently as apparent from the strong temporal temperature gradients (top right graph). This results in even higher preheat temperatures and hence strongly increased temperatures in the catalyst zone ($>1200^{\circ}\text{C}$) which lead to further increases in syngas yields.

Further increasing the period to 100s, the efficiency of the heat integration is significantly reduced again, resulting in a drop in conversion and selectivity. The reason for this lies in the exhaustion of the heat reservoir supplied by the inert zones, as apparent in the spatio-temporal temperature profiles (bottom right graph): After less than 50s in each half cycle the contour lines for the temperature close to the catalyst ($z = 10\text{-}40\text{mm}$) flatten, indicating that no further heat exchange is occurring in these areas. Hence, as soon as the temperature profiles in the inert zones start to flatten, maximum temperatures inside the catalyst zone decrease, which then leads to less selective reactions, i.e. a drop in selectivity and conversion.

Interestingly, despite the very high flow velocities in these reaction systems, the reaction front remains ‘pinned’ to one spot at reverse-flow operation (for example, they are both located roughly at 2-3 mm downstream the catalyst entrance as shown by Fig 14 where the flowrate is 2slm and $\tau / 2$ is 25 second), rather than showing the traveling front that is typically observed in a RFR [50,51]. Clearly, the kinetics of the catalytic oxidation reaction is so fast at these high temperatures that no displacement can be induced by the gas flow, and the kinetic and thermal dynamics of the reactor hence become completely uncoupled. To gain further understanding of

this phenomenon, we translated the data in Fig. 14 (for flow rate at 2slm and $\tau / 2$ 25s) in a 2-D graph at different times after the flow reversal as shown in Fig. 15.

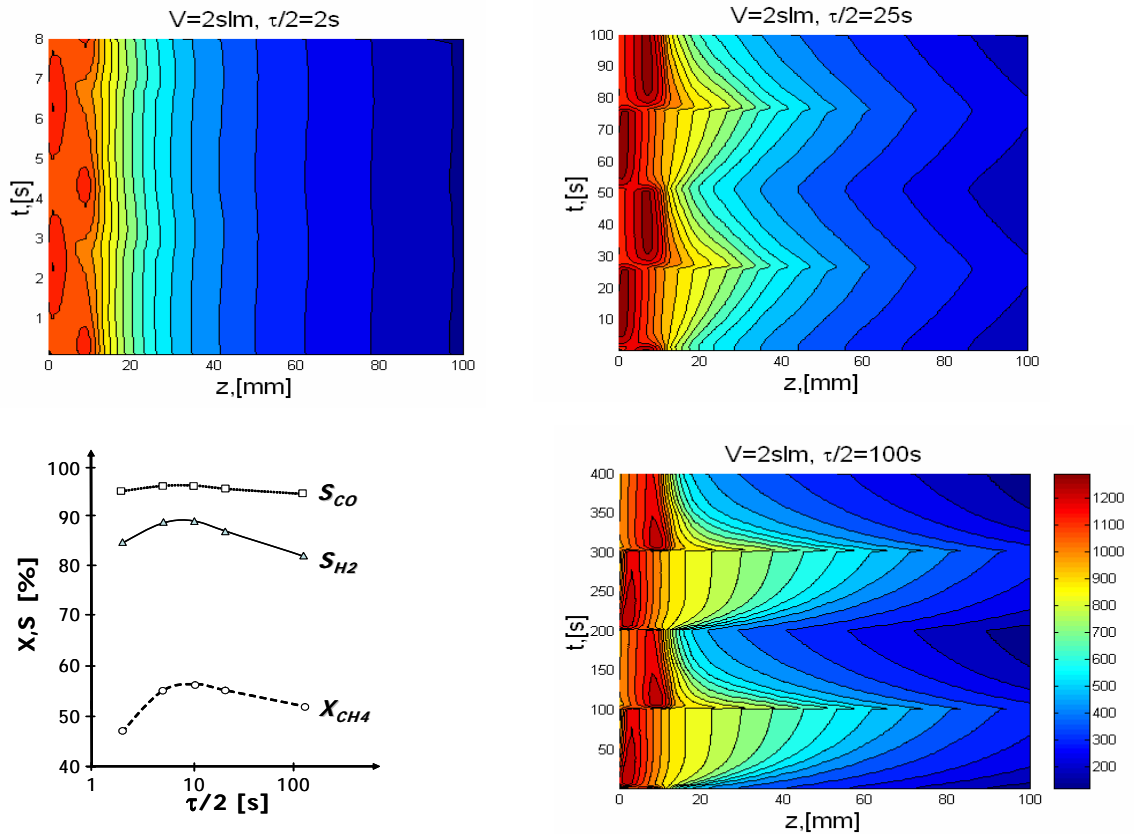


Figure 14. Spatio-temporal temperature profiles inside the catalyst ($z = 0-10\text{mm}$) and one inert zone during four half-periods (i.e. four flow reversals) for a flow reversal half-period of 2 s, 25s and 100s, respectively (clockwise from top left). The bottom left graph shows the corresponding methane conversion (circles), H_2 selectivity (triangles) and CO selectivity (squares) as a function of periodicity. $\text{CH}_4/\text{O}_2 = 2$ in methane air system.

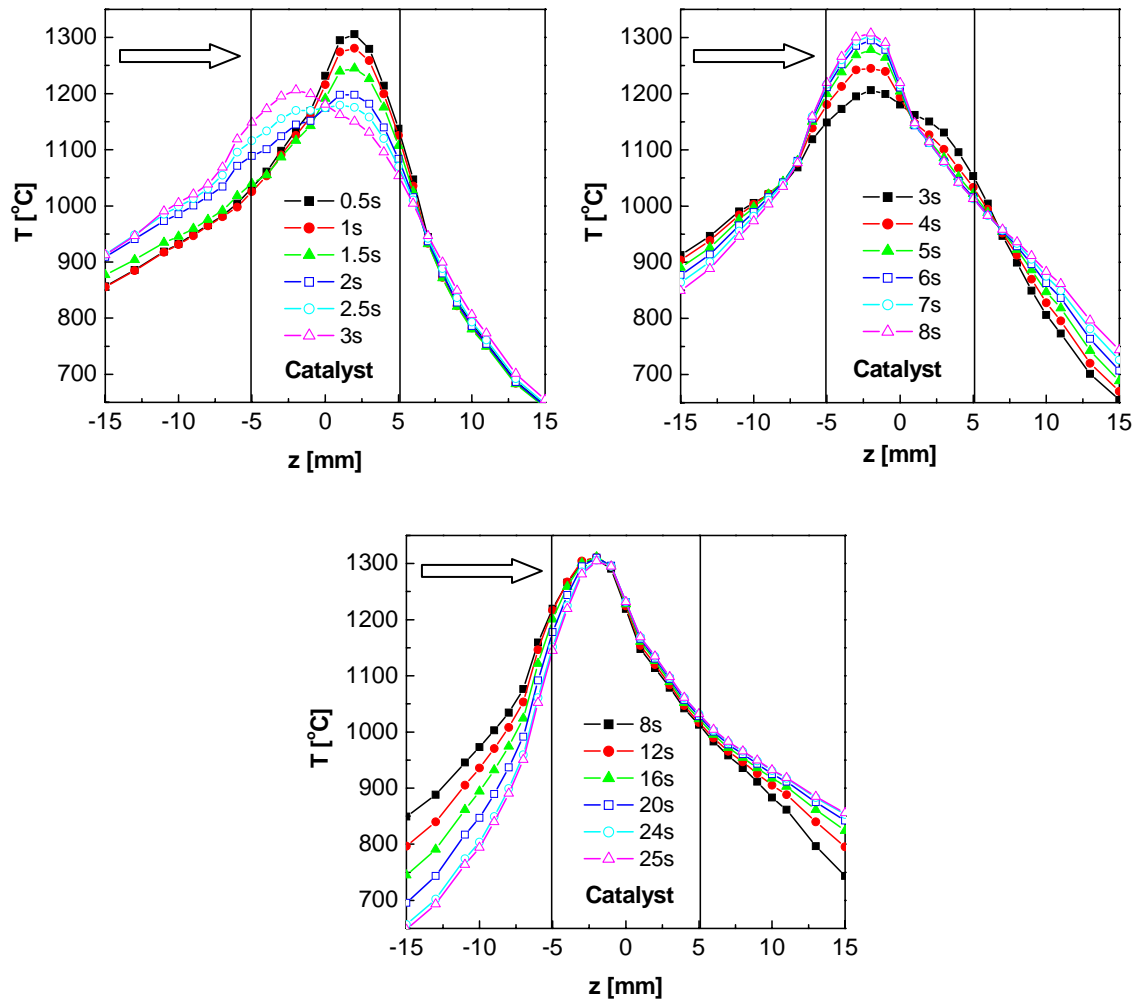


Figure 15. Dynamic temperature profiles in the catalyst and inert zones during one semi-cycle upon flow switch in RFR operation. The flow rate is 2 slm with $\text{CH}_4/\text{O}_2 = 2$ in methane/air system, $\tau/2 = 25s$.

The first graph in Fig. 15 shows the temperature profile changes from the switching of the valves at $t = 0$. As indicated by the dashed arrow in the first graph, initially ($t < 0$) gases flow from right to left. At $t = 0$, the switching of valves changes the gases flow direction and now gases flow from left to right. The two vertical lines located at -5 and 5 mm mark the

entrance/exit of the catalyst. It is seen from the first graph that during the initial 3 seconds, temperature in the downstream inert zone ($z > 5$ mm) changes slightly but the temperature inside the catalyst and in the upstream inert zone near the catalyst entrance ($z = -5$ mm) increases rapidly. The reaction front, which is represented by the maximum temperature, changes rapidly from the previously located position $z = 2.5$ mm to a new position at $z = -2.5$ mm. The temperature of the upstream inert zone near the catalyst entrance also increases rapidly. This is probably due to the radiation from the glowing reaction front. At these high temperatures, heat is most likely transferred to the nearby upstream inert zone via radiation through the straight channels of the monolith. The sharp and rapid temperature response upon flow switching indicates kinetic control, which stems from the strong exothermicity of the oxidative reaction near the catalyst entrance.

In the second graph, the temperature profile evolutions are recorded from 3 s to 8 s after flow reversal. Temperature inside the catalyst near the reaction front ($z = -2.5$ mm) still increases, but temperature in the upstream inert zone begins to decrease while temperature in the downstream inert zone begins to increase. These are the indications of convective heat transfer by the gas flows. The cold reactant gases gradually cool down the upstream inert zone while the hot exit product gases gradually heat up the downstream inert zone. The convective heat transfer in the inert zones occurs slower than the kinetically controlled process in the catalyst zone.

The third graph in Fig. 15 shows the temperature profile changes after 8s. During this period, there are only very slight changes of the temperature in the catalyst zone, while temperature in the upstream inert zone still decreases significantly. The temperature distribution inside the catalyst almost reaches a 'steady state', while the continuously fed cold reactant gases keep cooling down the temperature in the upstream inert zone, which was very hot during the

previous semi-cycle. The effect of these heat exchange characteristics results in a “cold in – cold out” reactor configuration favorable for the partial oxidation as mentioned earlier.

3.2.2 Influence of flow rate on temperature profiles

One of the major advantages of RFR over SS operation is that RFR could be operated with higher reactor throughputs [13]. On the Pt coated foam monolith catalyst, methane conversion and syngas selectivity increase with increasing gas flow rate and reach their maximum at ~3slm at SS operations. Further increases the flow rate, methane conversion and syngas selectivity begin to decrease. At RFR operations, conversion & selectivity keep increasing with increasing flow rate. We had previously used thermocamera scans to qualitatively illustrate how the heat-integration efficiency was enhanced during RFR operations at higher flow rates.

We extended our experimental conditions by increasing the total gases flow rate up to 8 slm. We observed the maximum position for CH₄ conversion and H₂ selectivity located at flow rate ~7slm at RFR operations (see Fig. 16). Further increase the flow rate to 8slm results in decreased conversion and selectivity. In comparison, the maximum conversion and selectivity occurs near 3 slm at SS operations. Therefore, RFR operations could increase the reactor operation range at least by a factor of 2, with further improved conversion and selectivity.

The above observations can also be understood through dynamic temperature studies. Fig. 9 (left) shows the temperature profiles at different flow rates at SS operations. From Fig. 9, increasing the flow rate results in decreased entrance temperature but increased maximum temperature and exit temperature. The reaction front shifts into catalyst bed with increasing flow rate. In chapter 2, we studied the reaction mechanism of CPOM on Pt coated monolith. The

reaction pathway on the Pt catalyst consists of an initial CH₄ oxidation part to dominant CO and H₂O (Eq. (6)):

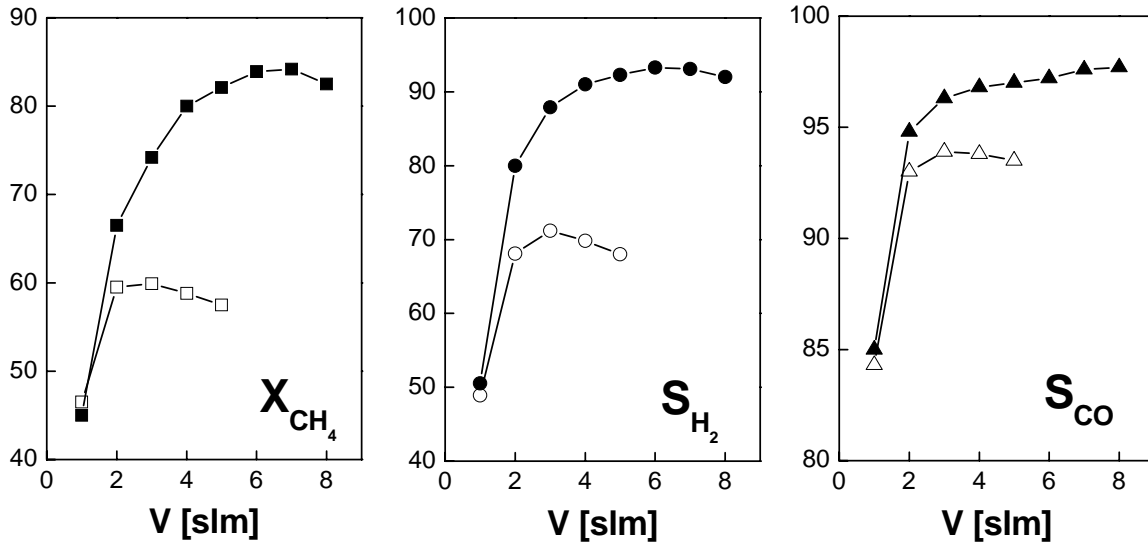


Figure 16. CH₄ conversion (X_{CH_4} left), H₂ selectivity (S_{H_2} middle), and CO selectivity (S_{CO} , right) as a function of the total volumetric gas flow rate for steady-state (SS, open symbols) and RFR (solid symbols) operation.

This reaction causes sharp temperature increase near the catalyst entrance. Followed reaction (6) is the steam reforming part which causes the strong temperature decrease in the later part of the catalyst:



Increasing the flow rate from 1 slm to 2 slm significantly increases the temperature in the catalyst which is due to increased amount of reaction heat. Therefore, both oxidation reaction (6)

and steam reforming (1) are improved, which results in enhanced conversion and selectivity. In another hand, increasing the flow rate also increases the convection heat transfer of gases. This leads to cooling down of the entrance temperature and heating up of exit temperature. The cooling down effect of entrance temperature as well as the increased gases velocity requires a longer catalyst length for the oxidation reaction to complete, as one can see from the shifting of the reaction front when changing flow rates. As a result, catalyst length for steam reforming is being cut off. Therefore, increasing the flow rate although keeps improving the oxidation reaction due to increased temperatures, steam reforming is significantly suppressed because of the decreased contact times. Since syngas production is the coupled effect of reaction (6) and (1), a maximum behavior of conversion and selectivity versus flow rate changes is observed at SS operations.

At RFR operations, heat is re-integrated into the reactor. Increased exit temperature at higher flow rates results in more efficient heat-integration. Fig. 17 shows the temperature profiles in two full cycles in the Pt catalyst and one inert zone at flow rate of 1 slm (left) and 2 slm (right) at RFR operations. One can see heat-integration efficiency is significantly improved at 2 slm than 1 slm: temperature in the catalyst zone is significantly increased; temporal temperature gradient in the inert zone is also strongly increased, which is an indication of the improved heat exchange in the inert zones.

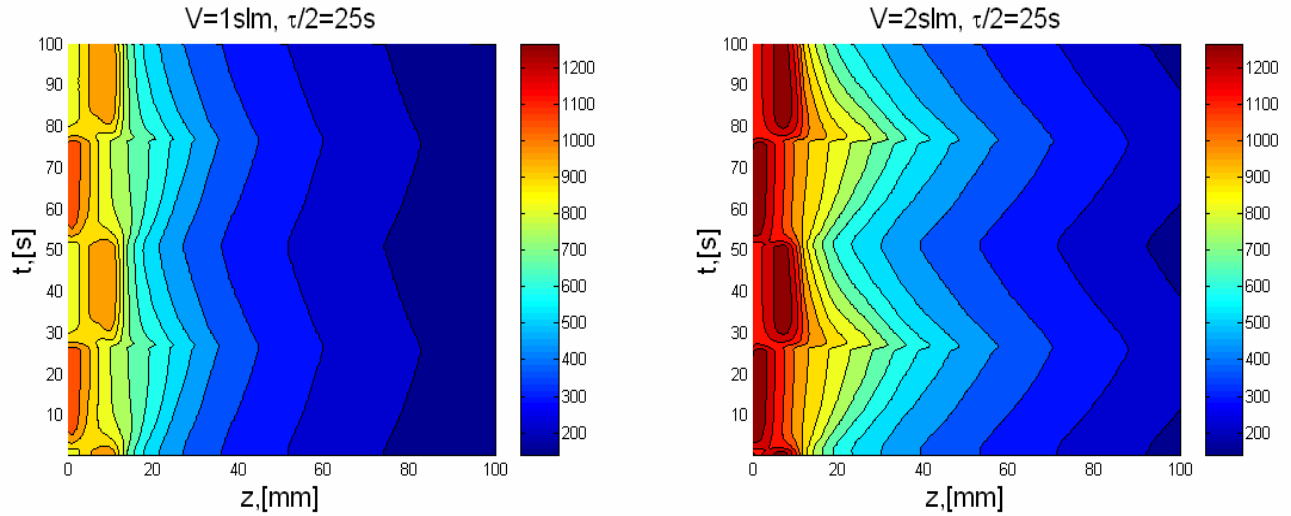


Figure 17. Temperature profiles in two full cycles on the Pt catalyst and one inert zone at 1 slm (left) and 2 slm (right) at RFR operations, $\text{CH}_4/\text{O}_2 = 2$ in methane/air system, $\tau/2 = 25$ s.

Enhanced heat-integration in RFR results in significantly increased entrance gas temperature in comparison to SS operations. The increased entrance gas temperature accelerates the direct oxidation and improves its performance in the first part of the catalyst. Thus the catalyst length needed for the oxidation part is reduced at RFR operations. Therefore, the reaction front is shortened while steam reforming part is extended in comparison to SS operations. Both the oxidation and reforming reactions are strongly improved by RFR operation, which lead to enhanced methane conversion and syngas selectivity [9,13]. While increasing the flow rate at SS operations notably shifts the reaction front into the catalyst, which results in further flattened/decreased methane conversion and H_2 selectivity as shown in Fig. 9, this shift is significantly reduced at RFR operations. One can again see from Fig. 17 that the reaction front undergoes little change in going from 1 slm to 2 slm. As a result, the maximum conversion and

selectivity occurs at a much higher flow rate (~ 7 slm). Therefore RFR can be operated with significantly increased reactor throughput with further improved syngas yields.

3.2.3 Compensation for catalyst deactivation

Catalyst stability is a very important issue for its applications. Many reasons can result in catalyst deactivation, such as sintering, poisoning, coking and metal volatilization. During our experiments, we observed metal deposition on the inert zones downstream the catalyst after prolonged reactor operation. This indicates that metal volatilization can be the reason of catalyst deactivation. The detailed deactivation mechanism is still not clear to us, however, since all of the above reasons become more significant at higher temperatures, one would expect accelerated catalyst deactivation during RFR operations given the fact that heat-integration in RFR results in significantly increased temperature in the catalyst bed. To test this hypothesis, we conducted the catalyst deactivations studies.

Shown by Fig. 18 are the methane conversion, H_2 selectivity and CO selectivity at RFR (solid symbols) as well as SS (open symbols) operations versus reaction time. During RFR operations, at some points, we switched it to SS operation and waited until the reaction system reached a stable state i.e., the temperatures at the catalyst ends are stable. We took the GC measurement and switched it back to RFR operation, as indicated by the dot arrows in the left graph. These measurements are denoted as SS in RFR and they represent the *actual* catalyst activity during RFR operations.

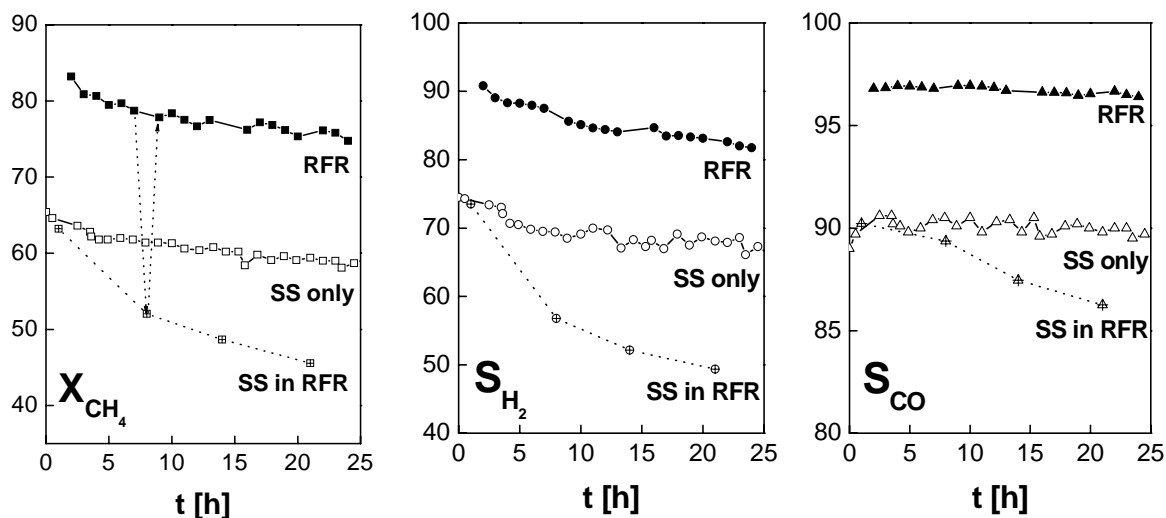


Figure 18. Catalyst deactivation at SS operation vs. RFR operation: methane conversion and syngas selectivities are shown vs. time on stream while switching between SS reactor operation (cross symbols and dotted lines) and RFR operation (close symbols and solid lines) for the Pt catalyst. Inlet gas composition was $\text{CH}_4/\text{O}_2=2$ in methane/air system at a total inlet gas flowrate of 4 slm, $\tau/2=15\text{s}$.

From Fig. 18, Pt catalyst deactivates rapidly at SS operations, as one can see the decreasing curves of methane conversion and H_2 selectivity denoted by SS only. The *actual* catalyst activity at RFR operations deactivates faster than SS operation as one can see the accelerated decreasing trends of methane conversion and H_2 selectivity denoted by SS in RFR. However, the parallel decreasing trends of methane conversion and syngas selectivity at RFR operations and SS operations indicate that no obvious acceleration of the deactivation is observed at RFR operation. Quite interestingly, RFR operation in fact compensates for the accelerated catalyst deactivation. We explained the apparently contradictory observation through the nature of the regenerative heat-integration at RFR operation [9]: Catalyst deactivation results

in increased unselective reactions which lead to increased temperature. However, while at SS operation, this increased amount of heat produced by the increasing unselective reaction is eventually carried out of the reactor by the hot product gases, RFR operations leads to a re-integration of a significant amount of this heat into the reaction system. A deactivated catalyst thus leads to improved heat-integration which then results in an intrinsic compensation of catalyst deactivation through RFR operation.

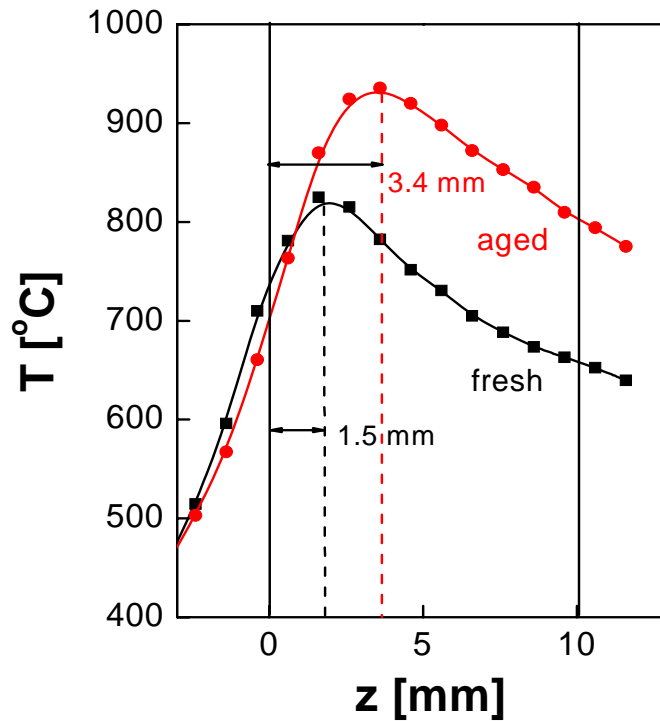


Figure 19. Temperature profile on the fresh and aged Pt catalyst at 1slm at SS operations. The deactivation was operated at total flowrate 4slm, $\text{CH}_4/\text{O}_2=2$ in methane/air system for 6 hours.

The intrinsic compensation of catalyst deactivation by RFR operation can be illustrated through the temperature profile studies. Fig. 19 shows the temperature profiles on the fresh catalyst (square) and aged catalyst (circle) at SS operations. The deactivation test was conducted at the total flow rate of 4 slm, $\text{CH}_4/\text{O}_2 = 2$ in methane/air system for 6 hours. On the fresh catalyst the reaction front is located at ~ 1.5 mm downstream the catalyst entrance. During deactivation, the overall temperature in the catalyst increases, which is an indication of increased unselective reactions due to the degradation of catalyst performance. The reaction front also gradually shifts into the catalyst bed. It locates at ~ 3.5 mm on the aged catalyst. The reaction front shifts 1.9 mm into the catalyst.

In another set of experiments, we conducted the deactivation test at RFR operations with the same total flow rate, same feed composition with switching period $\tau/2 = 15$ s for 6 hours. We compared the temperature profile at 1slm during RFR operation on both fresh and aged catalyst with the results shown in Fig. 20. From Fig. 20, on fresh catalyst (the upper graph in Fig. 20), the reaction front (indicated by dotted lines) is located ~ 0.8 mm downstream the catalyst entrance (indicated by solid lines), which is 0.7 mm shorter than that in SS operations. On the aged catalyst (the lower graph in Fig. 21), the reaction front is 2.1 mm downstream the catalyst entrance, which is 1.4 mm shorter than that in SS operation. The reaction front shifts 1.3 mm into the catalyst bed at RFR operations while it shifts 2 mm at SS operations.

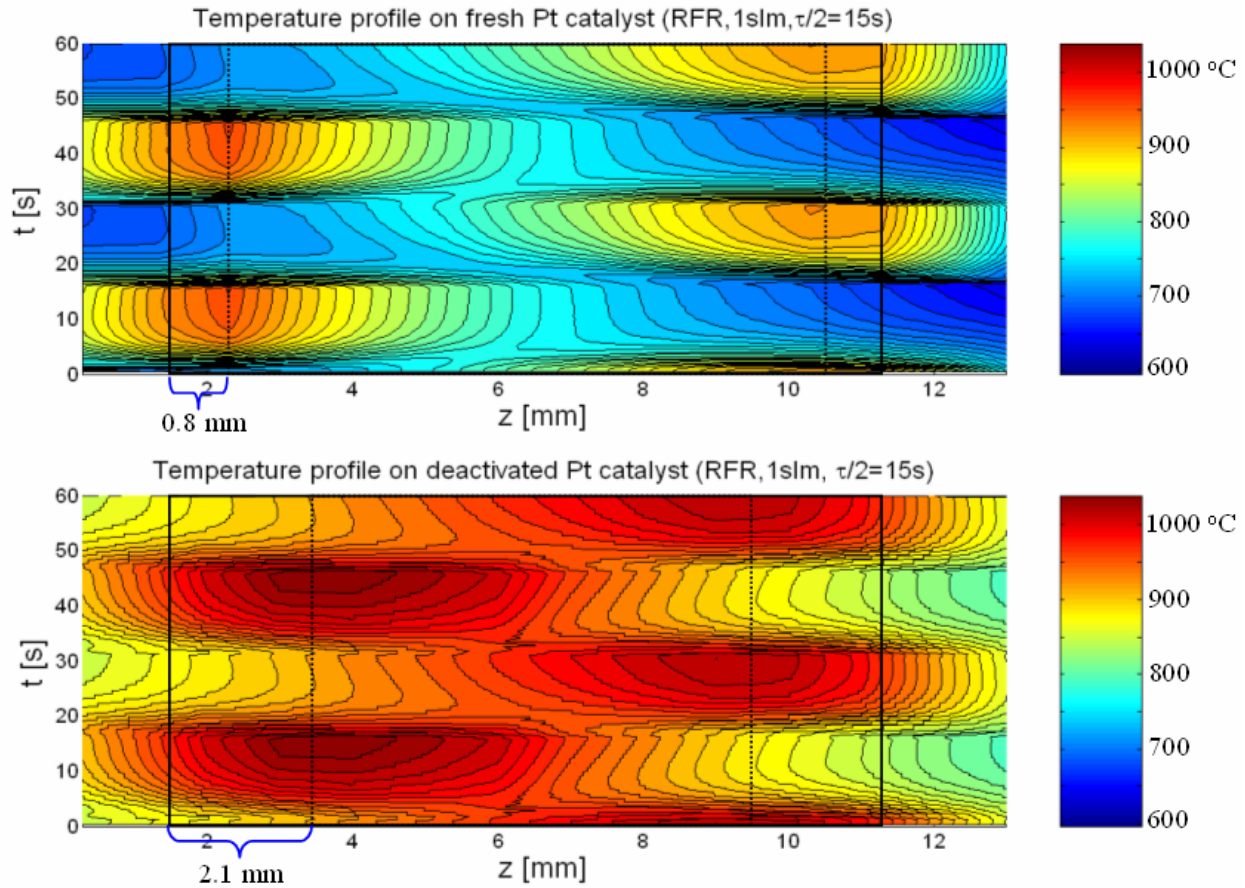


Figure 20. Temperature profile on the fresh and aged Pt catalyst at 1slm at RFR operations. The deactivation was operated at 4slm, $CH_4/O_2 = 2/1$ in methane/air system, $\tau/2=15s$ for 6 hours.

Comparing the above result, the reaction front at RFR operations is shorter than SS operations at the same inlet gases flow rate. This is because at RFR operations, feed gas enters the catalyst entrance with elevated temperature. Considering the CPOM mechanism as we have discussed in chapter 2, the elevated entrance temperature accelerates the direct oxidation reaction and shortens the catalyst length necessary for the first part, and hence extends the length for the steam reforming part. The characteristic temperature profile results in improved syngas yields.

Furthermore, RFR operation also slows down the shifting of the reaction front during deactivation and the slowing down effect retains the catalyst length for steam reforming and thus could compensate for the accelerated deactivation at higher RFR operation temperatures. It should be noted that, the nature of this compensation is exclusively an effect of heat-integration and independent of any specific deactivation mechanisms. It is universally hold and lack sensitivity to the catalyst used as we have tested with different catalysts [9].

3.3 SUMMARY

We studied the temperature dynamics during catalytic partial oxidation of methane at reverse-flow reactor operations. The aim of this study is to gain deeper understanding of the efficient heat-integration in RFR and the subsequent advantages. The influence of heat integration (and hence the conversion and selectivity) by switching frequency, volumetric inlet gases flow rate and catalyst deactivation are particularly investigated.

The results indicate that there exist two coupled effects in RFR. Temperatures in the catalyst change rapidly upon flow switching because they are kinetically controlled by the fast reaction while temperatures in the inert zones change slowly because they are thermally controlled by the slow heat transfer through gas and solid in the inert zones. The uncoupled effects reveal that heat is efficiently “centered” in the reaction zone. The efficient heat integration results in significantly increased entrance temperature. This increased entrance temperature accelerates the direct oxidation at the first part of the catalyst and improves the following steam reforming part. As a result of this characteristic temperature dynamics, RFR could be operated at higher reactor throughputs with further improved syngas yields.

Furthermore interesting, RFR operation could intrinsically compensate for the catalyst deactivation at high temperatures. Comparing to SS operations, the reaction front is shortened and the shifting of reaction front is slowed down during deactivation at RFR operations which generates a temperature profile that favors CPOM. Thus the compensation is solely an effect of heat-integration and independent of the specific catalyst used or detailed deactivation mechanisms.

The characteristics that RFR holds makes it particularly beneficial for high-temperature, short contact time catalytic processes, such as CPOM, autothermal reforming (ATR) and the catalytic oxidative dehydrogenation (ODH) of ethane to ethylene. Following this chapter, in chapter 4, we extend RFR studies onto ATR.

4.0 AUTOTHERMAL REFORMING (ATR) IN A RFR

Autothermal methane reforming (ATR) is an alternative process to steam reforming of methane (SRM) for synthesis gas and/or hydrogen production. By combining an exothermic oxidation reaction with endothermic steam reforming in one reactor, ATR meets the intensive energy demand in conventional SRM and thus allows autothermal reactor operation.



However, even ATR runs into critical autothermal operation limitations if the water-to-oxygen feed ratio is increased to optimize hydrogen production. We have shown previously that CPOM runs into autothermal limitation in that although strong exothermic combustion reactions provides high temperatures thermodynamically necessary for good syngas yields, these combustion reactions are by definition detrimental to syngas selectivities. In practice, the autothermal limitation limits the obtainable syngas yields. We have demonstrated that this thermodynamic limitation in CPOM could be overcome by heat-integration in a reverse-flow reactor (RFR), and strongly increased syngas yields were observed. Since conceptually ATR is the combination of POM and SRM, heat integration is expected to be even more crucial for optimizing syngas (and especially hydrogen) yields in ATR process.

Here, we extend our studies onto ATR over Ni catalysts. RFR and SS operations are compared by varying steam/oxygen ratio, methane/oxygen ratio, inlet gases flow rate and reverse

flow switching period. We will demonstrate in the following that heat-integration in RFR is again and even more beneficial for ATR processes.

4.1 THERMODYNAMICS

ATR runs into thermodynamic limitations at autothermal operations. This can be demonstrated through thermodynamic calculations. Shown in Fig. 21 is the hydrogen yield as a function of temperature and $\text{H}_2\text{O}/\text{CH}_4$ ratios. In these calculations, CH_4 to O_2 ratio was kept at 2, while $\text{H}_2\text{O}/\text{CH}_4$ ratio was varied from 0 to 10 and the temperature was varied from 250 to 1200 °C. We used CANTERA[52] and GRI 3.0 mechanism to conduct these calculations to determine the adiabatic temperature, methane conversion and syngas selectivities.

It is found that hydrogen yield increases with increasing $\text{H}_2\text{O}/\text{CH}_4$ ratios. Initial increasing temperature initially increases hydrogen yield while further increasing temperature results in decreased hydrogen yield. The adiabatic temperature, which is the maximum temperature a reaction system can reach autonomously, is shown as the dashed line in Fig. 21. Hydrogen yield at adiabatic operations is limited to the left of the adiabatic temperature line. In order to reach the maximum obtainable hydrogen yield, temperature has to be increased beyond the adiabatic line. Therefore, heat-integration is important for ATR.

We extended our thermodynamic calculations to a wide range of O_2/CH_4 and $\text{H}_2\text{O}/\text{CH}_4$ ratios. These calculations were conducted under adiabatic conditions: a mixture with specified compositions of CH_4 , O_2 and H_2O is ignited at 100°C (to ensure H_2O in gaseous phase) and the system then reaches the equilibrated state autonomously.

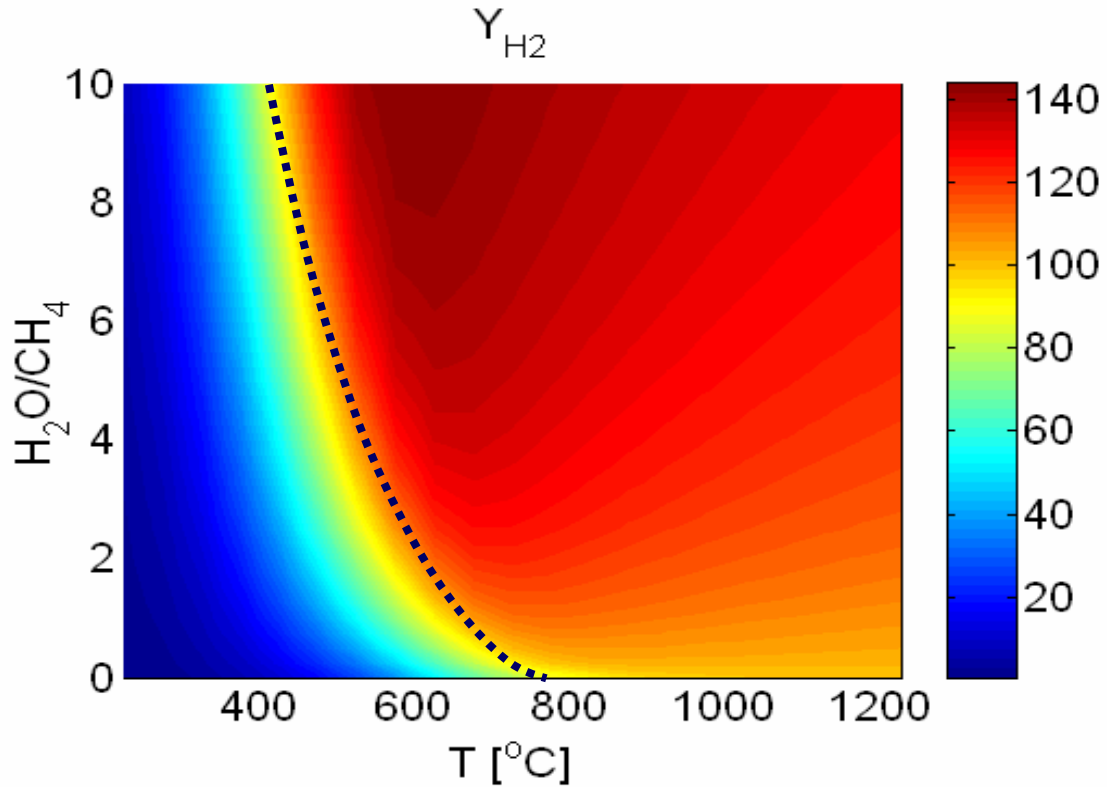
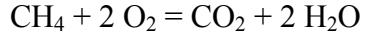


Figure 21. Thermodynamic calculations of hydrogen yield as a function of H_2O/CH_4 and isothermal temperature. Dashed line - adiabatic temperature of the system started at $100^{\circ}C$.

Shown by Fig. 22 are the thermodynamic calculation results for adiabatic temperature, methane conversion and syngas selectivities. Without H_2O addition, methane conversion initially increases rapidly with increasing O_2/CH_4 ratio. Since the main products are H_2 and CO as one can see the high selectivities for H_2 and CO , the overall reaction heat is small. As a result, adiabatic temperature is relatively low. As O_2/CH_4 is increased beyond 0.5 and further, both H_2 and CO selectivity decrease. In particular, H_2 selectivity decreases significantly. The main products shift to H_2O and CO_2 , while methane is completely converted. As a result, temperature increases drastically due to the strongly exothermic total oxidation:



$$\Delta H_R = -802 \text{ kJ/mol} \quad (4)$$

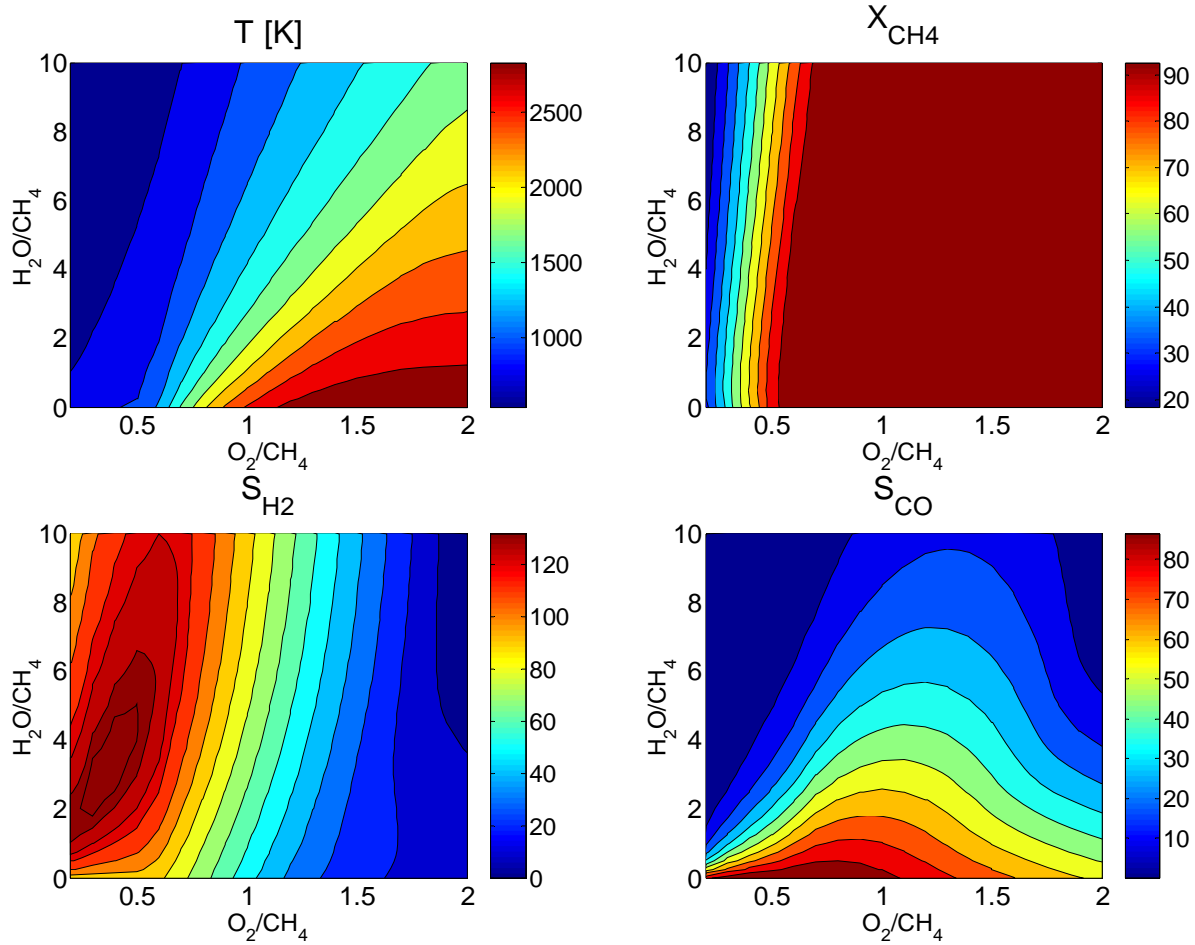


Figure 22. Thermodynamic calculations for adiabatic temperature (T), top left, methane conversion (X_{CH_4}), top right, H_2 selectivity (S_{H_2}), bottom left and CO selectivity (S_{CO}), bottom right as function of O_2/CH_4 and $\text{H}_2\text{O}/\text{CH}_4$ ratios.

Starting from different O_2/CH_4 ratios on x-axis, H_2O is gradually added into the system as denoted by $\text{H}_2\text{O}/\text{CH}_4$ ratios on y-axis. This results in marked temperature decrease. Methane

conversion only changes slightly. In fact, methane conversion initially increases slightly and then decreases mildly. Both CO and H₂ selectivities change significantly: CO selectivity decreases steeply upon water addition; while there is a maximum zone for H₂ selectivity as indicated by the contour lines.

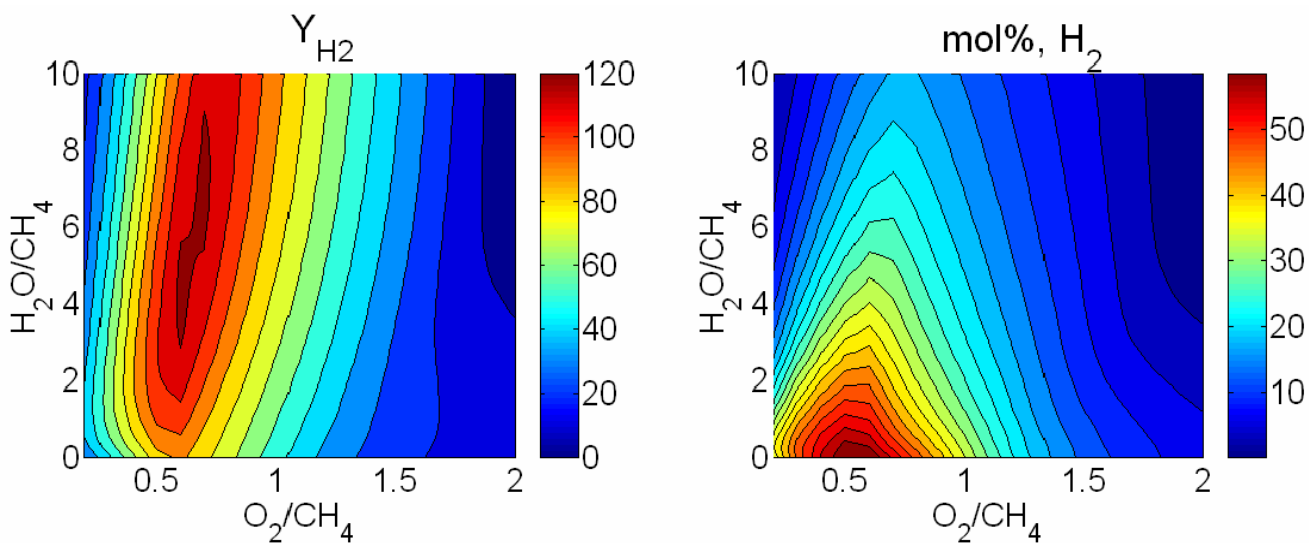


Figure 23. Thermodynamic calculations for hydrogen yields (left) and concentration (in molar fraction) in the equilibrated gases.

The yield of H₂ is calculated as the product of methane conversion and H₂ selectivity, which is shown together with equilibrated H₂ concentration (in molar fraction) in Fig. 23. Corresponding to the optimal H₂ selectivity zone in Fig. 22, there is also an optimal zone for H₂ yields. The optimal zone is located at O₂/CH₄ ratio from 0.55-0.7 and H₂O/CH₄ ratio from 3 – 9. However, H₂ concentration in the equilibrated gases decreases significantly with water addition, as indicated by the right graph in Fig. 23. Very low H₂ concentration means the ATR process is

not efficient. This trade-off effect indicates that in practice, the $\text{H}_2\text{O}/\text{CH}_4$ should be adjusted carefully for the overall process efficiency.

Fig. 24 shows the adiabatically equilibrated H_2/CO ratios. Typically, CPOM produces syngas with H_2/CO ratio near 2; SRM produces syngas with H_2/CO ratio 3, while ATR allows for much broader H_2/CO ranges as shown in Fig. 24. Typically, ATR is operated at O_2/CH_4 ratios between 0.5 and 0.6 [7,53,54]. As seen from Fig. 24, at O_2/CH_4 between 0.5 to 0.6, H_2/CO ratio in the equilibrated syngas spans from 2 to 20 with different water additions. Syngas with different H_2/CO ratios is favored at different processes. For example, syngas with H_2/CO at 2 is desired for methanol synthesis, and GTL processes; syngas with much higher H_2/CO is preferred in ammonia synthesis; hydrogen production and fuel cells. Syngas with lower H_2/CO ratio such as 1 is favored in OXO process [5]. Therefore, ATR allows for much wider range of H_2/CO ratios in syngas, which renders flexibility for downstream treatments.

From Fig. 24, adding water thermodynamically can't result in syngas with H_2/CO ratio less than 2 (for $\text{O}_2/\text{CH}_4 < 1$). In order to get syngas with lower H_2/CO , CO_2 instead of water needs to be added. Similar to the calculations for adding water, we also performed calculations with adding CO_2 to O_2/CH_4 system. Shown by Fig. 25 are the H_2/CO ratios in the equilibrated syngas upon CO_2 additions. As demonstrated, adding CO_2 can result in equilibrated syngas with lower H_2/CO ratios, even further below 1 at O_2/CH_4 less than 1. Therefore, generally, adding H_2O increases H_2/CO ratio in the product syngas, while adding CO_2 decreases H_2/CO ratio. Our studies and discussions are mainly focused on water added autothermal reforming. However, water added and CO_2 added autothermal reforming are similar to some extent, as will be described in the later part.

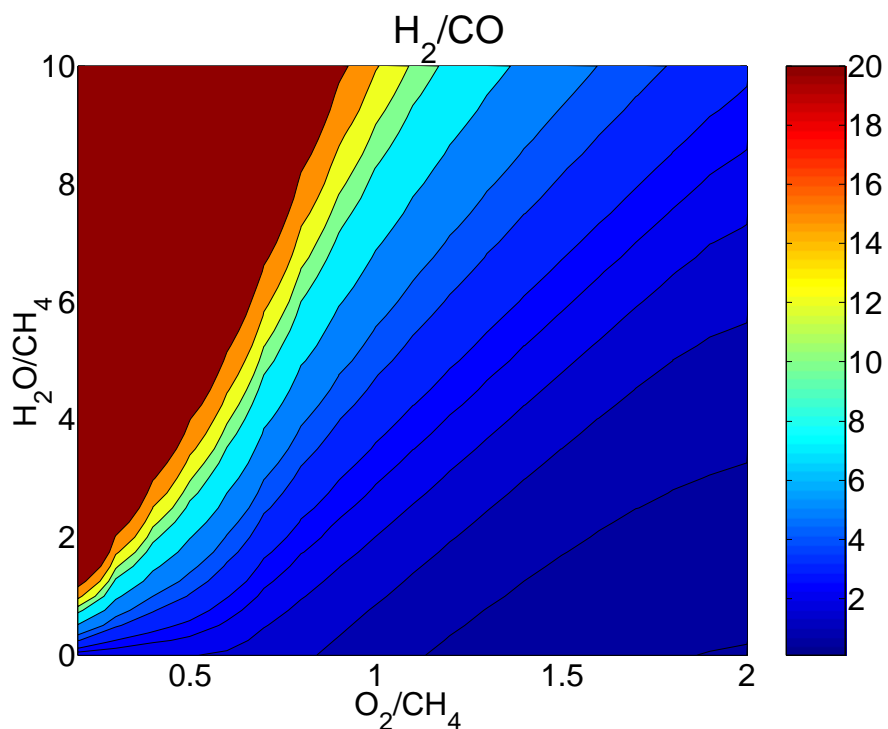


Figure 24. Thermodynamic calculations for adiabatic equilibrated H_2/CO ratios upon water additions.

Our experimental studies were carried out according to the thermodynamic calculation results: O_2/CH_4 ratios were varied from 0.25 to 0.6; H_2O/CH_4 ratios were varied from 0 to 4. These conditions include part of the theoretical optimal H_2 yield zone without going to excessive water additions. The ATR process is studied at both steady state (SS) and reverse flow operations (RFR). The difference between SS and RFR operations are demonstrated and the benefits of RFR operations are discussed in the following paragraphs.

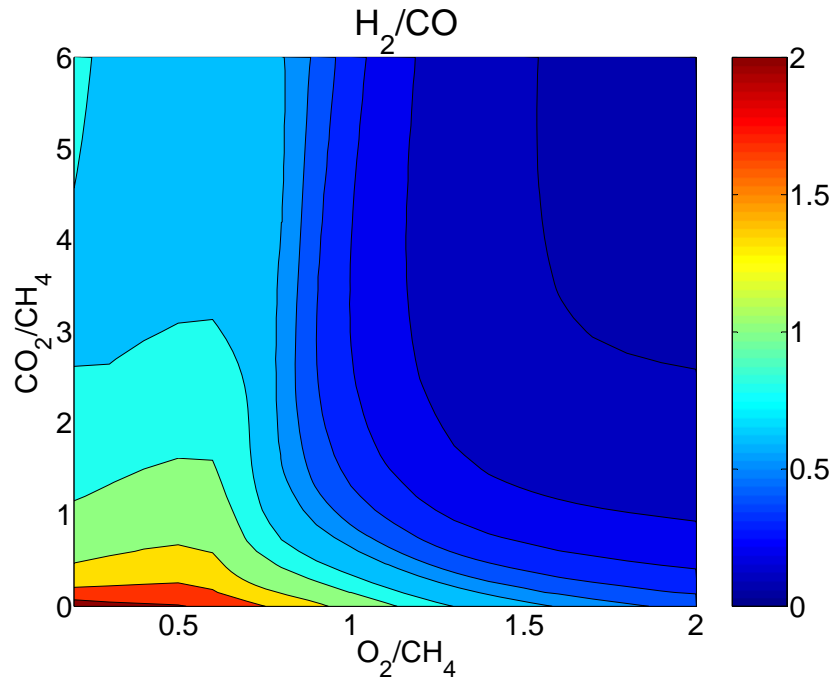


Figure 25. Thermodynamic calculations for adiabatic equilibrated H_2/CO ratios upon CO_2 additions.

4.2 EXPERIMENTAL

4.2.1 Experimental setup

Experimental setup for autothermal reforming studies consists of two reactors: a reverse-flow reactor (RFR) and a catalytic H_2 pre-burner for water co-feeding. The reverse flow reactor has been described in the previous chapters. Steam is added to the system through the H_2 pre-burner. Platinum (1 wt %) on 1/8 in alumina pellets (Alfa Aesar) are packed into a fix bed, where H_2 is catalytically oxidized in excess O_2 to form steam. The steam and remaining O_2 are then mixed with CH_4 at the exit of the pre-burner before introduced into the reverse-flow reactor tube. All

the gas lines before the RFR are heated above 100°C (~120°C) to prevent condensation of steam before autothermal reforming occurs over the catalyst in the RFR.

Catalysts used in ATR-RFR studies were Ni coated foam monolith via standard impregnation: Nickel salt solution ($(\text{C}_2\text{H}_3\text{O}_2)_2\text{Ni}$, Sigma-Aldrich) was dropped onto the alumina foam monolith [17mm OD and 10mm long; 45 ppi (pores per inch); Vesuvius High-Tech Ceramics] support. The catalyst was then calcined in N_2 stream at 600°C for 10 hrs and then reduced in 5% H_2 / 95% N_2 for 5-6 hrs. This typically results in 2 - 4 wt% Ni loading.

Temperatures were measured with type K thermocouples at both ends of the catalyst. Product gases at steady-state (SS) as well as reverse flow (RFR) operations were analyzed in a double GC system (two Shimadzu GC-14B). SS operations were conducted using the same setup for RFR while omitting the switching of flow direction. To gain a fair comparison between RFR and SS operations, RFR product concentrations were time-averaged by attaching a buffer container at the RFR exit, which mixed RFR products over 1~2 full cycles. This ensured that all differences between SS and RFR results were exclusively due to the differences in reactor operation rather than experimental setup.

4.2.2 Reactor safety

The addition of water was realized through the catalytic H_2 pre-burner. H_2 and O_2 were fed through calibrated mass flow controllers and mixed at the top of the reactor. The oxidation reaction took place on the $\text{Pt}/\text{Al}_2\text{O}_3$ surface within the narrow and tortuous channels between the randomly packed catalyst pellets. GC analysis revealed that H_2 was completely converted into H_2O . Thus, the catalytic H_2 pre-burner ensured stable steam feed. The feed gas composition to RFR can be calculated precisely through mass flow controller readouts. It is interesting to note

that although H_2 forms extremely explosive mixture with O_2 at a broad range, we did not observe any flame or explosions during our experiments, even at explosive conditions where we increased the total gas (H_2 and pure O_2) flow rate up to as high as 2.5 slm with H_2/O_2 ratio at 1. The fact demonstrates that the reactor packed with small catalyst particles, which can be viewed as a reactor with many micro-channel catalytic walls can be safe. It provides an experimental evidence for the simulation predictions from our group [55] that micro-reactors or micro-channel reactors are capable of quenching radical chain reactions and result in intrinsic reactor safety.

4.3 RESULTS AND DISCUSSION

4.3.1 Variation of H_2O addition

Shown by Fig. 26 are the methane conversion and syngas selectivities upon water addition at both SS and RFR operations at a fixed CH_4/O_2 ratio 3. Both SS and RFR operations were conducted at a total inlet gases flow rate of 2 slm. The flow reversal switching period for RFR was $\tau/2 = 25s$. At SS operations, methane conversion decreases with increasing water addition, H_2 selectivity increases significantly while CO selectivity decreases dramatically. With adding water into the system, the reaction becomes less exothermic and one observes further decreased conversion and selectivities. At even higher water additions, the reaction heat is not sufficient enough to maintain an autothermal operation: the reaction extinguishes, as one observes zero conversion and selectivities. At RFR operations, not only do we observe increased conversion and selectivities over SS operations, but more importantly, the autothermal operation range is significantly enlarged: at SS operations, autothermal operation range ends up at H_2O/CH_4 2,

while at RFR operations, autothermal operation range is increased up to H_2O/CH_4 at 4, the upper limit in our tests, with slight decreases in methane conversion, but still high H_2 selectivity. Therefore, RFR operation can improve H_2 production in a much broader range than SS operation.

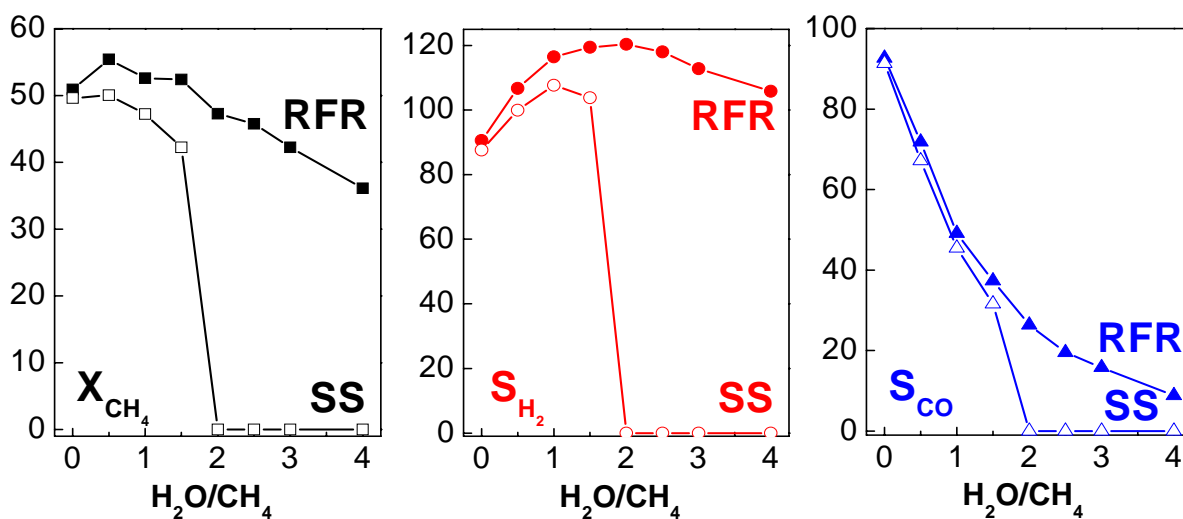


Figure 26. Methane conversion (square, left), hydrogen selectivity (circle, middle) and CO selectivity (triangle, right) as a function of water addition at both SS (open symbols) and RFR (closed symbols) operations. CH_4/O_2 ratio was kept at 3, the inlet gas ($CH_4 + O_2 + H_2O$) flow rate was 2 slm.

One might notice that in Fig. 26, H_2 selectivity can be improved beyond 100% with water addition. In water added autothermal reforming, H_2 has two sources: CH_4 and H_2O . H_2 selectivity is defined based on the converted methane (see Appendix C), that is, when all of the hydrogen atoms in the converted methane are turned in to H_2 gas, we will have H_2 selectivity as 100%.

selectivity higher than 100% means some hydrogen atoms in water are being converted to H₂ gas. From Fig. 26, H₂ selectivities are further improved beyond 100% at RFR operations than SS operations, which mean that RFR operations can convert more hydrogen atoms in water into H₂ gas.

4.3.2 Variation of O₂/CH₄ ratio

Fig. 27 shows the methane conversion and syngas selectivities at different O₂/CH₄ ratios at both SS and RFR operations. The flow reversal switching period for RFR was $\tau/2 = 25$ s. H₂O/CH₄ ratios were kept at 2 and the total flow rate was kept at 2 slm. Decreasing O₂/CH₄ ratio results in decreased conversion and selectivities. The reaction becomes less exothermic until at some point, no autothermal operation is possible----as one observes again the zero conversion and selectivities at SS operations. At RFR operations, again, one can see the conversion and selectivities are improved over SS operations and the autothermal operation ranges are increased. The improvement is more significant at lower O₂/CH₄ ratios, which indicates that the heat-integration in RFR is more beneficial at less exothermic conditions.

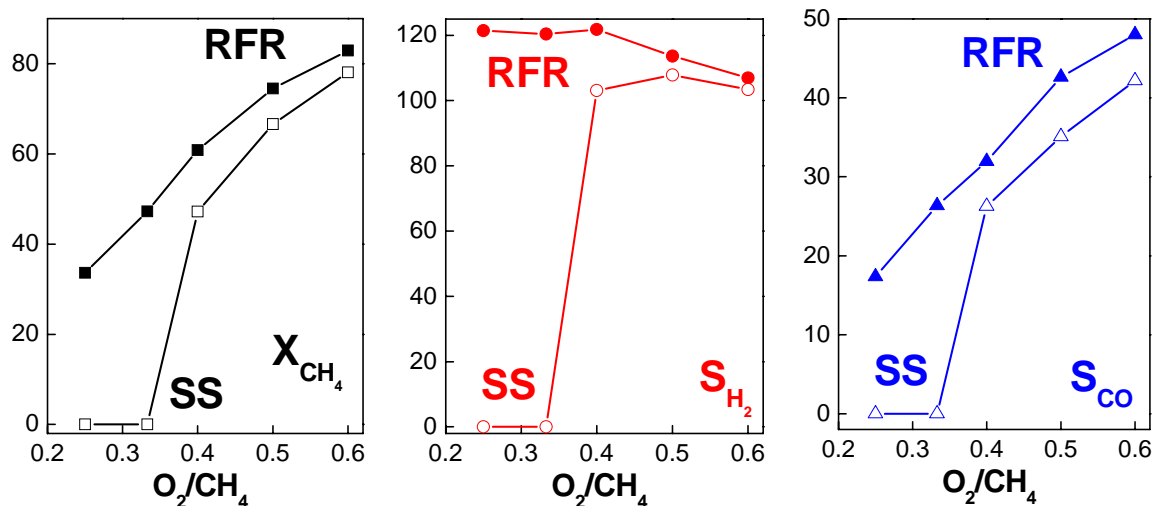


Figure 27. Methane conversion (square, left), hydrogen selectivity (circle, middle) and CO selectivity (triangle, right) as a function of O_2/CH_4 at both SS (open symbols) and RFR (closed symbols) operations. H_2O/CH_4 ratio was kept at 2, the inlet gases ($CH_4 + O_2 + H_2O$) flow rate was 2 slm.

4.3.3 H_2 yields

Shown in Fig. 28 are H_2 yields at both SS and RFR operations over the conditions we tested. In the left graph, at SS operations, the autothermal operation ranges are limited, as one observes zero yields at high H_2O addition and low O_2/CH_4 ratios. The maximum H_2 yield is near 82%. The optimal H_2 yield zone is located near x-axis, where H_2O addition is small. At RFR operations, autothermal operation ranges are significantly increased without extinction over all the conditions we tested. H_2 yield is also significantly increased particularly at less exothermic conditions as one can see from the ‘warmer’ color in the right graph in Fig. 28. Maximum H_2 yield is also increased close to 90%. The optimal H_2 yield zone is located at higher H_2O additions. According to the thermodynamic calculations, maximum H_2 yield occurs at $H_2O : CH_4$

ratio from 3 to 9. However, due to heat loss, the adiabatic calculation conditions can be rarely met at actual laboratory reactor operations. At SS operation, there is heat loss in the reactor and more importantly, significant amount of heat is being 'wasted' by the effluent product gases and therefore the maximum H₂ yield occurs at very low water addition. At RFR operations, heat is re-integrated into the reactor. Instead of being wasted, part of the reaction heat is being reutilized by the flow reversal, hence H₂ selectivity moves to higher water addition although still much lower than the thermodynamic calculation results. Detailed reactor optimization, for example, careful design and selection of heat reservoir material, gas flow rate, flow reversal switching period etc. can further shift the maximum H₂ yield toward higher water additions. However, these studies are not the focus of this thesis.

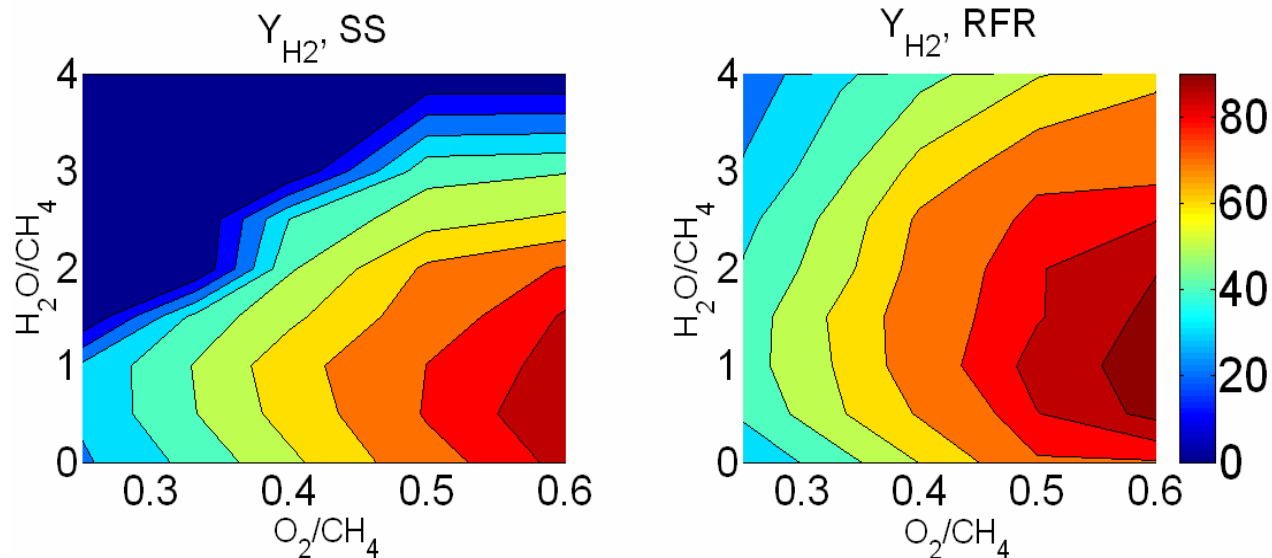


Figure 28. H₂ yields at SS (left) and RFR (right) operations. O₂/CH₄ ratio was changed from 0.25 to 0.6; H₂O/CH₄ ratio was changed from 0 to 4. Total inlet gases flow rate was 2 slm and the flow reversal switching period in RFR was $\tau/2 = 25$ s.

4.3.4 H₂/CO ratio

Shown in Fig. 29 are the H₂/CO ratios in the product syngas at both SS and RFR operations. At low H₂O/CH₄ or high O₂/CH₄ ratios, autothermal operations are possible for both SS and RFR, the resultant H₂/CO ratios are close. At higher H₂O/CH₄ or low O₂/CH₄ ratios, no autothermal reforming is possible for SS operations, so we set these values as zero. However, since RFR allows for significantly increased autothermal operation ranges, the obtainable H₂/CO ratios are also be significantly increased. The maximum obtainable H₂/CO ratio at SS operations is 7 while it can be increased up to 36 at RFR operations within the experimental conditions we conducted. Therefore, RFR operations are capable of producing much higher H₂/CO ratios in the product syngas, which makes downstream CO removal less burdened for pure H₂ production.

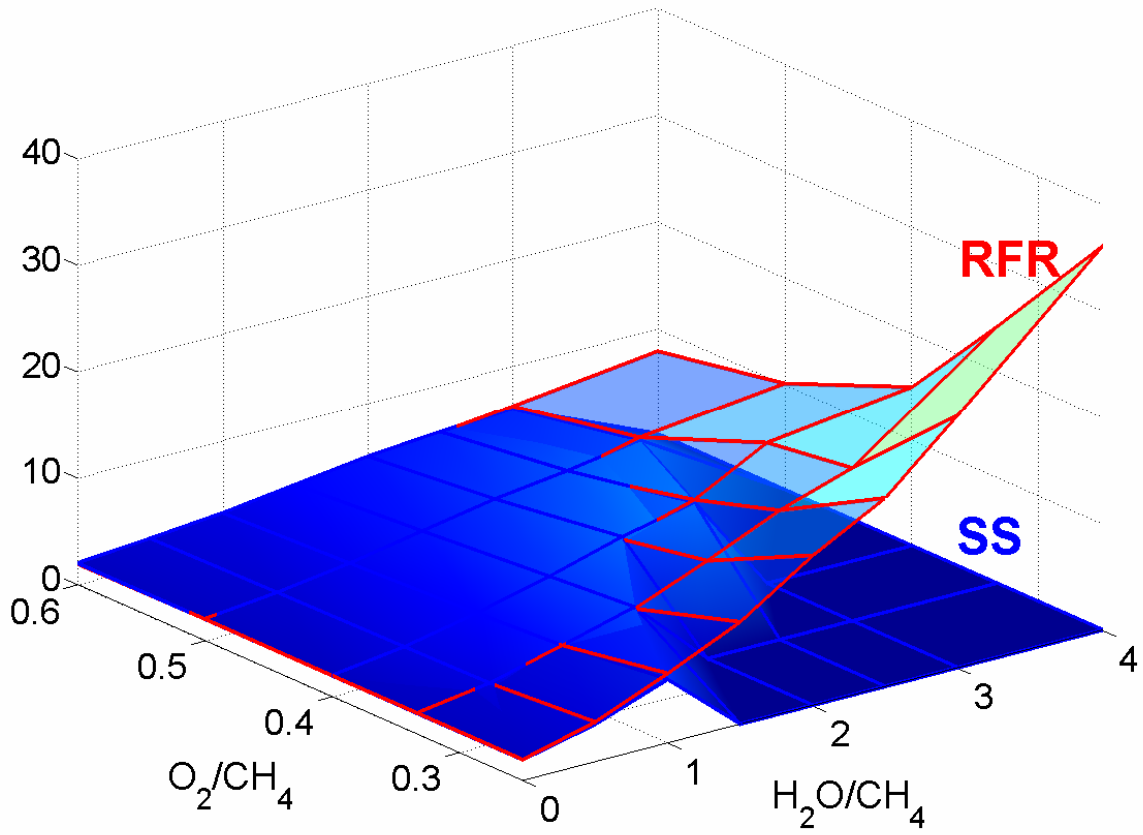


Figure 29. Comparison of product syngas H₂/CO ratio at SS (blue surface) and RFR (red surface) operations. O₂/CH₄ ratio was changed from 0.25 to 0.6; H₂O/CH₄ ratio was changed from 0 to 4. Total inlet gases flow rate was 2 slm and the flow reversal switching period in RFR was $\tau/2 = 25$ s.

4.3.5 Variation of τ and flow rate

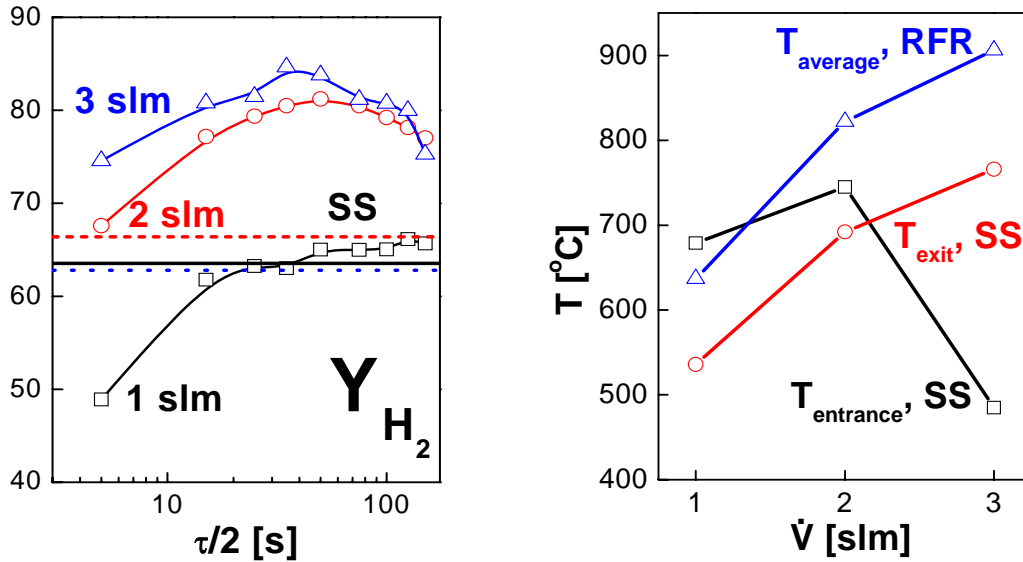


Figure 30. Left: Hydrogen yields at SS operations (horizontal lines) and RFR operations at different flow rate (1slm – 3slm) and different flow reversal switching periods ($\tau/2$). The feed gas composition was $O_2/CH_4/H_2O = 0.5/1/2$. Right: Temperature at catalyst entrance and exit during SS operations as well as average temperature at catalyst ends during RFR operations at different flow rates. The flow reversal switching period ($\tau/2$) was 25 seconds and the feed gas composition was $O_2/CH_4/H_2O = 0.5/1/2$.

In chapter 3, we demonstrated that the flow reversal period $\tau/2$ is an important operation parameter. There is an optimal τ corresponding to the most efficient heat integration in RFR. We also studied the influence of τ during ATR-RFR operations. Shown in the left graph in Fig. 30 are the influences of flow reversal switching period ($\tau/2$) on hydrogen yields at different flow rates during RFR operations (solid lines with open symbols). One observes that hydrogen yields

are strongly dependent on the flow reversal switching period ($\tau/2$). There is an optimal switching period for optimal hydrogen yield, which corresponds to the most efficient heat-integration in the RFR, similar to what we have demonstrated in chapter 3 for CPOM-RFR. The optimal switching period shifts to shorter time-scales with increasing flow rates because at higher flow rates, the increased heat-transfer rate in the reactor exhausts the heat reservoir faster.

We also demonstrated that heat-integration in RFR results in significantly increased reactor throughput which allows more compact reactors possible. Similarly, we also study the influence of flow rate on ATR-RFR operations as also shown in Fig. 30. For comparison, hydrogen yields at SS operations are shown in the left graph in Fig. 30 as the horizontal lines. At 1slm, RFR operations (shown in black solid line with open squares) barely result in any increase in hydrogen yields compared to SS operations (shown in black dash line). Increasing the flow rate to 2slm, hydrogen yields are significantly improved at RFR operations (shown in red solid line with open circles) over SS operation (shown in red dash line). Further increase the flow rate to 3 slm, hydrogen yield at SS operations (shown in blue dot line) is decreased from 2 slm, while it is further increased at RFR operations (shown in blue solid line with open triangles). This observation is explained through temperature studies shown in the right graph. At SS operations, increasing the flow rate from 1 slm to 2slm increases the overall reaction heat at autothermal operations. Both temperatures at the catalyst entrance and catalyst exit are increased, which result in increased hydrogen yields. Further increases the flow rate to 3 slm, the increased flow rate causes a cooling down effect of catalyst entrance while a heating up effect of catalyst exit. The reaction front shifts into the catalyst. This leads to decreased hydrogen yields. At RFR operations, heat is re-integrated into the reactor. Increasing flow rate results in increased catalyst exit temperature at SS operations which will then result in more efficient heat-integration at RFR

operations. Therefore, hydrogen yields are increased with increasing flow rate. These results are in agreement with the experimental observations as catalytic partial oxidation in a reverse-flow reactor as we have demonstrated previously [13]. RFR operation therefore allows for higher reactor throughputs with further improved hydrogen yields or RFR operation allows for even shorter contact time and more compact reactor volumes which make it particularly suited for small scale hydrogen productions.

4.3.6 ATR Mechanism

In Fig. 26, we found that upon water addition, methane conversion changes slightly, hydrogen selectivity increases, while CO selectivity decreases significantly. This indicates that water gas shift reaction plays a significant role (WGS, Eq. 2).



Therefore, in water added autothermal reforming, the main reaction pathway is partial oxidation and water gas shift reaction. In our previous studies, we found that partial oxidation in fact consists of two sections: an initial oxidation to predominant CO and H₂O, followed by predominant steam reforming and some WGS. Adding water in ATR increases the WGS in the second part of the catalyst. WGS results in increased H₂ while decreased CO concentration and thereby increased H₂/CO ratios in the product syngas. Our thermodynamic calculations which are shown in Fig. 23 also indicate that water gas shift reaction is thermodynamically favorable: In Fig. 23, when adding water, the adiabatic temperature decreases, methane conversion changes slightly, H₂ selectivity increases significantly while CO selectivity decreases significantly.

Similarly, for CO₂ added autothermal reforming, adding CO₂ will increase the reverse water gas shift reaction (RWGS, Eq. 8) in the second part of the catalyst.



The RWGS results in decreased H₂ while increased CO concentration and thereby decreased H₂/CO ratios in the product syngas. Thermodynamic calculations also verified this speculation, with the H₂/CO ratios shown in Fig. 26. According to these thermodynamic calculations, adiabatic temperature at both steam added and CO₂ added autothermal reforming conditions decreases with increasing H₂O/CH₄ or CO₂/CH₄ ratios. Our experimental results reveal that RFR operations can improve syngas/H₂ yields as well as the autothermal operation ranges over SS operations during water added autothermal reforming. Since CO₂ added autothermal reforming is intrinsically similar to steam added autothermal reforming, we expect RFR operation should also be beneficial for CO₂ added autothermal reforming.

4.3.7 Autothermal reforming economics

Compared to SRM, CPOM does not require intensive energy input to sustain the reaction and thereby can be operated autothermally. However, for large-scale industrial applications, pure oxygen is needed to run the reaction. The additional oxygen plant for commercial size CPOM operation needs significant energy input as well as large investment costs and thereby counteracts this benefit. In water added ATR, hydrogen production is maximized through the addition of water, while the overall reaction is still exothermic and thereby autothermal operation still possible. To produce the same amount of H₂, ATR consumes less oxygen than CPOM since ATR utilizes source of the oxygen in the steam feed. Therefore, ATR is more economical than CPOM for the production of H₂ from methane. Our studies show that coupled ATR with RFR operations could convert more hydrogen atoms in water into H₂ gas than SS operations, therefore, to produce the same amount of hydrogen, ATR-RFR needs least oxygen consumption.

Considering the large energy as well as operational cost for an oxygen plant, ATR-RFR should be a particularly economical way for the production of hydrogen from methane.

4.4 SUMMARY

We studied hydrogen production via autothermal reforming over Ni catalyst in a reverse-flow reactor (RFR). Thermodynamic calculations show that in order to get optimal H₂ yields, reaction temperature needs to be increased beyond adiabatic temperature rise. Therefore, heat-integration is very important. At SS operations, autothermal operation range is limited by the decreasing reaction exothermicity at high H₂O: CH₄ or low O₂ : CH₄ ratios. At RFR operations, autothermal operation range is significantly increased with further improved methane conversion and syngas and particularly H₂ selectivities. As a result, H₂ yields and obtainable H₂/CO ratios are also greatly improved. The improvements in H₂ yields are particularly pronounced for very high flow rates (i.e. very short contact times), which makes the ATR-RFR process particularly well suited for small-scale and decentralized hydrogen production.

5.0 NANOCOMPOSITE OXYGEN CARRIERS FOR CHEMICAL LOOPING COMBUSTION (CLC)

In the previous chapters, we have demonstrated that the efficient heat-integration by periodic switched flows in a reverse flow reactor (RFR) can successfully overcome thermodynamic limitations during autothermal operations for CPOM and ATR and results in significantly increased syngas and/or hydrogen yields, increased reactor throughput and increased autothermal operation ranges. The process intensification goals are well achieved through the integration of reaction and heat exchange in a single tube. In this chapter, we will discuss our studies on developing nanocomposite material as oxygen carriers for chemical looping combustion (CLC). CLC integrates reaction (fuel combustion) with heat exchange (via solid carriers) in a dynamic, cyclic system. Therefore, CLC is similar to RFR operation in that both processes operate dynamically and cyclically. However, In a RFR, catalyst and inert zones (solid material) are fixed in the reactor and gas flow directions are switched, while in CLC, gas (fuel and air) flow directions are fixed and solid oxygen carriers are circulated between the two inter-connected reactors.

High temperature and periodically changed redox atmosphere require strict stability of the solid oxygen carriers. Conventionally prepared oxygen carriers suffer from sintering as well as slow re-oxidation kinetics which we will discuss in the later part of this chapter. In this

chapter, we will report a significant step toward developing high temperature stable nanocomposite oxygen carriers.

‘Nanoscaled’ materials have become the focus of intense research in catalysis and material science due to the high reactivity, large surface area, as well as fundamentally changed physical and chemical properties of materials on the nanoscale [56,57]. However, their practical application is to-date limited to low temperature conditions due to the lack of thermal stability of the highly energetic nanoparticles. In previous work from our lab, we have demonstrated that through appropriately tailored nanocomposite materials catalytic metal nanoparticles can be stabilized to very high temperatures, and the high reactivity of nanoparticles can thus be reconciled with the often harsh demands of a technical process [17,18,58]. In these studies, we demonstrate the application of this principle to the synthesis of highly efficient oxygen carriers for chemical looping combustion, i.e. we demonstrate that such nanocomposite materials can even withstand the repeated oxidation-reduction cycles that characterize the cyclic operation of a chemical looping combustor. The nanostructured oxygen carrier can also successfully overcome the diffusion limitations during re-oxidation and thus is a multifunctional material.

5.1 EXPERIMENTAL

5.1.1 Synthesis and characterization of oxygen carriers

The synthesis of the nanocomposite carriers, which is schematically shown in Fig. 31, is based on a route previously developed in our laboratory for nanocomposite high-temperature catalysts [58]. The synthesis is based on a reverse-microemulsion templated route, in which the metal

nanoparticles are synthesized in a simple one-pot synthesis simultaneously with a high-temperature stable ceramic matrix (here: barium-hexaaluminate, 'BHA', Appendix B). For this purpose, a reverse microemulsion is prepared by mixing an aqueous solution of ($\text{FeCl}_3 \cdot 6 \text{H}_2\text{O}$ (>99.0%) for Fe, $\text{Ni}(\text{NO}_3)_3 \cdot 6 \text{H}_2\text{O}$ (99.999%) for Ni, $\text{Cu}(\text{NO}_3)_2 \cdot 2.5 \text{H}_2\text{O}$ (99.99%) for Cu, and $\text{Co}(\text{NO}_3)_2 \cdot 6\text{H}_2\text{O}$ (>99.0%) for Co, all from Aldrich) with isooctane (2,2,4-trimethylpentane, 99.7% Aldrich) and a surfactant (poly(ethylene oxide)-*block*- poly(propylene oxide)-*block*-poly(ethylene oxide) with 10 wt% ethylene oxide, Aldrich). 1-pentanol (99+%, Aldrich) is added as a co-surfactant to obtain a Winsor type IV system. Aluminum isopropoxide and barium isopropoxide (both 99.9%, Aldrich) at a stoichiometric ratio of 1 to 12 are dissolved in dry isopropanol before addition to the reverse microemulsion. The isopropoxides diffuse through the oil phase and the surfactant shell into the aqueous phase of the micelles where they hydrolyze to form a Barium-aluminate structure. After aging for 48 hours, the water phase and the organic phase are separated via temperature-induced phase separation (TIPS). The product phase is then washed several times with acetone, and remaining volatile residues are removed via freeze drying. This synthesis results in powders which are calcined for 5 hours in air at 600°C.

As reference material, conventional Me-Bentonite (Me for Ni, Fe and Cu) oxygen carriers were prepared by mixing dry powders of nickel oxide and bentonite (weight ratio NiO: bentonite = 3:2) at the National Energy Technology Laboratory (NETL). Deionized water was added to the powder mixture to obtain a paste, and the paste was then dried at 105°C for 24 h, calcined at 900°C for 6 h, and finally crushed to obtain small particles. Oxygen carriers were characterized by XRD, SEM/EDX, TEM, and BET techniques. We will focus our discussion predominantly on Ni in this chapter; however, the results from Fe, Cu and Co will also be discussed.

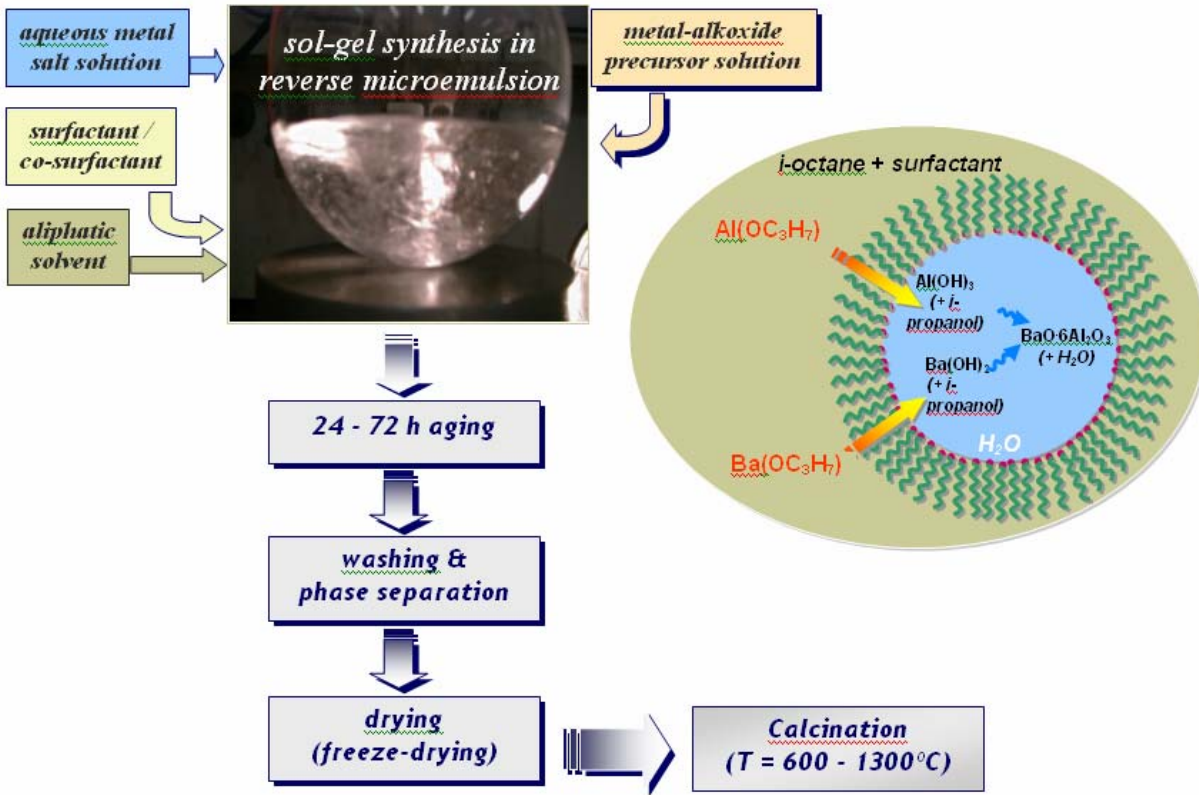


Figure 31. Synthesis schema of nanocomposite oxygen carriers.

5.1.2 Reactive evaluation

Both types of oxygen carriers (nanocomposites and conventional) were evaluated with regard to their suitability as oxygen carriers by subjecting them to repeated oxidation-reduction cycles and monitoring the sample weight via online thermogravimetric analysis (TGA) as measure for the oxidation state of the samples.

During these cycles, the samples (typical sample weight 20–100 mg) were oxidized for 1 hour in a purified air stream at (fixed) temperatures between 700°C and 900°C, and then reduced

for 10 min. at the same temperature in contact with a typical (dry) synthesis gas (simulated ‘coal gas’: 12vol% CO, 36vol% CO₂, 27vol% H₂, balance: He). For safety purposes, the oxidation and reduction half-cycles were separated by 5 min. purge cycles with pure nitrogen to avoid uncontrolled mixing of synthesis gas with air after switching of the feed gases. In a typical experiment, the oxygen carriers were subjected to ten oxidation-reduction cycles for a total duration of about 900 minutes.

The kinetics of the resulting oxidation-reduction curves were evaluated based on a shrinking core model in order to elucidate the rate-controlling step and to obtain the characteristic time constant for the process as detailed further below.

5.2 RESULTS AND DISCUSSION

5.2.1 TEM

The synthesis results in nanocomposite materials, where metal (Ni in Fig. 32 top) nanoparticles with average particle sizes of about 10 nm and narrow size distributions are embedded in the ceramic matrix. The materials are characterized by an irregular, highly porous structure with pure textural porosity and a very homogeneous distribution of the metal in the ceramic matrix. Samples with different weight loadings between 15wt% and 37wt% Ni were prepared and characterized by TEM. It is found that the average Ni particle size does not change very much with increasing metal weight loading, while metal particle site density increases with increasing metal weight loading.

For comparison, TEM image of conventionally prepared Ni-Bentonite (60wt%) is also shown in the bottom picture in Fig. 32. Ni-Bentonite contains mainly irregular, big (> 200 nm) primary particles.

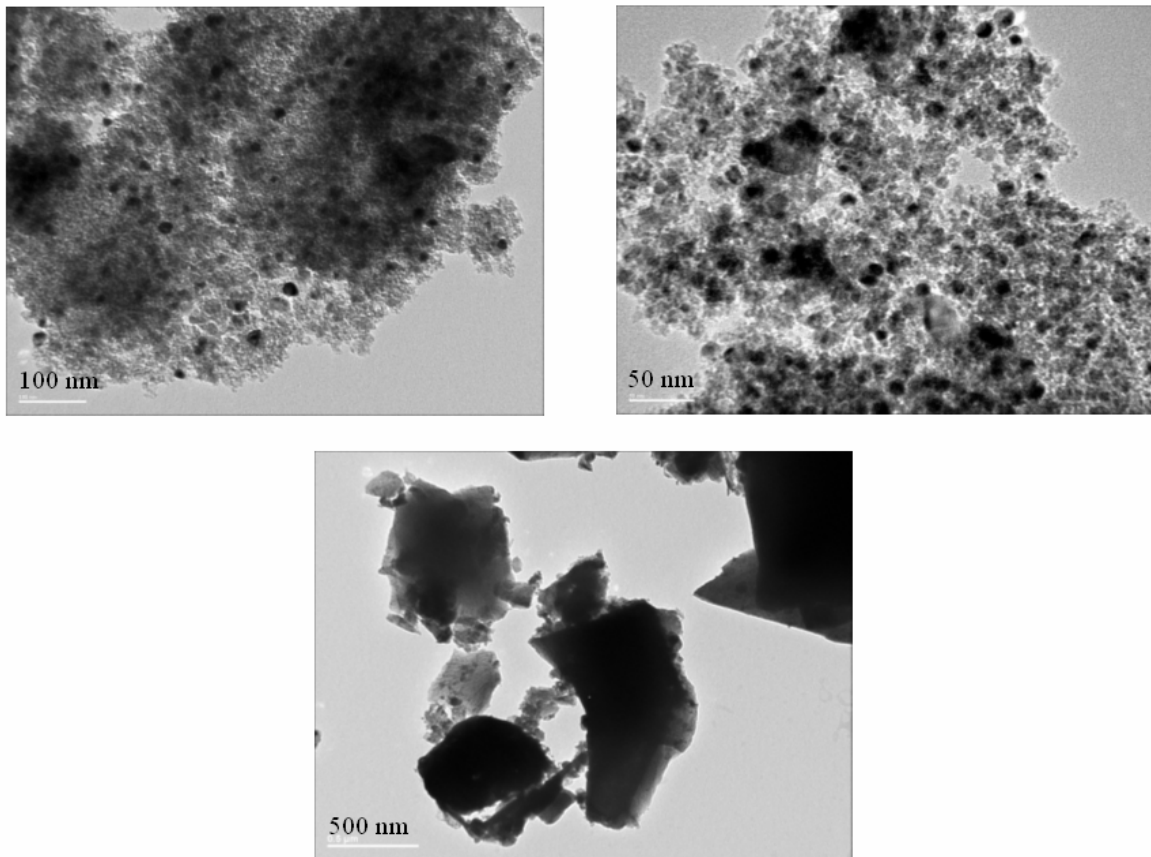


Figure 32. TEM images of Ni-BHA (15wt%, upper left, 26wt%, upper right) and Ni-Bentonite (lower).

5.2.2 XRD

The nanocomposite samples were characterized by XRD (Philips PW1830, using Cu $K\alpha$ radiation) after oxidation in ambient, flowing air and after reduction in a flow of 5vol% H_2 in N_2

(both for 1h @ 800°C) in order to evaluate the basic redox stability of the Ni nanoparticles as well as the ceramic structure in the nanocomposites. Figure 33 shows XRD spectra after several such redox cycles. The spectra indicate that the Ni particles are completely oxidized and reduced in the redox cycles, while the ceramic phase remains unaffected. A Debye-Scherrer analysis yields 14 nm and 18 nm as average particles sizes for the reduced and oxidized Ni particles, respectively, which is in good agreement with TEM measurements of the samples (not shown) and with the theoretical expected volume change of the Ni nanoparticles during oxidation. This indicates that the nanoparticles are stable during redox cycles, i.e. that the embedding of the nanoparticles efficiently avoids sintering despite the fairly demanding conditions of complete oxidation and reduction of these particles.

Fig. 34 shows the XRD spectra for Ni_BHA nanocomposite samples with different weight loadings. The vertical lines mark the diffraction from metallic Ni. It is found that, the peak width does not change much with increasing weight loading, which indicates that the primary Ni particle sizes are virtually unchanged with increasing weight loading. The signal intensity increases with increasing metal weight loading, which is due to the increased metal site density. These observations agree well with TEM images, as shown in Fig. 32.

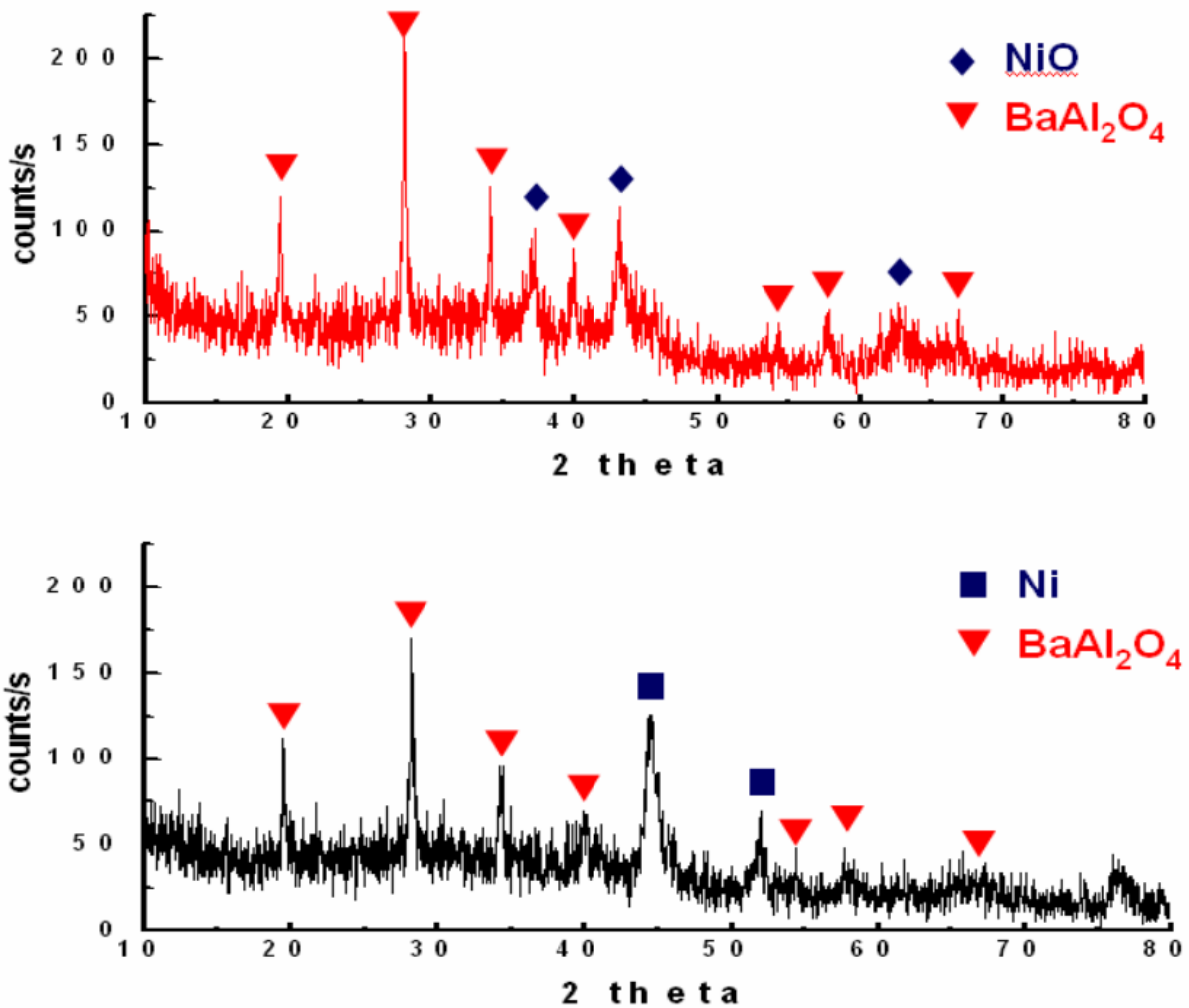


Figure 33. XRD spectra for a 15wt% Ni-BHA nanocomposite sample after oxidation (top) and reduction (bottom).

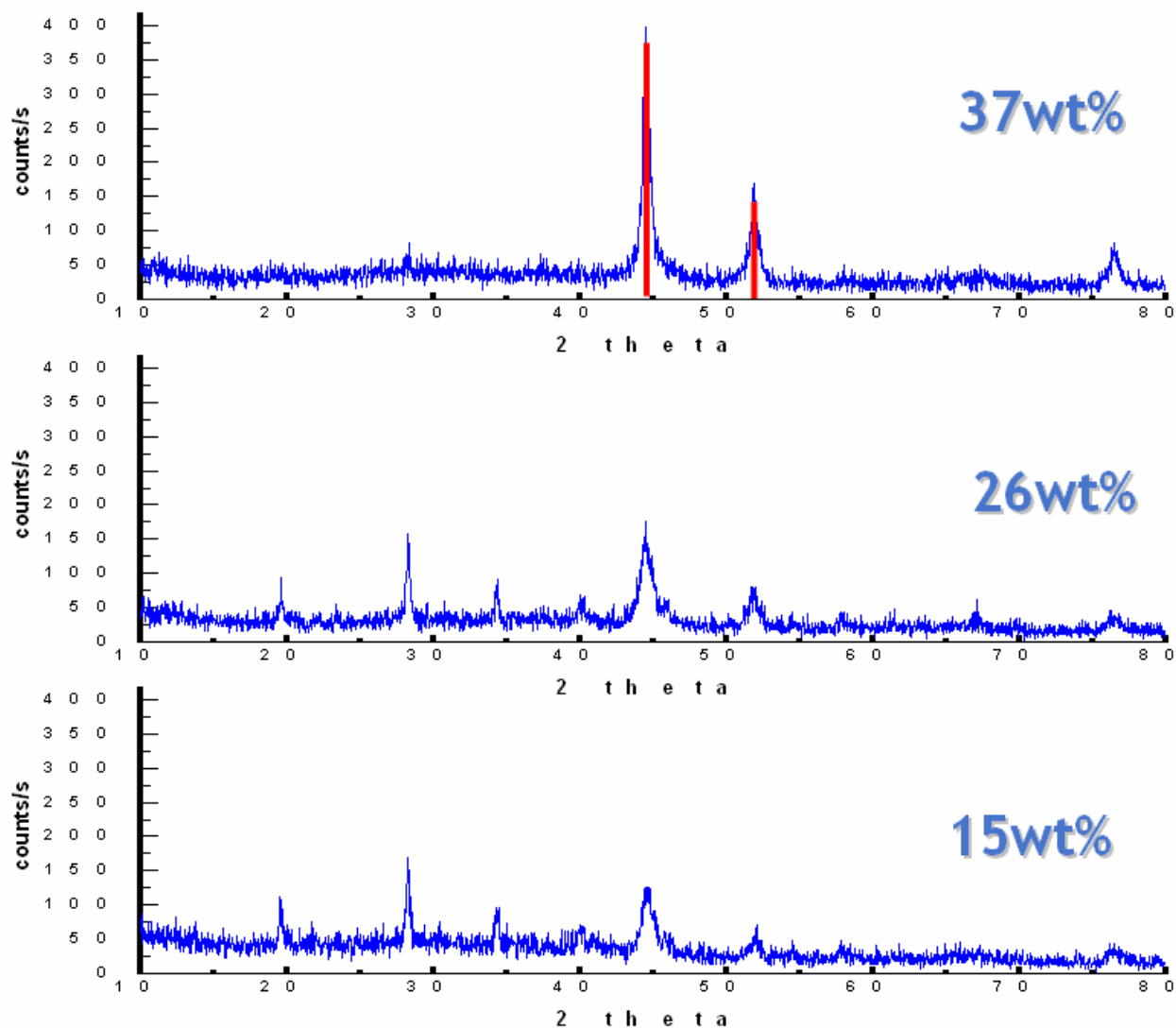


Figure 34. XRD spectra for 15wt%, 26 wt% and 37wt% Ni-BHA nanocomposite samples.

5.2.3 BET and pore structure

Shown in Fig. 35 are the liquid N₂ adsorption isotherms for Ni-BHA (40wt%, left ordinate) and Ni_Bentonite with 60 mesh size (60wt% metal oxide loading, right ordinate). BET analysis were conducted in ASAP 2020 (Micromeritics) with liquid N₂ at 73.15K. The Ni-BHA adsorption

isotherm represents a typical type IV mesoporous material, while Ni-Bentonite adsorption isotherm reveals a purely macroporous material.

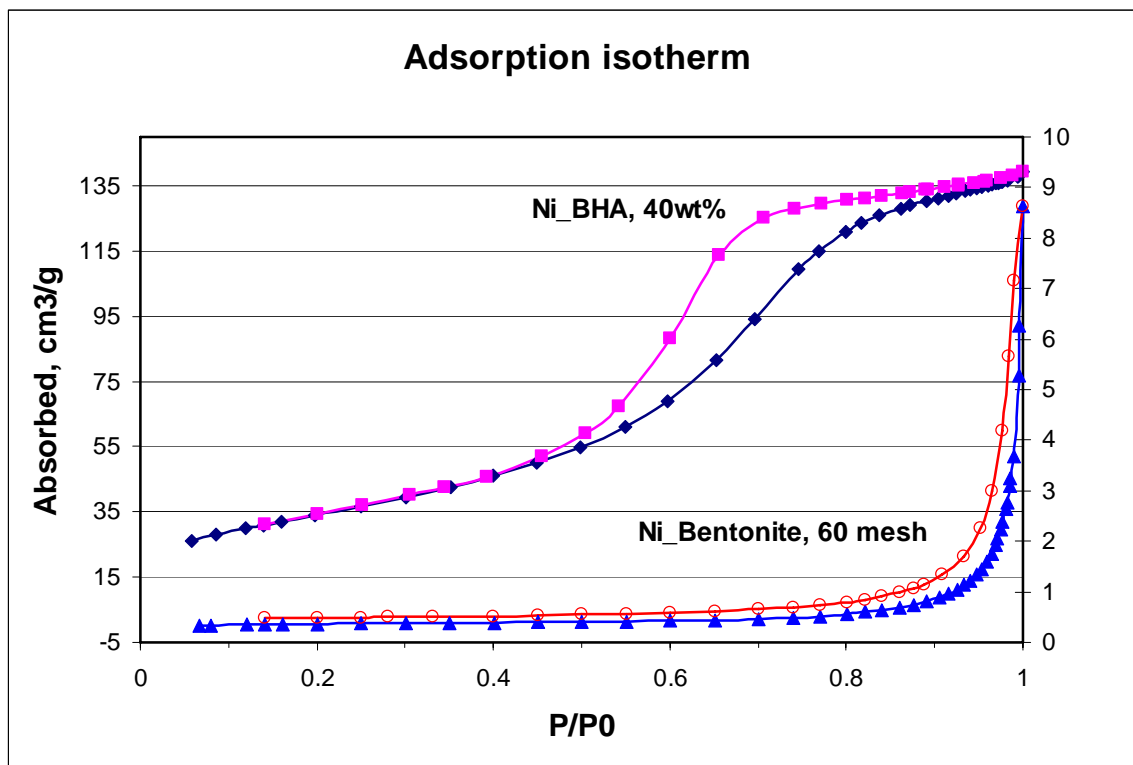


Figure 35. N₂ adsorption isotherm for Ni-BHA and Ni-Bentonite.

Fig. 36 shows the results of BJH pore structure analysis. It is found that the pore diameter of Ni-BHA nanocomposite sample is close to 10 nm. With this characteristic pore diameter, Ni particles in the BHA ceramic matrix are easily accessible to the reactant gases and hence results in fast redox kinetics as will be shown below. The pore structure of Ni-Bentonite can not be analyzed by the instrument because Ni-Bentonite has much larger primary particles (Fig. 32) so

that the overall pore volume is extremely low. Ni particles in Ni-Bentonite are less accessible to reactants and hence diffusion resistance is expected within Ni-Bentonite oxygen carriers.

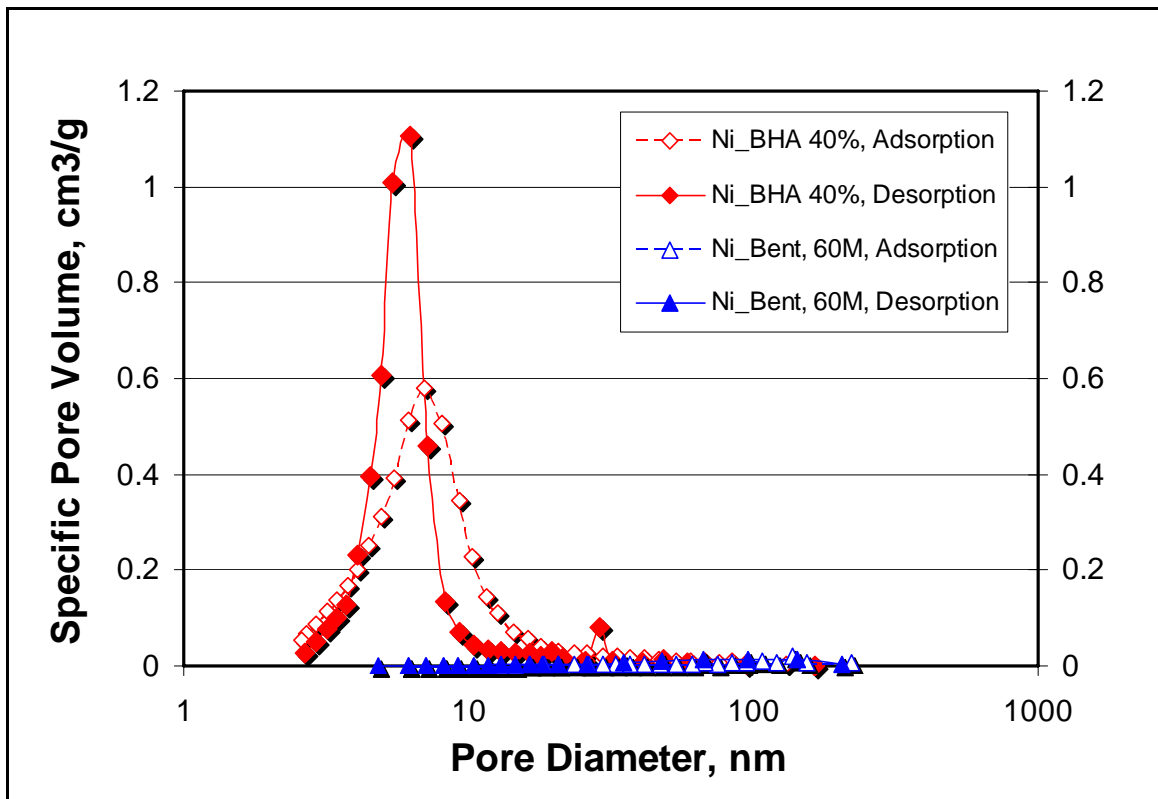


Figure 36. BJH pore structure for Ni_BHA and Ni_Bentonite.

Table 3 summarizes the surface area measurement of Ni-BHA nanocomposite samples and Ni-Bentonite samples. The second column is the result on the oxidized samples and the third column is the result on the reduced samples. It is found that Ni-BHA samples have much larger surface areas, typically two orders of magnitude larger than Ni-Bentonite samples. It is interesting to note that the surface areas of oxidized samples are lower than the reduced samples

(with the exception of the 15wt% Ni-BHA). This is most likely due to clogging of some of the BHA pores by the swelled metal particles during oxidation. The clogging effect is expected to be more significant with higher metal loading as shown in Table 3 from 27wt% Ni-BHA to 37 wt% Ni-BHA, the difference of the surface areas between oxidized and reduced samples are getting bigger. On the 15wt% Ni-BHA, since the metal weight loading is low, the clogging of BHA pores is much less likely to occur. Instead, one observes the surface area of oxidized sample slightly larger than reduced samples, which is mainly due to the increase of metal oxide surface area from its metal counterpart. For Ni-Bentonite samples, the metal weight loading is much higher (60wt %), therefore, one always observes higher surface area of reduced samples than oxidized samples.

Table 3. BET surface area of Ni-Bentonite samples and Ni-BHA samples.

<i>Sample</i>	<i>S.A, m²/g, OX</i>	<i>S.A, m²/g, RE</i>	<i>Δ SA</i>
Ni-Bent, 20 mesh, 60wt%	0.83	1.16	28%
Ni-Bent, 30 mesh, 60wt%	0.68	1.07	36%
Ni-Bent, 60 mesh, 60wt%	0.91	1.27	28%
Ni-Bent, 200 mesh, 60wt%	1.35	1.71	21%
Ni-BHA, 15wt%	187.1	172.2	(- 8.7%)
Ni-BHA, 27wt%	105.3	120.4	13%
Ni-BHA, 32wt%	97.6	123.3	21%
Ni-BHA, 37wt%	124.6	211.6	<u>41%</u>

5.2.4 Reactive test

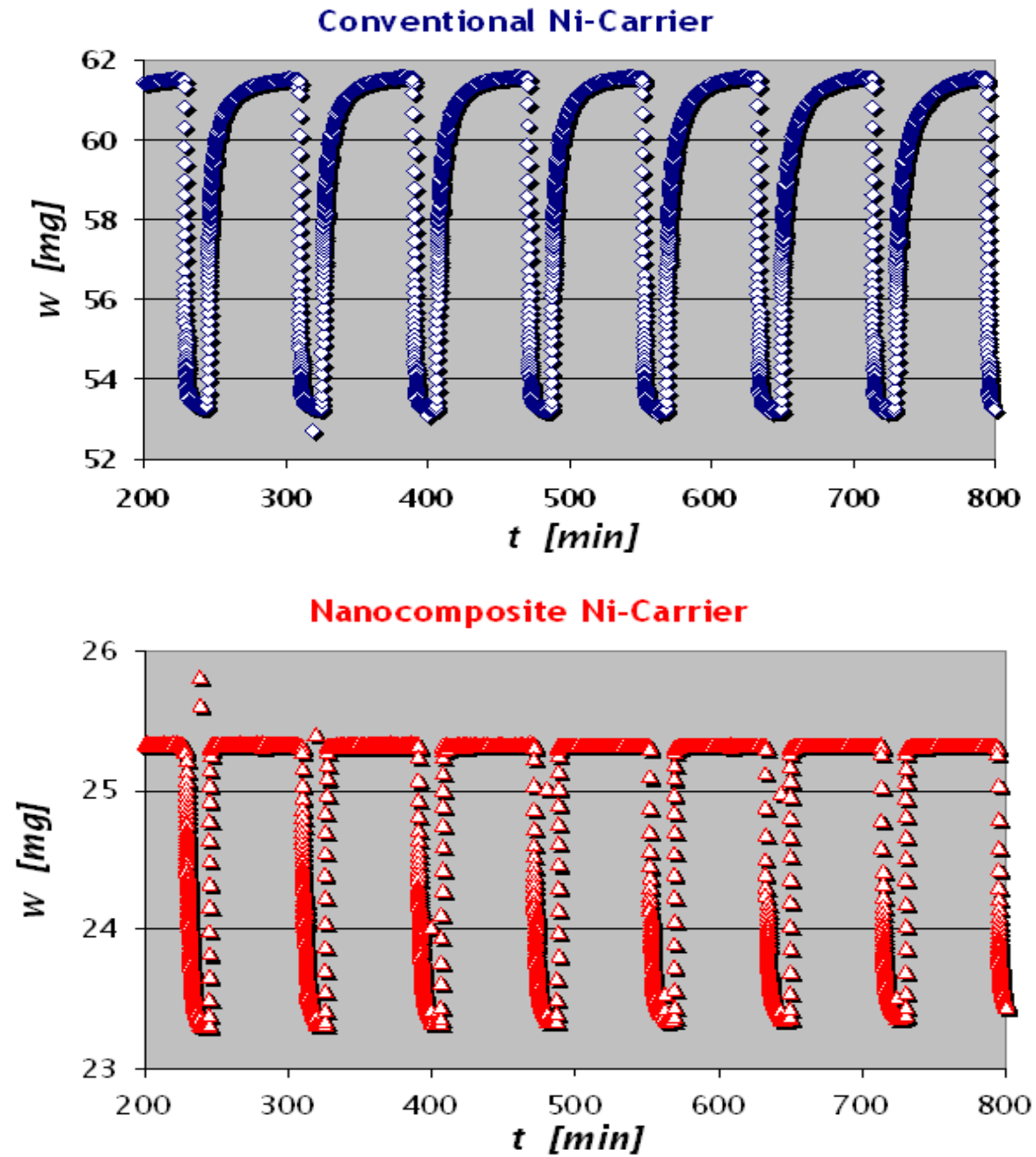


Figure 37. Results from cyclic-TGA for a ‘conventional’ 60wt% Ni-bentonite sample (top) and a nanocomposite 15wt% Ni-BHA nanocomposite sample (bottom). Sample weight is shown versus time.

The nanocomposite Ni-BHA samples were evaluated in direct comparison to the ‘conventional’ bentonite-based Ni samples as described above. Fig. 37 shows two representative TGA traces for both types of samples at an (isothermal) temperature of 800°C. Both samples show very stable and reproducible oxidation and reduction, as indicated by the cyclic weight changes. The weight difference between the reduced and oxidized states of the samples reflects in both cases a complete oxidation and reduction of the Ni, i.e. the Ni content of the conventional and the nanocomposite oxygen carriers is being utilized 100%.

However, strong differences in the redox kinetics are apparent from the distinctly different shapes of the cyclic curves in Fig. 37. These differences become more apparent in a direct superposition of two single redox segments from the above curves (Fig. 38). Since sample weights and Ni content are different between the two samples, the degree of conversion of the conventional Ni-Bentonite carrier (60wt% Ni, triangles) and a nanocomposite Ni-BHA sample (15 wt% Ni, circles) is shown versus time. The conversion X_B is defined as:

$$X_B = \frac{w - w_{re}}{w_{ox} - w_{re}} \quad (9)$$

where:

w : the instant sample weight, mg;

w_{re} : the reduced sample weight, mg;

w_{ox} : the oxidized sample weight, mg;

According to this definition, A conversion of ‘one’ corresponds to the fully oxidized sample (NiO, w_{ox}) and a conversion of ‘zero’ to the fully reduced state (i.e. metallic Ni, w_{re}).

In the respective experiment, the feed gas is switched to the reducing synthesis gas at \approx 713 min, and a fast reduction of the oxygen carriers ensues. Complete reduction is attained within less than 10 mins. for both samples. After a brief nitrogen purge, the feed is switched to

air at $t \approx 730$ min. The samples are now re-oxidized as apparent in the increasing degree of conversion. However, while the reduction of the samples followed very similar time traces, the oxidation kinetics are drastically different: The complete reoxidation of the Ni-Bentonite sample takes almost the entire 60-minute duration of the oxidation half-cycle (only the first 40 min are shown in the graph), while the re-oxidation of the nanocomposite is virtually instantaneous (< 1 min). Clearly, the nanostructure of the oxygen carrier results in a dramatic acceleration of the re-oxidation kinetics.

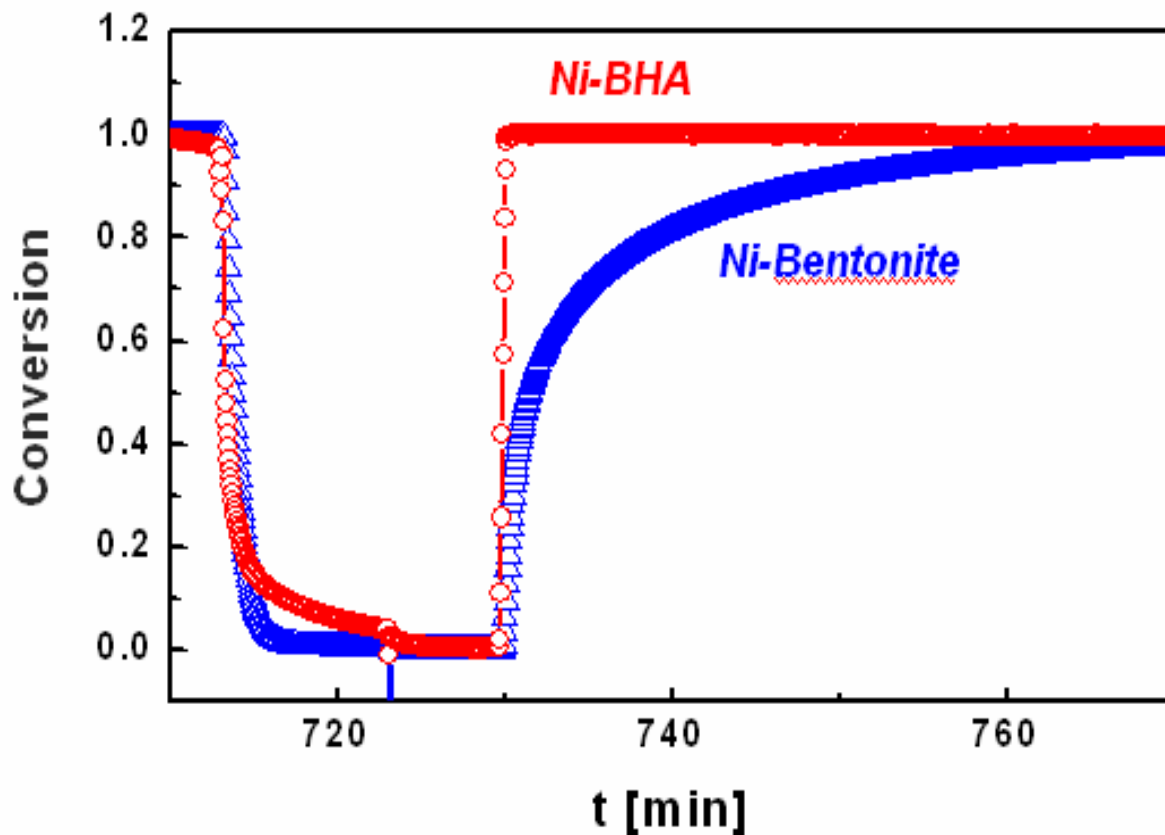


Figure 38. Overlay of a single redox cycle from TGA experiments at 800°C for a nanocomposite carrier ('Ni-BHA') and a 'conventional' carrier ('Ni-Bentonite').

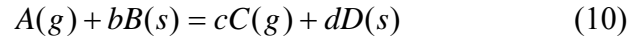
The reason for this strong acceleration of the oxidation kinetics is easily understood: during re-oxidation, a dense oxide layer grows from the surface towards the core of the metal particles. This results in increasing diffusion limitations with increasing degree of conversion due to slow oxygen transport via solid state diffusion through the product layer. By ‘nanoscaling’ the metal particles, the thickness of this oxide layer is reduced to only a few nm (the radius of the particles) and thus diffusion limitations in the oxidation kinetics are completely eliminated.

Similarly, the absence of a strong difference in the reduction kinetics of the two different samples can be explained by the fact that the reduction of the oxidized samples results in highly porous, open metallic layers. Therefore, the size of the primary metal particles does not have a significant impact on the reduction kinetics of the oxygen carriers.

The experimental investigations were further extended over a range of temperatures from 700°C to 900°C, i.e. the typical temperature range for chemical looping combustion processes, as well as onto several different Ni weight loadings of the nanocomposites in order to investigate the influence of temperature and Ni loading on stability and kinetics of the nanocomposite samples. The data obtained from these and the above described TGA experiments was evaluated quantitatively based on a shrinking core model [59]. This analysis allows determination of the rate controlling step during reduction as well as oxidation, as well as quantification of the characteristic time for both steps. (‘Characteristic time’ hereby denotes the time necessary for complete conversion (reduction or oxidation) of a sample based on the rate controlling step.) Details of the procedure will be described below.

5.2.5 Shrinking core model

Considering the oxidation / reduction of a spherical metal / metal oxide particle, both reactions can be written into this form:



As the reaction proceeds, a product layer forms peripherally while the original metal or metal oxide core shrinks. To simplify the model, we assume the reaction takes place isothermally. A schematic of the isothermal shrinking model is illustrated in Fig. 39. The major steps involved in shrinking core model are:

The reactant gas diffuses through the thin external gas film from bulk phase to the solid surface;

The reactant gas diffuses in the product layer to reach the unreacted core;

Reaction takes place on the sharp interface between the metal and metal oxide.

Product gas leaves the interface of Me/MeO and diffuses through the product layer to the solid surface;

Product gas diffuses through the external gas film from the solid surface to bulk phase.

For detailed derivation of isothermal shrinking core model, readers are referred to Appendix D [59]. To summarize, for the shrinking model as shown in Fig. 39, the relation of conversion (X_B) to reaction time (t) is:

$$t = \frac{\rho_{Bm} R}{bc_{Ag}} \left\{ \frac{X_B}{3k_{Ag}} + \frac{R}{6D_e} [1 - 3(1 - X_B)^{2/3} + 2(1 - X_B)] + \frac{1}{k_{As}} [1 - (1 - X_B)^{1/3}] \right\} \quad (11)$$

Where:

ρ_{Bm} : molar density of solid B (Me during oxidation and MeO during reduction, mole/m³);

R: initial particle radius, m;

b : stoichiometric factor in equation (10) ;

c_{Ag} : reactant gas concentration in bulk phase, mol/m³;

k_{Ag} : external mass transfer coefficient, m/s;

D_e : internal diffusion coefficient, m²/s ;

k_{As} : surface reaction rate constant, m/s ;

Eq. (11) can be written as:

$$t = t [t \text{ (external mass transfer control)} + t \text{ (internal diffusion control)} + t \text{ (surface reaction control)}] \quad (12)$$

Where, external mass transfer control term stays for the first term in eq. (11), internal diffusion control stays for the second and reaction control for the third. Particularly, if one of these three controlling steps is dominant, for example, the process is controlled by internal diffusion, where D_e is very small compared to either k_{Ag} or k_{As} , then, the equation can be simplified to only one term

$$t = \frac{\rho_{Bm} R}{bc_{Ag}} \frac{R}{6D_e} [1 - 3(1 - X_B)^{\frac{2}{3}} + 2(1 - X_B)] \quad (13)$$

Similarly, if the process is controlled by external mass transfer:

$$t = \frac{\rho_{Bm} R}{bc_{Ag}} \frac{X_B}{3k_{Ag}} \quad (14)$$

and controlled by surface reaction:

$$t = \frac{\rho_{Bm} R}{bc_{Ag}} \frac{1}{k_{As}} [1 - (1 - X_B)^{\frac{1}{3}}] \quad (15)$$

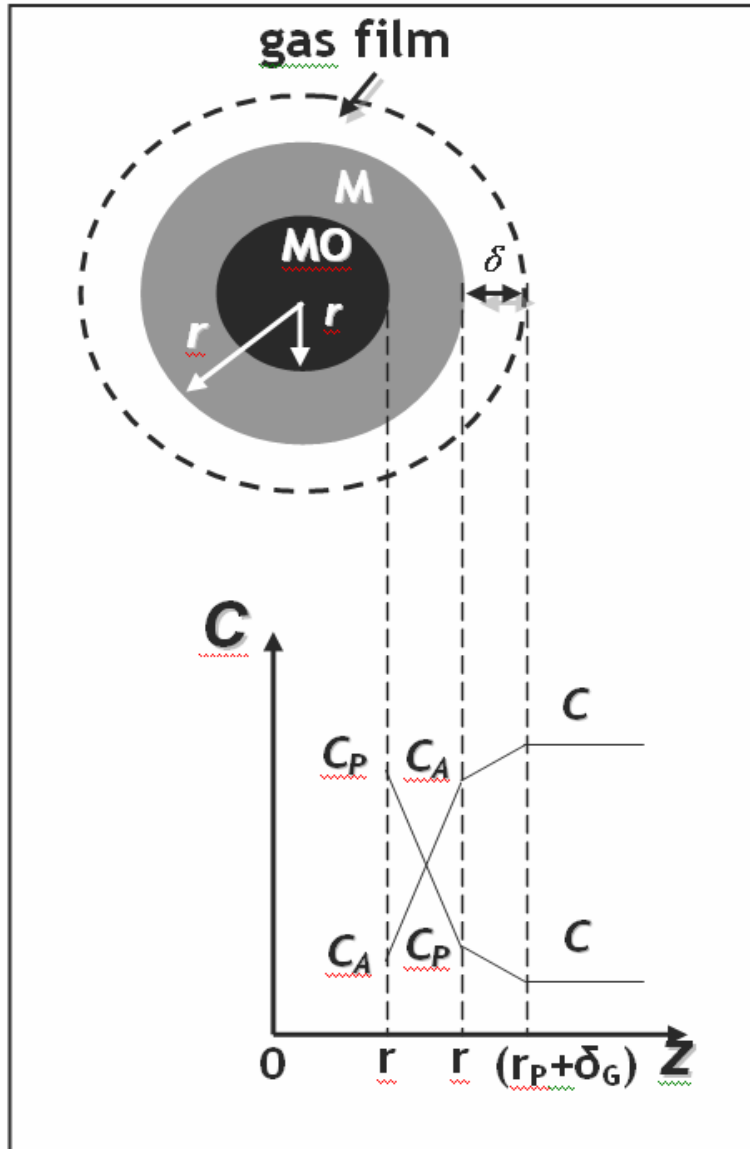


Figure 39. Schematic of shrinking core model.

In table 4, we summarize these three cases in terms of characteristic time τ , which denotes the time necessary for complete conversion (reduction or oxidation) of a sample based on the rate controlling step.

Table 4. Rate limiting cases for shrinking core model.

Controlling steps	t/τ	τ
External mass transfer (MT)	X_B	$\frac{\rho_{Em}R}{3k_{Ag}bc_{Ag}}$
Internal diffusion (D)	$[1 - 3(1 - X_B)^{\frac{2}{3}} + 2(1 - X_B)]$	$\frac{\rho_{Em}R^2}{6bc_{Ag}D_e}$
Surface reaction (R)	$[1 - (1 - X_B)^{\frac{1}{3}}]$	$\frac{\rho_{Em}R}{k_{As}bc_{Ag}}$

We fit our experimental data to these three controlling mechanisms in Table 4. The fitting results tell us which step is the rate limiting step and also give the characteristic times. A typical fitting example is shown in Fig. 40. The circle points are experimental results from TGA. The three lines are fitted curves based on the controlling mechanisms summarized in table 4: solid line for reaction control case, dash line for external mass transfer control case and dot line for internal diffusion control case. It is found that the experimental data fits very well with the solid line (as also indicated by the correlation coefficient R^2), which means the reduction process is controlled by the surface reaction, both the internal diffusion and external mass transfer resistance are negligible. The characteristic time for the reaction control fitted curve is 2.17 min, that is to say, based on the surface reaction control mechanism, the reduction process will finish in 2.17 mins.

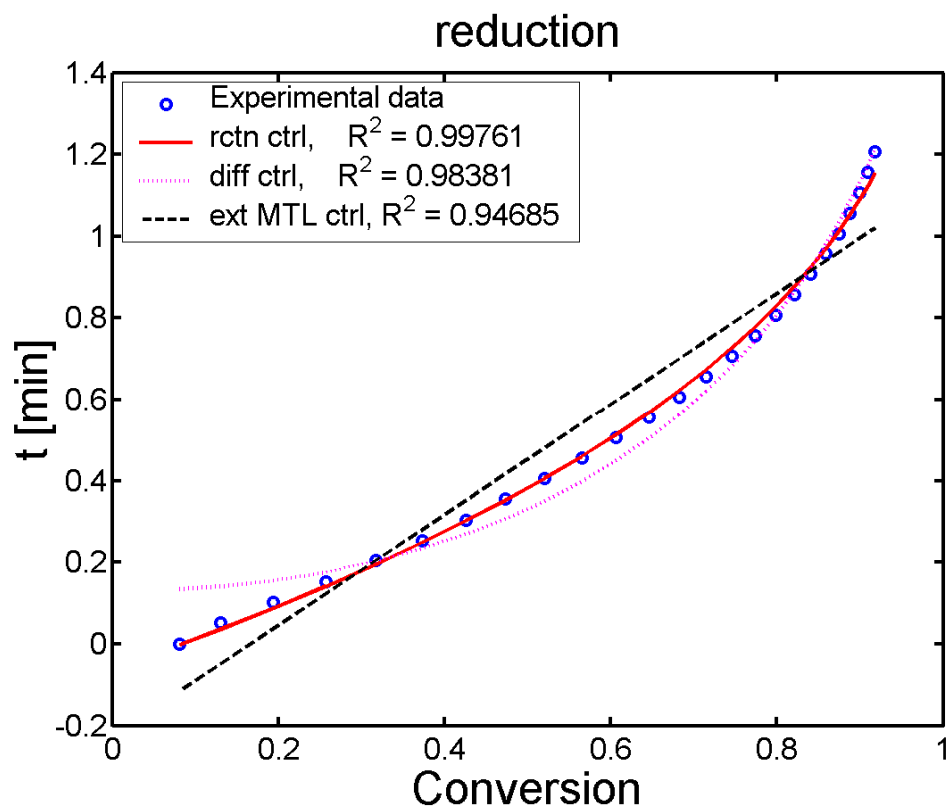


Figure 40. A typical fitting result for the experimental data (circle points) with three fitted lines based on different controlling mechanisms.

Table 5 shows a summary of the main results of this analysis. ‘Control’ refers to the rate-controlling mechanism (‘D’ = diffusion control, ‘MT’ = external mass transfer control, and ‘R’ = reaction control), while τ is the characteristic time constant for the respective rate controlling step obtained from the experimental data.

As expected, the oxidation of the Ni-Bentonite samples is diffusion controlled with a characteristic time of $\tau \sim 47$ min, while the reduction is relatively fast ($\tau \sim 3$ min) and reaction controlled.

Table 5. Summary of comparative evaluation of a ‘conventional’ Ni-bentonite carrier and nanocomposite Ni-BHA carriers with different weight loadings.

Carrier	Ni (wt%)	T (°C)	reaction	control	τ (min)
<i>Ni-Bent</i>	60	800	<i>Oxid.</i>	<i>D</i>	47
Ni-BHA	15	800	Oxid.	MT	0.34
Ni-BHA	26	800	Oxid.	MT	0.50
Ni-BHA	37	700	Oxid.	MT	0.44
Ni-BHA	37	800	Oxid.	MT	0.66
Ni-BHA	37	900	Oxid.	MT	0.77
<i>Ni-Bent</i>	60	800	<i>Red.</i>	<i>R</i>	3.05
Ni-BHA	15	800	Red.	D	2.87
Ni-BHA	26	800	Red.	D	4.97
Ni-BHA	37	700	Red.	D	3.01
Ni-BHA	37	800	Red.	D	1.98
Ni-BHA	37	900	Red.	D	2.17

In contrast to that, oxidation of all nanocomposite samples is drastically accelerated by about two orders of magnitude in comparison to the conventional samples ($\tau < 1$ min. for all samples), resulting in external mass transfer as rate limiting step. This result has two significant implications for the design of a chemical looping process: the drastic acceleration of the oxidation allows a strong reduction of the residence time of the oxygen carrier in the oxidizer and hence a strong reduction in the size of this reactor, which currently has to be sized much larger than the reducer due to the slow kinetics of conventional oxygen carriers. Additionally, the fact that due to the strongly accelerated kinetics the oxidation of the carrier becomes external mass transfer limited facilitates reactor design significantly, since external mass transfer is easy to predict and calculate, and makes the kinetics independent on possible batch-to-batch variations in the carrier production.

In contrast to the MT limited oxidation kinetics, the analysis shows that the reduction of the nanocomposites is diffusion-limited, albeit with a time constant which is comparable to that of the reaction-controlled process for the bentonite sample. As noted above, the reduction of a NiO particle results in highly porous, metallic product layer, and hence no diffusion limitation is to be expected for this process. However, we found the nanocomposite samples to be highly hygroscopic, absorbing significant amounts of moisture during storage at ambient conditions, most likely due to water condensation in the mesoporous network of the sample. We therefore tentatively attribute the diffusion limitation during reduction of the nanocomposites to the comparatively slow diffusion of the reaction product H₂O from the active site (i.e. the Ni/NiO nanoparticle) out of the mesoporous nanocomposite structure.

In agreement with this identification of mass transfer and diffusion as rate limiting steps for the oxidation and reduction of the nanocomposites, the respective kinetics do not show a significant temperature dependence over the investigated temperature range.

Finally, the Ni weight loading of the nanocomposite sample was varied by changing the amount of Ni salt in the aqueous phase of the reverse microemulsion. We verified via TEM (Fig. 32) and XRD (Fig. 34) analysis that this only changes the number density of Ni nanoparticles in the nanocomposites without affecting the Ni nanoparticle size or the ceramic matrix in any way. These nanocomposites thus allow changing of the Ni weight loading while maintaining complete control over the nanostructure of the Ni-BHA samples. However, we found that incorporation of Ni via the synthesis as described above is limited to ~37wt% Ni: for higher corresponding concentrations of the Ni salt in the reverse microemulsion, the synthesis yield becomes incomplete with regard to Ni incorporation. This limitation can be traced back to an ‘exhaustion’ of capacity of the ceramic ‘nanosponge’ matrix: The described synthesis yields metal

nanoparticles embedded in the pore ‘cages’ of ceramic nanosponges. On one hand, this achieves a highly effective capturing and stabilization of the particles at reaction conditions. On the other hand, however, this also imposes an upper limit for the capacity of these nanocomposites, since the capacity of the porous network is exhausted once (virtually) each pore is occupied by one metal particle. We are currently working on tailoring the ceramic structure to obtain more open materials with correspondingly higher capacity for metal nanoparticle incorporation.

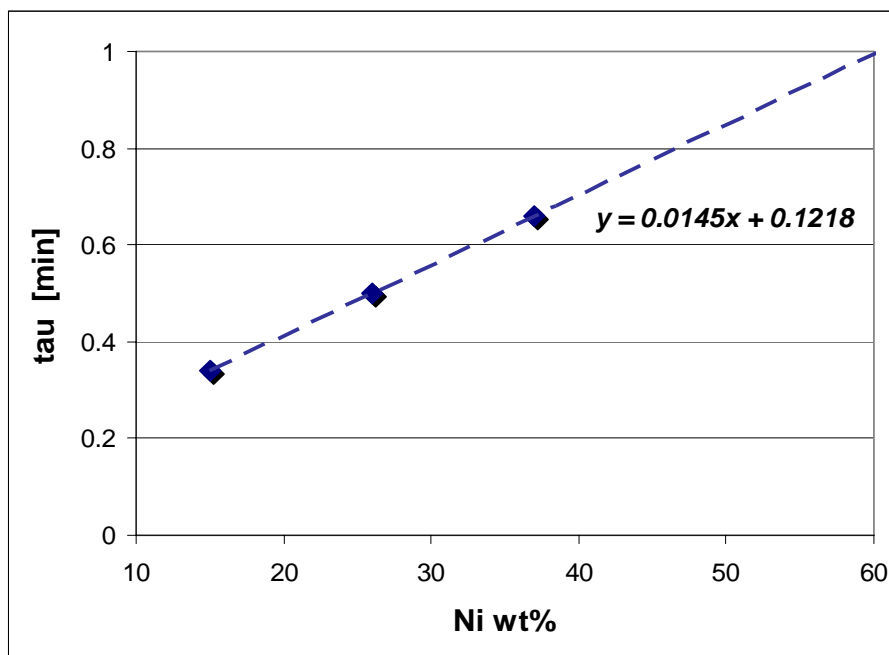


Figure 41. τ as a function of Ni weight loading during the oxidation of Ni-BHA samples at 800°C.

As shown in table 5, the characteristic times for complete oxidation of the nanocomposites increase with Ni loading. We find a near perfect fit to a linear equation: τ [min] = 0.0145 x + 0.1218 (where ‘x’ denotes the Ni loading in wt%, see Fig. 41). This allows us to

extrapolate our results to the (currently unattainable) weight loading of 60wt% Ni, and thus have a direct comparison with the 60wt% Ni-Bentonite samples. We obtain a (theoretical) characteristic time of ~ 1 min. for the oxidation of a 60wt% nanocomposite, indicating that the dramatic acceleration of the oxidation kinetics is in fact not simply the trivial result of the lower weight loading of these samples but truly results from ‘nanoscaling’ the metal particles in the oxygen carriers.

In contrast to the oxidation kinetics, the characteristic time for reduction of the samples is completely unaffected by the weight loading. In view of the identification of (product) diffusion as rate limiting step, this seems very surprising at first. An increasing amount of metal oxide requires a correspondingly larger amount of reaction product to diffuse out of the nanocomposite, which should hence lead to a significant slow-down of the overall reduction. The absence of this effect is again strong evidence for the exceptionally open, highly accessible structure of the nanocomposite carriers: In the irregular porous network of these nanosponges, a specific, individual optimal transport path exists for each metal nanoparticle. Increasing the metal loading by increasing the number density inside the structure hence simply results in more of these ‘optimal transport pathways’ being utilized, rather than a competition for the existing diffusion cross-sections and a corresponding slow-down as would be observed in conventional materials.

5.2.6 High temperature stability

During CLC, the oxygen carriers are subjected to very high temperatures (700 – 1000°C) and periodic reduction and oxidation atmospheres. These harsh conditions demand strict high temperature stability of the material. Fig. 42 compares the stability of Ni-BHA (37wt %) and Ni-

Bentonite (60wt%, 20 mesh) at high temperatures for several redox cycles during reactive evaluations in a TGA. One finds that at 700 °C, the Ni-Bentonite sample needs a long induction period (up to 3 redox cycles) to get complete reduction and re-oxidation. After the induction period, there is no apparent deactivation of the oxygen carrier, the redox cycles are stable. At 800 °C, the Ni-Bentonite sample already sees deactivation as one observes decreasing upper weight level when the oxygen carrier is being re-oxidized which indicates that it can not return to the previous oxidized state (weight). The deactivation is more apparent at 900°C: within 10 redox cycles, the oxygen carrier loses ~60% of its oxygen uptake capacity. Therefore, the conventional prepared (from physical mixing) Ni-Bentonite samples are not stable at high temperature applications. For Ni-BHA samples, even at 900°C, we do not see any indication of deactivation.

It is also found that for Ni-Bentonite samples, while they can not be fully oxidized anymore, they can still resume completely to their previous reduced state as one observes an unchanged bottom weight level. Therefore, the deactivation affects only the oxidation cycle. At high temperatures, metal particle sintering is the main reason for deactivation. As particles sinter together and form larger ones, the diffusion resistance for oxygen is expected to be larger. As a result, the oxidation kinetics will be significantly slowed down. For Ni-BHA, however, the stable redox behavior indicates that the sintering problem is overcome. The reason for the high temperature stability of Ni-BHA samples can be understood in their structure: as shown in Fig. 32 by TEM, the nanosized metal particles are being “embedded” in the BHA support matrix rather than being “supported”. The metal particles fill the pore cages of the ceramic matrix and thereby the surface mobility of these nanosized metal particles as well as sintering at high temperature is significantly inhibited.

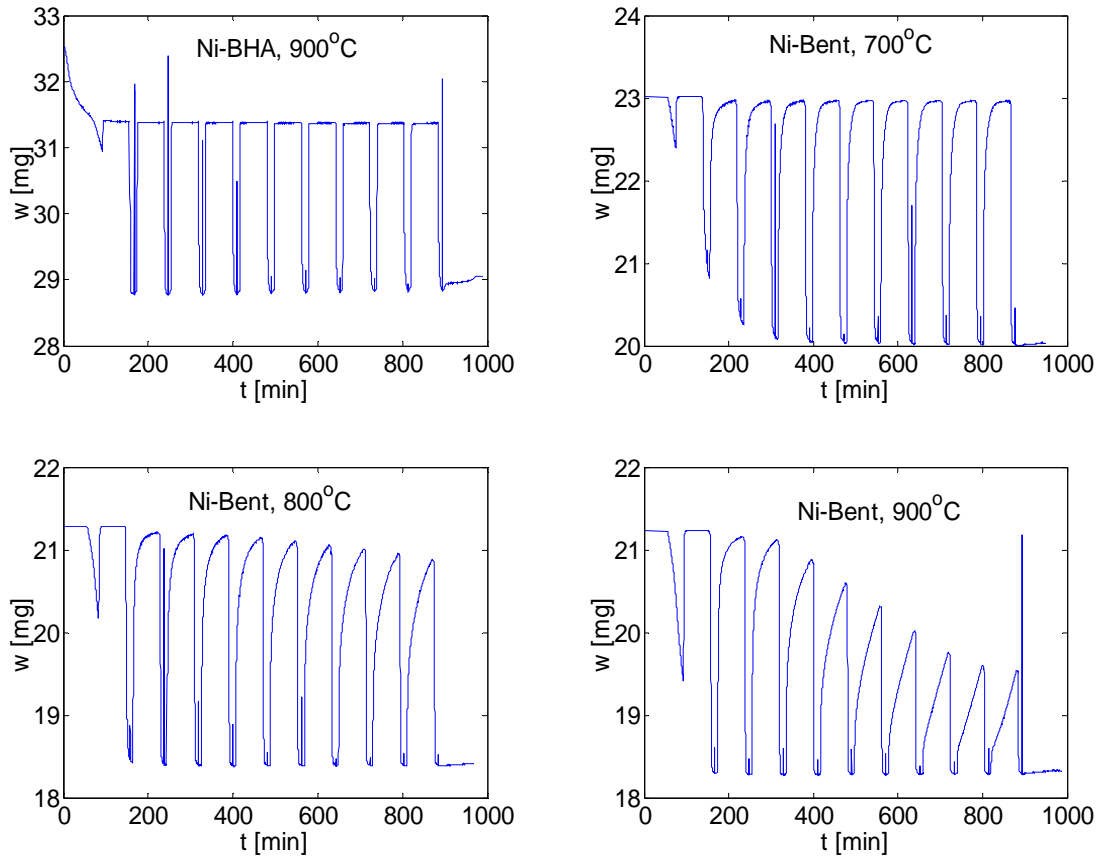


Figure 42. TGA reactive evaluations for Ni-BHA with 37wt% NiO loading at 900°C and Ni-Bentonite sample with 20 mesh particle size and 60wt% NiO loading at 700, 800 and 900°C respectively.

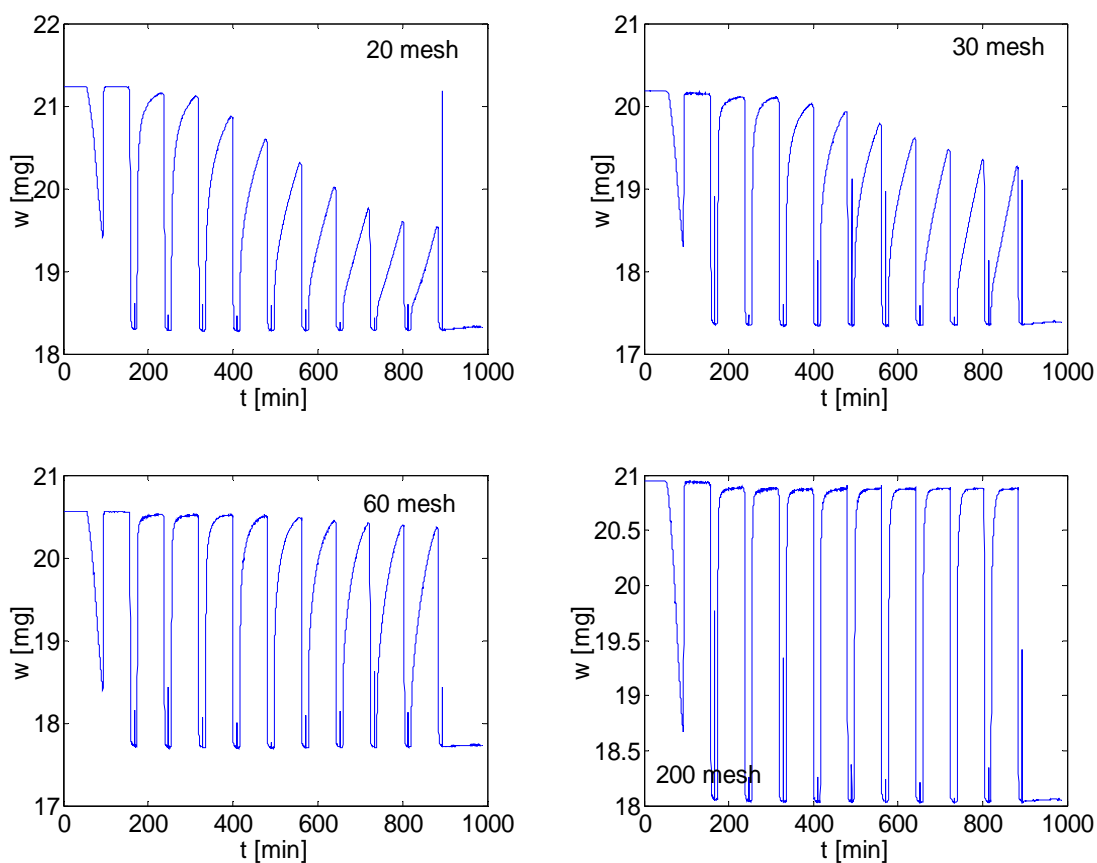


Figure 43. TGA reactive evaluations for 20, 30, 60 and 200 mesh Ni-Bentonite carriers with 60wt% NiO loading at 900°C.

In addition to the findings above, we also find that the deactivation on Ni-Bentonite oxygen carriers differs with different mesh size. Shown in Fig. 43 are the results of cyclic TGA reactive evaluation for Ni-Bentonite samples with different mesh (20 – 200mesh) at 900°C. One finds that the deactivation is most significant on 20 mesh (bigger) sample, and decreases with decreasing mesh size. On the 200 mesh sample, although there is not much deactivation as shown in the graph, we compare the first and last individual cycle and we find that in fact, 200

mesh Ni-Bentonite also deactivates. The characteristic time for the first cycle is ~ 9 mins, while it is ~19 min for the last cycle. While on all of our Ni-BHA carriers, we do not find any indication of deactivation.

5.2.7 Results on other metals

Besides Ni-BHA, we also synthesized Cu-BHA, Fe-BHA and Co-BHA. While the synthesis routes are similar for these samples, the reactivity results differ significantly. We will briefly discuss these results and conclude that Ni-BHA is more suited for the application of CLC than the other samples.

5.2.7.1 Fe-BHA

Fig. 44 shows the reactive test for Fe-BHA with 16wt% weight loading at 800oC. Similar to Ni-BHA, Fe-BHA also shows stable and reproducible redox behavior after the water has been removed. There is a small step between cycle 5 and 6 near 500 min, which is due to instrument noise. Assuming the sample is reduced from Fe_2O_3 to Fe during redox, the metal utilization calculated from the TGA data gives ~34%. Therefore, more likely reduction stops at FeO, which gives the metal utilization ~100%. As a result, for Fe_BHA, we can not use all of the available oxygen in the oxide. The available oxygen per unit weight Fe based oxygen carrier (10.02wt %) is hence less than Ni based carriers (21.42%).

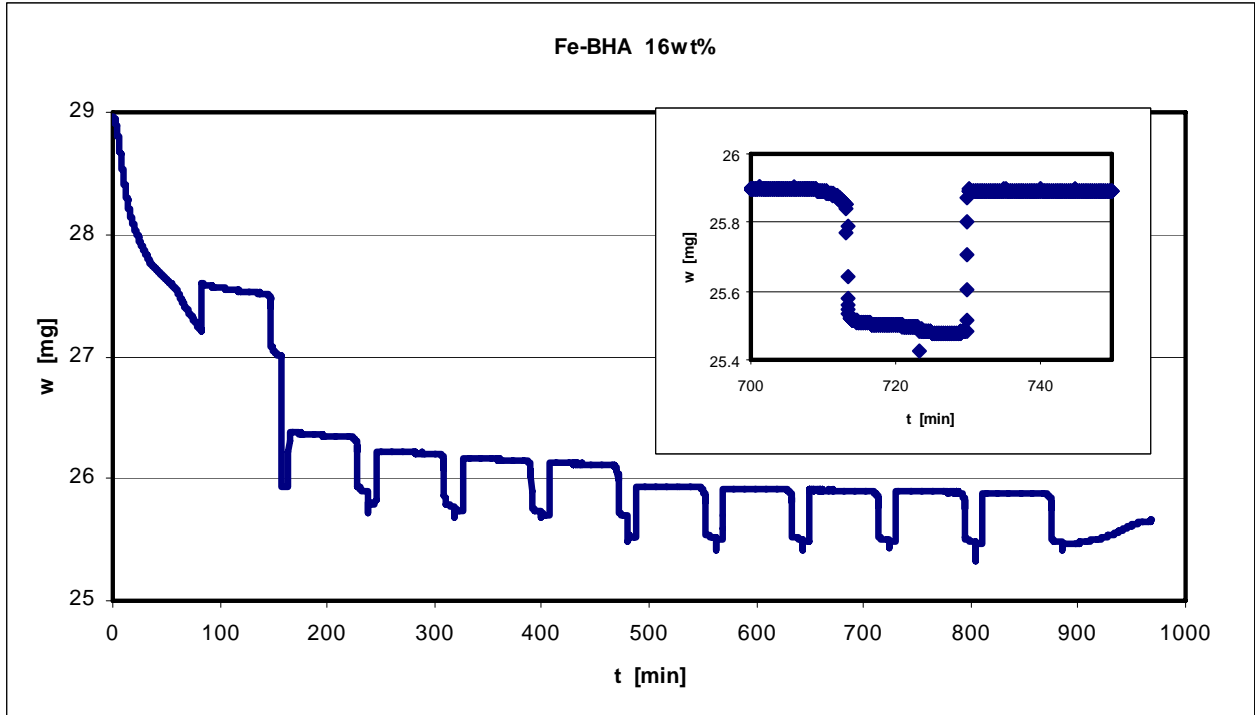


Figure 44. Results from cyclic-TGA for 16wt% Fe-BHA nanocomposite sample. A single redox cycle result is shown in the upper graph.

We also used SCM to analyze the reduction and oxidation kinetics shown in Fig. 44 upper layer. The reduction fit was not very satisfactory due to the quality of available data, while the re-oxidation fit again reveals that the re-oxidation is controlled by external mass transfer with characteristic time $\tau \sim 0.22$ min.

Fig. 45 compares the re-oxidation behavior of Fe-Bentonite and Fe-BHA. Again, one observes significant accelerated re-oxidation kinetics: The complete reoxidation of the Fe-Bentonite sample takes almost 60-minute duration of the oxidation half-cycle, which is due to the slow diffusion in the product layer; while the re-oxidation of the nanocomposite is virtually instantaneous ($\tau \sim 0.22$ min).

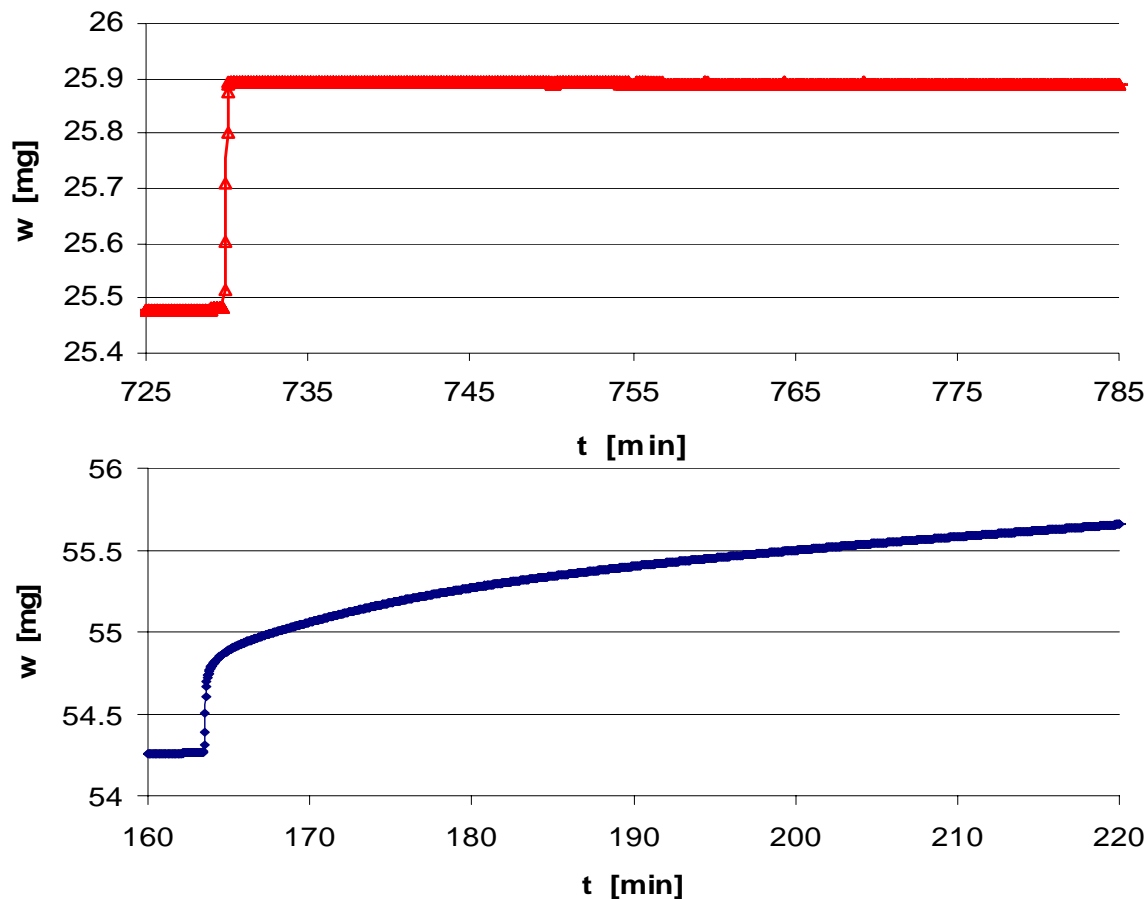


Figure 45. Comparison of re-oxidation kinetics for Fe-BHA (16wt%) and Fe-Bentonite (60wt%) at 800°C.

5.2.7.2 Cu-BHA

We also synthesized Cu-BHA nanocomposite oxygen carriers. XRD, TEM (not shown here) results showed that Cu-BHA has similar structure as Ni-BHA. The metal particles are embedded in the support matrix. When oxidized, the sample turns completely to CuO and when reduced, the sample turns completely to Cu. The redox behavior for a single cycle is shown in Fig. 46

upper graph. Similar to Ni_BHA and Fe_BHA, the redox kinetics of Cu_BHA carriers are also very fast. From Fig. 46, both the reduction and re-oxidation of Cu_BHA take less than 1 min.

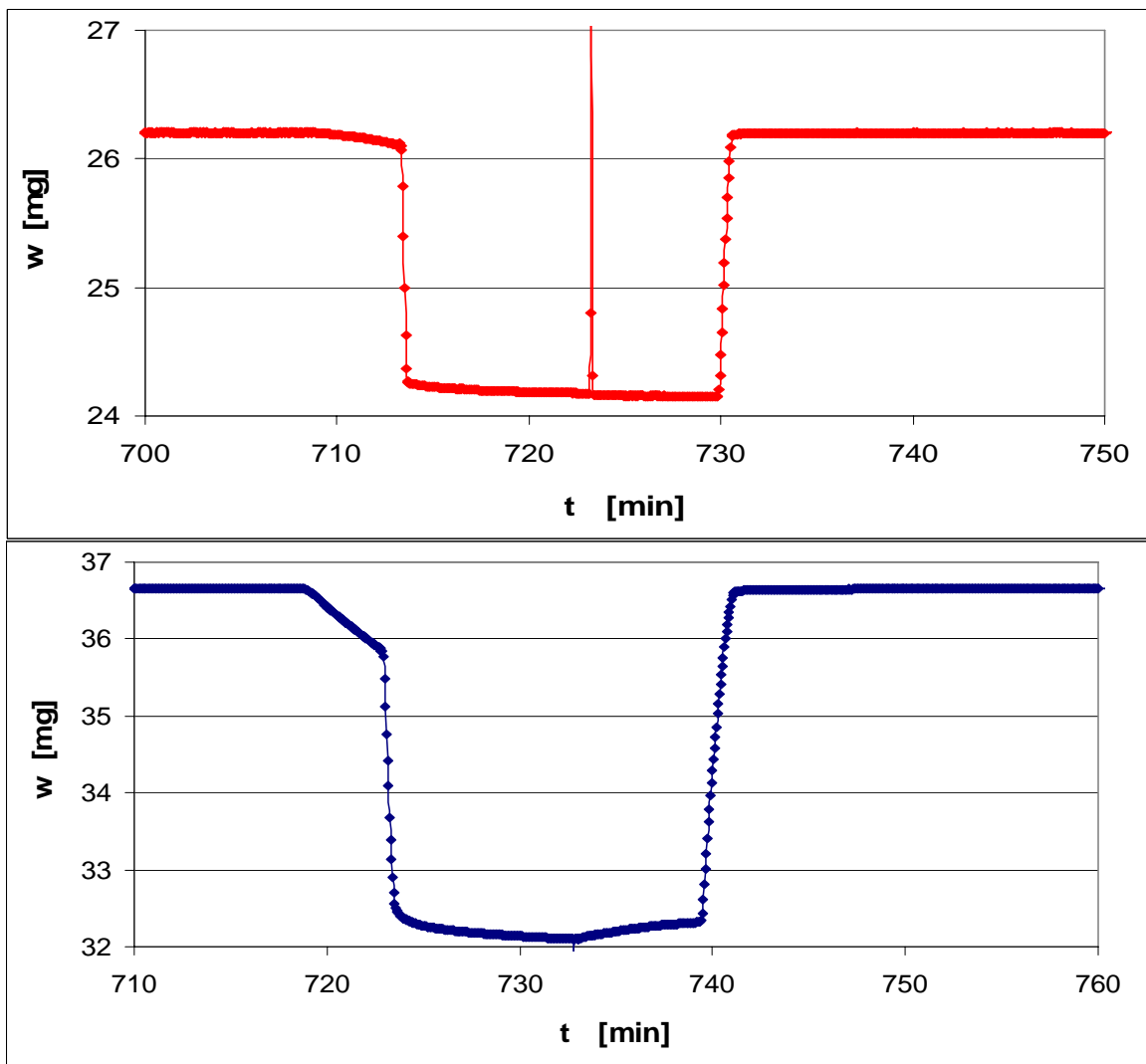


Figure 46. Comparison of a single redox cycle from TGA experiments at 800°C for a nanocomposite carrier Cu-BHA and a conventional Cu-Bentonite.

However, when compared to conventional prepared Cu-Bentonite oxygen carrier, quite surprisingly, we found the re-oxidation of Cu-BHA is only slightly accelerated because the re-oxidation on Cu-Bentonite is already very fast.

Table 6. Summary of comparative evaluation of a ‘conventional’ Cu-Bentonite carrier and nanocomposite Cu-BHA carriers.

Sample	Reaction	T [°C]	Limiting step	τ [min]
Cu-Bent, 60wt%	Ox	800	R	2.9
Cu-BHA, 40wt%	Ox	700	MT	0.60
Cu-BHA, 40wt%	Ox	800	MT	0.62
Cu-BHA, 40wt%	Ox	900	R	1.50
Cu-Bent, 60wt%	Re	800	MT	0.75
Cu-BHA, 40wt%	Re	700	MT	0.28
Cu-BHA, 40wt%	Re	800	MT	0.27
Cu-BHA, 40wt%	Re	900	MT	0.30

In table 6, we show the SCM analysis of Cu based oxygen carriers. One finds that the re-oxidation of Cu-BHA at 800 °C is controlled by external mass transfer and the characteristic time is 0.62 min. The re-oxidation of Cu-Bentonite carriers at 800°C is controlled by surface reaction and the characteristic time is 2.9 min. While the time scale (less than 1 min) and controlling mechanism (MT) on Cu-BHA during re-oxidation are similar to those on Fe-BHA and Ni-BHA, the time scale and controlling mechanism on Cu-Bentonite are significantly different. Typically,

on Fe-BHA or Ni-BHA, the re-oxidation is controlled by the internal diffusion and the characteristic time is very long, close to 1 hour, while on Cu-Bentonite, the re-oxidation is much faster and controlled by surface reaction. Internal diffusion is not the rate limiting step. This interesting observation can be well understood via Fig. 47 [60].

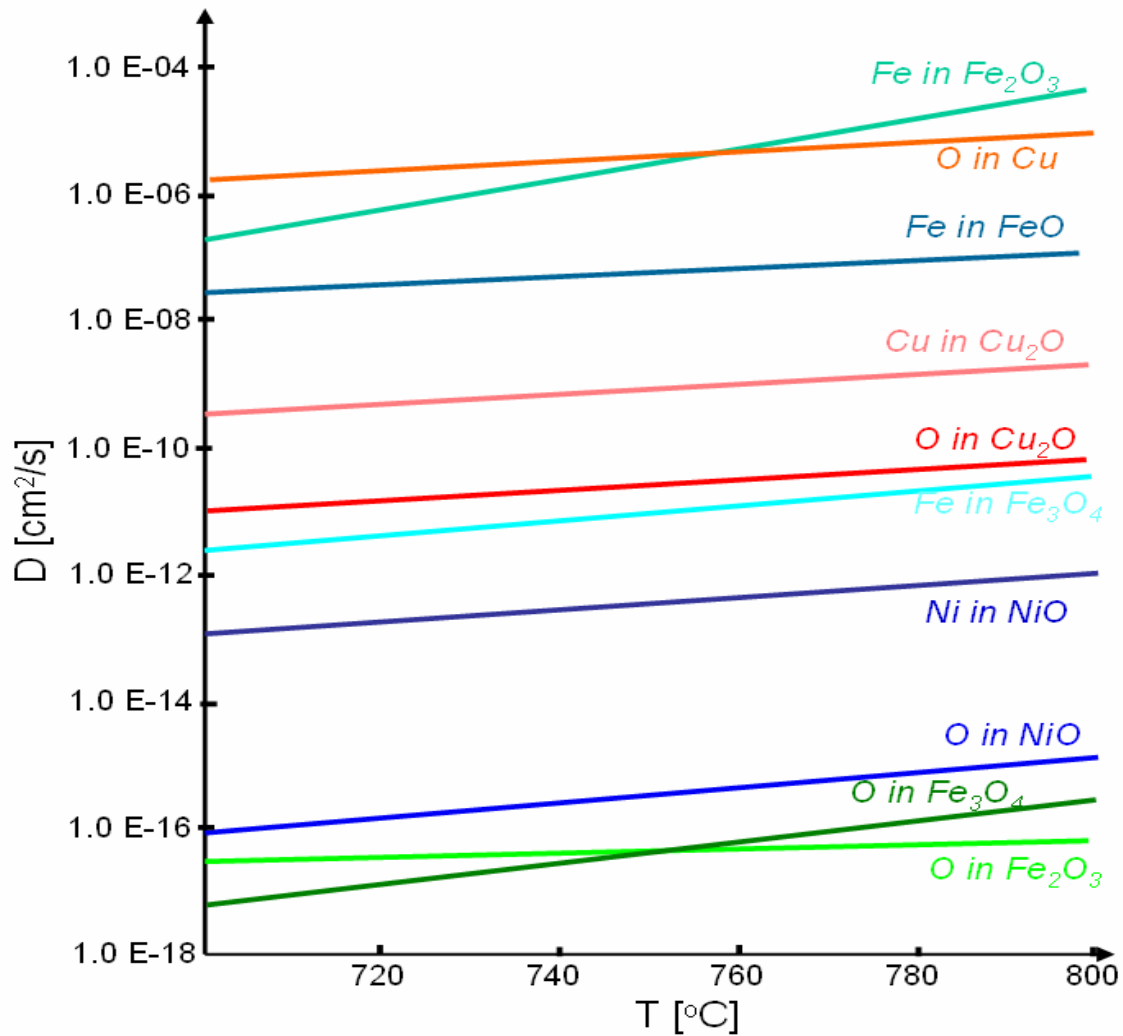


Figure 47. Oxygen diffusivity in different metal oxides at different temperatures (adapted from I. Gallino, Ph.D. thesis, Oregon State, 2003).

Fig. 47 shows the oxygen diffusivity in different metal oxide layers at different temperatures. It is found that the oxygen diffusivity in Cu and Cu₂O are at least five orders of magnitude larger than those in NiO and Fe₂O₃ or Fe₃O₄. Therefore, oxygen diffuses in copper oxide layer drastically faster than in the nickel or iron oxide layer. As a result, while the internal diffusion through the metal oxide layer during re-oxidation is the rate limiting step for Ni-Bentonite and Fe-Bentonite, it is no longer the rate limiting step for Cu-Bentonite.

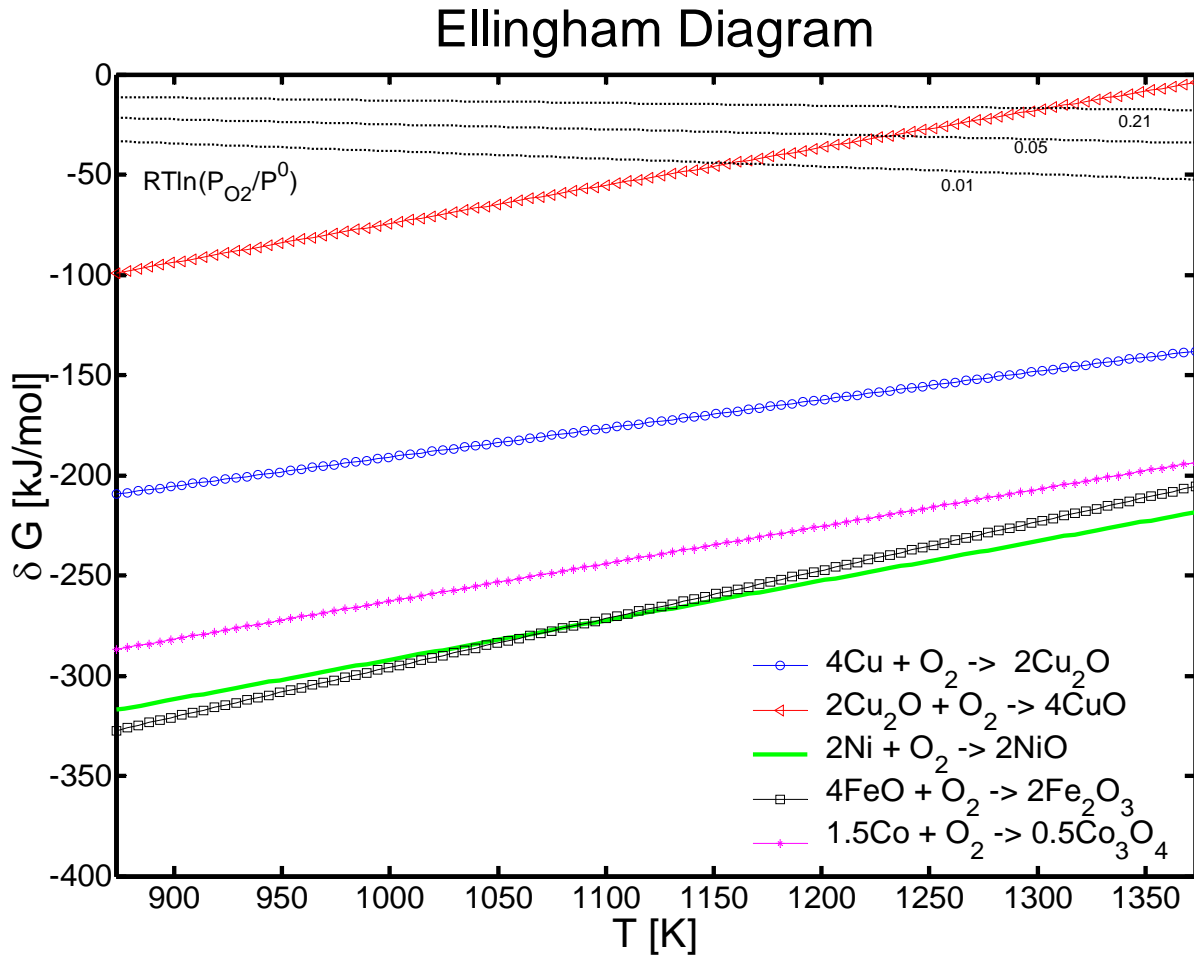


Figure 48. Ellingham diagram for Ni, Fe, Cu and Co oxidation reactions.

It is puzzling to note that in table 6, while the re-oxidation of Cu-BHA at 700 and 800°C is controlled by external mass transfer with characteristic times near 0.6 min, the re-oxidation of Cu-BHA at 900°C is controlled by surface reaction with an even increased characteristic time up to 1.5 min. Since temperature influences reaction rate more significantly than mass transfer rate, one would not expect the reaction to be the rate limiting step at higher temperatures if it is not the rate limiting step at lower temperatures. This observation, however, can be explained through the Ellingham diagram in Fig. 48. In the Ellingham diagram, the oxidation reaction free energy (ΔG) are shown versus temperature for different metals/metal oxides. The relationship of reaction free energy to oxygen partial pressure at reaction equilibrium can be expressed as:

$$\exp\left(\frac{-\Delta G}{RT}\right) = \frac{p^0}{p_{O_2}} \quad (15)$$

Rearrange the above equation gives:

$$\Delta G = RT \ln\left(\frac{p_{O_2}}{p^0}\right) \quad (16)$$

In Fig. 48, we also show three lines of $RT \ln\left(\frac{p_{O_2}}{p^0}\right)$ on the top of the graph. The top most line represents $RT \ln\left(\frac{p_{O_2}}{p^0}\right)$ with oxygen partial pressure at 0.21 to simulate air; the middle line for $p_{O_2} = 0.05$ and the lowest line for $p_{O_2} = 0.01$. These three different oxygen partial pressures are used to simulate the reaction atmosphere in the CLC oxidizer. The intersection of these three lines with the ΔG line means the reaction is at equilibrium at the given oxygen partial pressure and corresponding intersection temperature. Further increase the temperature beyond the intersection temperature will increase the reverse reaction, e.g., the decomposition of the metal oxides.

From Fig. 48, the free energy for Ni, FeO and Co oxidation reactions are all far below the $RT \ln\left(\frac{P_{O_2}}{p^0}\right)$ lines during the temperature range we calculated. The free energy for Fe oxidation is even further below and is not shown in Fig. 48. These results indicate that the oxidation of these metals is stable at this temperature range. No decomposition of the metal oxides will occur. Therefore, Ni, Fe and Co can be applied at high temperatures in CLC.

The intersection of the three $RT \ln\left(\frac{P_{O_2}}{p^0}\right)$ lines with Cu₂O oxidation indicates that CuO is not stable at high temperatures and decomposes to Cu₂O when the temperature goes beyond the equilibrium temperature at corresponding oxygen partial pressures. We also performed CuO-BHA decomposition studies in a TGA. We found that CuO-BHA decomposes (starts losing weight) at around 950°C in air and around 750 °C in N₂. Therefore, the observed reaction control during Cu-BHA re-oxidation at 900°C in table 6 is most likely due to the competing effects of oxidation and decomposition. While at 700°C and 800°C, the decomposition reaction is very unlikely to occur and hence external mass transfer control is observed.

These results demonstrate that Fe, Co and Ni based oxygen carriers can be used at a very broad temperature range while the applications of Cu based oxygen carriers are limited to low-medium temperature ranges.

5.2.7.3 Co-BHA

We synthesized Co-BHA with the target weight loading of 30wt% and 50wt% respectively. However, during 50wt% synthesis, we found we could not incorporate all the metal into the ceramic matrix as we observed magenta color in the upper layer solution during phase separation. The similar phenomenon also appears during Ni and Cu nanocomposite synthesis for

high target loadings. The maximum weight loading we could get is roughly near 40wt% for all of these metals.

The Co-BHA oxygen carriers were then reduced and re-oxidized to determine the actual weight loading and the samples were also taken for XRD studies. The redox results show that we can't completely use the oxygen of the metal oxide: only got ~7.5wt% and ~10.0wt% calculated weight loading were obtained for 30wt% and 50wt% target synthesis respectively. While XRD results indicate that when oxidized, the sample turns to Co_3O_4 , when reduced, the sample turns to Co, we found extremely slow kinetics on Co-BHA samples: after even 1 hour reduction of Co_3O_4 -BHA in 5 – 10% H_2/N_2 at 800°C, we still observed significant diffraction peaks from Co in the XRD pattern, indicating that we can't reduce all of the Co_3O_4 into Co within a meaningful reaction time. Therefore, Co-BHA is not as interesting as the other three nanocomposite oxygen carriers.

5.3 SUMMARY

In this chapter, we synthesized Ni, Fe, Cu and Co novel nanocomposite oxygen carriers for chemical looping combustion and compare them with conventional prepared bentonite samples using a synthetic 'coal gas' (synthesis gas) as model fuel. The nanometer size of the metal particles in these nanocomposites leads to an acceleration of the oxygen uptake of these carriers by about two orders of magnitude for Ni-BHA and Fe-BHA in comparison to the conventional carriers.

Due to the embedding of the metal nanoparticles in a high-temperature stable ceramic matrix, sintering is completely prevented, resulting in exceptionally stable carriers with highly

reproducible oxidation-reduction cycles at reaction conditions. At the same time, the highly open structure of these nanocomposites keeps the metal particles accessible and avoids or minimizes internal mass transfer limitations even at the high-temperature conditions of chemical looping combustion.

Table 7 qualitatively summarizes some major characteristics of nanocomposite oxygen carriers we have synthesized. These results reveal that Ni-BHA is more suitable for the application as CLC oxygen carriers. Compared to Ni-BHA, Fe-BHA has similar redox kinetics, while the oxygen uptake capacity is much lower. Co-BHA has higher oxygen uptake capacity; however, the redox kinetics is significantly slower. Cu-BHA has similar redox kinetics and similar oxygen uptake capacity, but it is limited to low-medium temperature applications only. The conventionally prepared Ni-Bentonites have significantly slower re-oxidation kinetics and is subjected to significant deactivation.

Table 7. Summary of nanocomposite oxygen carriers.

Carrier	Ox / Re	O capacity	Ox. control	τ [min]	Re. control	τ [min]
Ni-BHA	NiO/Ni	21.42wt%	MT	<1	D	2 – 6
Fe-BHA	Fe ₂ O ₃ /FeO	10.01wt%	MT	<1	MT	N/A
Cu-BHA	CuO/Cu	20.11wt%	MT	<1	MT	<1
Co-BHA	Co ₃ O ₄ /Co	26.58wt%	Incomplete	Very slow	Incomplete	Very slow

Overall, we see great potential for these novel nanostructured oxygen carriers for clean energy applications, and we are currently extending the presented approach onto other metal carriers and towards further tailoring of the nanostructure of these materials.

6.0 SUMMARY AND OUTLOOK

6.1 SUMMARY

This presented work consists of two parts. In the first part, we investigated syngas production from methane via CPOM and ATR in a reverse-flow reactor (RFR) while in the second part, we studied nanocomposite oxygen carriers for chemical looping combustion. Both of these processes are of strategic importance for future fuel and energy production. The objectives of these studies are to improve our understanding of these processes and obtain process intensification. We have demonstrated that the process intensification goals can be well achieved via multifunctional reactor concepts. However, for different processes, we have also demonstrated that the ‘multifunctionality’ occur at different levels.

6.1.1 Syngas / hydrogen production in a reverse-flow reactor (RFR)

We reported on a mechanistic study of catalytic partial oxidation of methane over a supported Pt catalyst in which we varied catalyst length and gas flow rate, and correlated conversion and selectivity data with in-situ temperature profile measurements. In this way, we were able to obtain a detailed understanding of the reaction mechanism in a fairly simple and straight-forward experiment. The reaction pathway on the supported Pt catalyst consists of an initial oxidation zone in which predominantly CO and H₂O are formed, followed by a steam reforming zone. The

oxidation reactions lead to a sharp temperature increase near the front edge of the catalyst. As soon as the available oxygen is consumed, the reaction shifts to steam reforming, accompanied by some water gas shift reaction. The endothermic steam reforming reaction results in a steep temperature drop towards the catalyst exit.

Both thermodynamic calculations and reaction mechanism studies reveal that there is a complex interaction between exothermic combustion reaction and endothermic reforming reactions. This interaction limits obtainable syngas yields at autothermal operations. We demonstrated that this limitation can be overcome through heat-integration in a RFR. Significantly improved methane conversion and syngas selectivities are observed. Reactor throughput is also significantly increased. Furthermore, although RFR operates at higher temperatures than steady state (SS) operation, it leads to an intrinsic compensation for catalyst deactivation. In-situ dynamic temperature profiles studies showed that there are decoupled effects of kinetically controlled dynamics in the catalyst and thermally controlled dynamics in the inert zones. Heat is efficiently integrated in the reaction zone. High temperature beyond the adiabatic limits can be obtained. We also demonstrated that this reactor configuration is well suited for ATR. Not only syngas, particularly H_2 , yields are significantly improved, the autothermal range is also significantly increased to a much broader range e.g, to high water additions for maximum production of hydrogen. The product H_2/CO ratios are improved at least four folds over SS operations, which make downstream treatments more flexible.

Overall, we have demonstrated that the use of regenerative heat-integration through dynamic reactor operation yields reactor configurations which are particularly suited for small-scale and decentralized syngas / hydrogen production from methane.

6.1.2 Nanocomposite oxygen carriers for chemical looping combustion (CLC)

Conventionally prepared oxygen carriers for CLC suffer from slow (re-oxidation) kinetics as well as sintering at high temperatures. While nanosized metal particle could minimize the internal diffusion resistance and thereby accelerate the re-oxidation kinetics, nanosized metal particles still suffer from sintering significantly. We have synthesized ‘multifunctional’ nanocomposite oxygen carriers — Me-BHA samples. In these so called nanocomposites, nanosized metal particles are embedded in the high-temperature stable ceramic support (here, BHA) matrix. The nanoscale metal particles retain fast kinetics while sintering problems are significantly prohibited by the ‘holding’ of the support matrix.

Our results reveal that diffusion resistance associated with conventional oxygen carriers (Ni-Bentonite) is minimized and the reaction kinetics is significantly accelerated on the Ni-BHA carriers by at least two orders of magnitude. The Ni-BHA is also very high temperature stable while Ni-Bentonite deactivates significantly, particularly at higher temperatures.

Ni-BHA is also a more suitable oxygen carrier for CLC than other Me-BHA candidates: Fe-BHA has lower oxygen uptake capacity, Co-BHA has extremely slow kinetics and Cu-BHA is limited to low/median temperature applications.

While in the first part, the process intensification is achieved via multifunctional reactor concepts at the reactor level, here, the multifunctionality occurs at the material level.

6.2 OUTLOOK

6.2.1 Mass transfer studies during CPOM

One might expect reactions such as CPOM and ATR at high temperatures to be limited by mass transfer. To study the mass transfer influences, isothermal reactor operation is necessary and variations of flow rates are essential. Unfortunately, the extremely high temperature around 1000°C as well as the extreme temperature gradients of up to 10^6 K/m prevents such studies. Furthermore, our experiments were conducted at autothermal conditions. Increasing flow rate not only increases (external) mass transfer, more significantly, it increases the overall reaction heat as well as heat transfer in the catalyst bed and inert zones as one observes increasing temperatures as well as shifting reaction front in Fig. 9. Therefore, we can not study mass transfer limitations with the current experimental set – up.

One way to solve this problem is to dilute the catalyst (powder catalyst such as Pt-BHA) with inert material (i.e. SiO₂ or SiC) and also dilute the fed reactants CH₄ / O₂ with inert gas (i.e. N₂). Then we may obtain isothermal reactor operations for CPOM which is applicable for mass transfer limitation studies.

6.2.2 Higher weight loading oxygen carriers

During the synthesis of nanocomposite oxygen, we found that the maximum metal weight loading is limited to 40wt%. However, for the application as CLC oxygen carriers, there are situations that demand higher weight loadings. Therefore, we need to increase the metal loading.

We will try the synthesis in two ways:

(1) Tailoring the BHA material structure to incorporate more metal particles. In the nanocomposite oxygen carriers, metal particles are embedded in the ceramic BHA pore cages. By changing the support ceramic structure, i.e., increasing the pore cages, we may incorporate more particles into the matrix. This can be realized by changing the synthesis parameters, i.e., the water/surfactant ratio. Our current synthesis uses a fixed water/surfactant ratio at 94.8. It was found [61] that when the water to surfactant ratio is increased, the reverse-microemulsion system may change to a turbid emulsion and the synthesis result in ‘needle’ like BHA structure. The ‘needle’ like structure may incorporate more metal particles.

(2) Synthesizing SiO₂ based nanocomposite oxygen carriers. The molecular weight of SiO₂ is much lower than BHA. Therefore, with the same weight of support, SiO₂ can provide more pore cages, which can incorporate more nano-metal particles per unit weight support and hence higher weight loading oxygen carriers can be synthesized.

6.2.3 Integrating RFR concept with CLC

The original concept of CLC needs two reactors, an oxidizer and a reducer. The oxygen carriers are circulated between these two reactors. Asymmetric redox kinetics, agglomeration and sintering of the metal component, attrition of the metal support during solid transport are significant problems in practice. While using nanocomposite oxygen carriers can successfully overcome kinetic and sintering problems, solid transportation as well as related attrition issues remain big challenges.

In another hand, we have demonstrated the exceptional ability of heat integration in a RFR. We have also extended the reactor concept for the applications of CPOM to ATR and ODH of ethane to ethylene, demonstrating the flexibility of the concept. Here, we propose the

application of RFR principle for CLC, to combine heat and mass transfer in a single reactor tube. The RFR principle for CLC is shown in Fig. 49. In this concept, instead of transporting the oxygen carrier between different reactors, a stationary fixed bed with oxygen carriers is exposed to temporally alternating gas flow of air (top) and fuel (bottom). To achieve heat-integration, the gas flow is switched with the gas feed and the fixed bed is surrounded by inert zones for heat storage and release. This concept could in principle avoid the circulation of solid oxygen carriers and thereby attrition problems and associated heat loss during solid transportation.

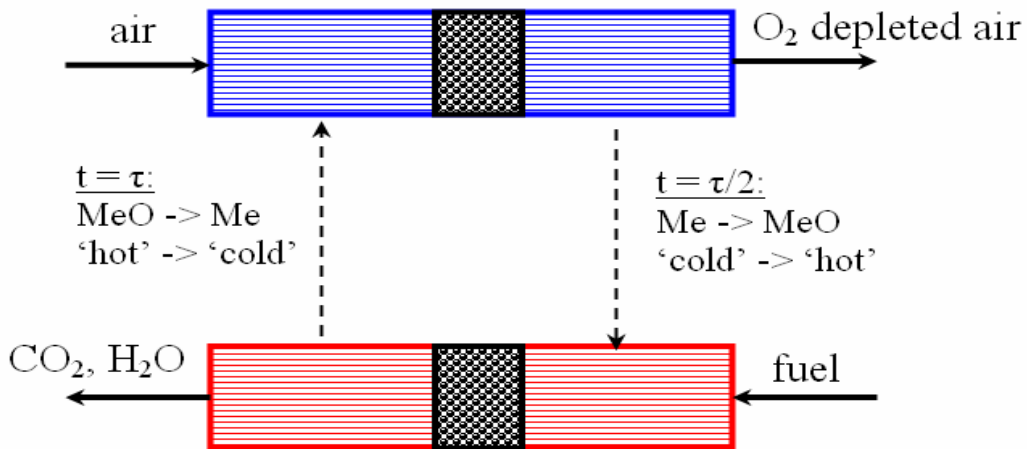


Figure 49. Principle of RFR_CLC.

APPENDIX A

CATALYST PREPARATION FOR CPOM / ATR

The catalyst substrate were α - Al₂O₃ foam monoliths (Vesuvius High – Tech Ceramics) or cordierite monolith (Corning Inc.). The substrates were shaped into cylinders with 17 mm diameter and 10 mm length. Different length (2mm, 5mm and 10 mm) substrates were prepared during mechanism studies.

The substrates were coated with Pt or Ni using standard impregnation procedures as listed in the following:

(1) The surface of the monolith is cleaned of any residuals by flaming it for several minutes.

(2) The cold monolith is impregnated with 10 wt% metal salt solution (H₂PtCl₆ for Pt, (C₂H₃O₂)₂Ni for Ni, both from Sigma-Aldrich, using de-ionized water).

(3) The coated monolith is dried in an oven at 120°C overnight to remove water.

(4) The catalyst is then reduced in an oven at 280°C – 600°C in a 5mol% H₂/N₂ stream for 5 hours.

The impregnation and calcinations procedure typically results in a thin metal coating on the monolith with ~ 2 – 4 wt%.

APPENDIX B

NANOCOMPOSITE OXYGEN CARRIER SYNTHESIS

Table 8. A typical recipe for Ni_BHA oxygen carrier synthesis. The synthesis results in 15.31 wt% (theoretical) NiO loading.

<u>Microemulsion</u>		MW	moles	mass (g)	vol (ml)
PEPP	(surfactant)	2000.00	0.0075	15.0	--
Pentanol	(co-surfactant)	88.15	1.9853	175.0	214.7
Iso-octane	(oil phase)	114.23	0.3939	45.0	65.2
H ₂ O	(water)	18.00	0.7111	12.8	--
Ni(NO ₃) ₂ *6H ₂ O	(metal salt)	290.81	0.0050	1.454	--
<u>Metal Alkoxides</u>					
Al-Isopropoxide		204.24	0.0320	6.5360	--
Ba-Isopropoxide		255.51	0.0027	0.6822	--
Isopropanol		60.10	1.6328	98.13	125
BHA		765.10	0.0027	2.07	--
NiO loading	0.153119581				

APPENDIX C

CALCULATIONS OF CONVERSION AND SELECTIVITY FOR ATR AND CPOM

Methane conversion in general is defined as (all the species hereafter are based on molar amounts):

$$X_{CH_4} = \frac{CH_{4,in} - CH_{4,out}}{CH_{4,in}} \times 100\% \quad (C-1)$$

Since only CO, CO₂ and CH₄ contain carbon element, the above definition can be simplified into:

$$X_{CH_4} = \frac{CO_{out} + CO_{2,out}}{CO_{out} + CO_{2,out} + CH_{4,out}} \times 100\% \quad (C-2)$$

This definition obviates using the value of inlet molar amount of methane. Methane conversion is directly calculated based on the exit product gases concentrations that can be detected by GC.

For carbon cycle, the reactant is methane and products are CO and CO₂, hence the definition of CO selectivity is:

$$S_{CO} = \frac{CO_{out}}{CO_{out} + CO_{2,out}} \times 100\% \quad (C-3)$$

Therefore, CO selectivity can also be calculated directly from the exit product concentrations.

Hydrogen selectivity is different. The product hydrogen may have two sources: CH₄ and H₂O. The hydrogen selectivity based on the converted methane is defined as:

$$S_{H_2,CH_4} = \frac{H_{2,out}}{2(CH_{4,in} - CH_{4,out})} \times 100\% \quad (C-4)$$

We will keep using S_{H₂} for hydrogen selectivity based on methane, however, readers should be aware of the difference of hydrogen selectivity defined in CPOM, where:

$$S_{H_2} = \frac{H_{2,out}}{H_{2,out} + H_2O_{out}} \times 100\% \quad (C-5)$$

In fact, when the water addition in ATR is zero, (C-4) and (C-5) give exactly the same results. Corresponding to the definition of hydrogen selectivity, water conversion in ATR is defined as:

$$X_{H_2O} = \frac{H_2O_{in} - H_2O_{out}}{H_2O_{in}} \times 100\% \quad (C-6)$$

According to this definition, water conversion can be positive, negative or zero. When there is no water addition in the reactant gases, water conversion is negative infinity. Careful hydrogen atom balance reveals that whenever the water conversion is zero or above, which means the overall effect is that water is being consumed in ATR process, hydrogen selectivity will be above 100%. This indicates all the hydrogen atoms in the converted methane have turned into hydrogen gas and ATR starts to convert hydrogen atoms in water into hydrogen gas.

APPENDIX D

DERIVATION OF SHRINKING CORE MODEL

Consider: $A(g) + bB(s) = \text{Product}(g, s)$

General PDE for unsteady state diffusion:

$$\frac{\partial C}{\partial t} = D \nabla^2 C + R_v \quad (\text{D-1})$$

In spherical coordinates:

$$\frac{\partial C}{\partial t} = D \frac{1}{r^2} \frac{\partial}{\partial r} \left(r^2 \frac{\partial C}{\partial r} \right) + R_v \quad (\text{D-2})$$

$$\frac{\partial C}{\partial t} = D \left(\frac{\partial^2 C}{\partial r^2} + \frac{2}{r} \frac{\partial C}{\partial r} \right) + R_v \quad (\text{D-3})$$

In ash layer, for gaseous reactant A, no reaction:

$$D_e \left(\frac{\partial^2 c_A}{\partial r^2} + \frac{2}{r} \frac{\partial c_A}{\partial r} \right) = \frac{\partial c_A}{\partial t} \quad (\text{D-4})$$

Pseudo steady state, $c_A = c_A(r)$; therefore, the above PDE turns to ODE:

$$\left(\frac{d^2 c_A}{dr^2} + \frac{2}{r} \frac{dc_A}{dr} \right) = 0 \quad (\text{D-5})$$

Boundary conditions:

$r = R$ (initial radius), $N_A = D_e \left(\frac{\partial c_A}{\partial r} \right)_{r=R} = k_{Ag} (c_{Ag} - c_{As})$ or $c_A = c_{As}$

at $r = r_c$ (metal core), $N_A = D_e \left(\frac{\partial c_A}{\partial r} \right)_{r=r_c} = k_{As} c_{As}$ or $c_A = c_{Ac}$

Where k_{As} is the rate constant for the first-order surface reaction:

$$-R_A = 4\pi r_c^2 k_{As} c_{As} = 4\pi r_c^2 (-r_{As}) \quad (D-6)$$

Solve ODE (D-5), let $y = dc_A/dr$, integrate (D-5) once, we get:

$y = \frac{dc_A}{dr} = \frac{2}{r^2} C_1$, where C_1 is the integration constant; applying boundary condition:

$$N_A = D_e \left(\frac{\partial c_A}{\partial r} \right)_{r=R} = k_{Ag} (c_{Ag} - c_{As}) \quad (D-7)$$

we get $C_1 = \frac{R^2 k_{Ag}}{De} (C_{Ag} - C_{As})$, therefore:

$$\frac{dc_A}{dr} = \frac{k_{Ag} R^2}{De} (c_{Ag} - c_{As}) \frac{1}{r^2} \quad (D-8)$$

Integrate (D-8), applying boundary condition at $r=r_c$, $c_A = c_{Ac}$ we get:

$$c_A = c_{Ac} + \frac{k_{Ag} R^2}{De} (c_{Ag} - c_{As}) \left(\frac{1}{r_c} - \frac{1}{r} \right) \quad (D-9)$$

Applying (D-8) at the surface of the core ($r = r_c$), together with boundary condition $N_A = D_e \left(\frac{\partial c_A}{\partial r} \right)_{r=r_c} = k_{As} c_{As}$, at $r = r_c$ we obtain one expression for c_{As} in terms of c_{Ac} :

$$c_{As} = c_{Ag} - (k_{As} r_c^2 / k_{Ag} R^2) c_{Ac} \quad (D-10)$$

Similarly, for equation (D-9), together with boundary condition $r = R$, $c_A = c_{As}$, we obtain another expression:

$$c_{As} = c_{Ac} + \frac{k_{Ag} R^2}{De} (c_{Ag} - c_{Ac}) \left(\frac{1}{r_c} - \frac{1}{R} \right) \quad (D-11)$$

From (D-10) and (D-11), eliminate c_{As} , and substitute resulting c_{Ac} into (D-6), we obtain:

$$(-R_A) = \frac{4\pi c_{Ag}}{\frac{1}{k_{Ag} R^2} + \frac{R - r_c}{De R r_c} + \frac{1}{k_{As} r_c^2}} \quad (D-12)$$

Keep in mind that, A is the reactant gas.

Now, consider reactant B (solid):

$$(-R_B) = -\frac{dn_B}{dt} = -\frac{d}{dt} \left(\rho_{Bm} \frac{4}{3} \pi r_c^3 \right) = -4\pi \rho_{Bm} r_c^2 \frac{dr_c}{dt} \quad (D-13)$$

Where ρ_{Bm} is the molar density of solid B (mole/m³).

The relation of R_A and R_B is:

$$(-R_B) = b(-R_A) \quad (D-14)$$

We obtain:

$$dt = -\frac{\rho_{Bm} R}{bc_{Ag}} \left[\frac{r_c^2}{k_{Ag} R^2} + \frac{1}{De} \left(r_c - \frac{r_c^2}{R} \right) + \frac{1}{k_{As}} \right] dr_c \quad (D-15)$$

Integration of equation (D-15), from $t = 0$, $r_c = R$, to t , r_c , results in:

$$t = \frac{\rho_{Bm} R}{bc_{Ag}} \left\{ \frac{1}{3k_{Ag}} \left[1 - \left(\frac{r_c}{R} \right)^3 \right] + \frac{R}{6De} \left[1 - 3 \left(\frac{r_c}{R} \right)^2 + 2 \left(\frac{r_c}{R} \right)^3 \right] + \frac{1}{k_{As}} \left(1 - \frac{r_c}{R} \right) \right\} \quad (D-16)$$

Based on the shrinking volume of a sphere, conversion x_B is defined as:

$$X_B = \frac{n_{B0} - n_B}{n_{B0}} = 1 - \left(\frac{r_c}{R} \right)^3 \quad (D-17)$$

Therefore, (16) can be re-written into:

$$t = \frac{\rho_{Bm} R}{bc_{Ag}} \left\{ \frac{X_B}{3k_{Ag}} + \frac{R}{6De} \left[1 - 3(1 - X_B)^{2/3} + 2(1 - X_B) \right] + \frac{1}{k_{As}} \left[1 - (1 - X_B)^{1/3} \right] \right\} \quad (D-18)$$

We may write equation (D-18) in this form:

$$t = [t(\text{external mass transfer control}) + t(\text{internal diffusion control}) + t(\text{reaction control})];$$

(D-19)

BIBLIOGRAPHY

- [1] T. Liu, V. Gepert, G. Veser, *Chem. Eng. Res. Des.* 83 (2005) 611.
- [2] F. Dautzenberg, M. Mukherjee, *Chem. Eng. Sci.* 56 (2001) 251.
- [3] D. Agar, *Chem. Eng. Sci.* 54 (1999) 1299.
- [4] A.P.E. York, T. Xiao, M.L.H. Green, *Topics in Catal.* 22 (2003) 345.
- [5] I. Wender, *Fuel Proc. Tech.* 48 (1996) 189.
- [6] M. Prettre, C. Eichner, M. Perrin, *Trans. Faraday Soc.* 43 (1946) 335.
- [7] M. Pena, J. Gomez, J. Fierro, *Appl. Catal. A: General* 144 (1996) 7.
- [8] S.C. Tsang, J.B. Claridge, M.L.H. Green, *Catal. Today* 23 (1995) 3.
- [9] A. Mitri, D. Neumann, T. Liu, G. Veser, *Chem. Eng. Sci.* 59 (2004) 5527.
- [10] U. Friedle, G. Veser, *Chem. Eng. Sci.* 54 (1999) 1325.
- [11] J. Frauhammer, G. Eigenberger, L. Hippel, D. Arntz, *Chem. Eng. Sci.* 54 (1999) 3661.
- [12] G. Kolios, J. Frauhammer, G. Eigenberger, *Chem. Eng. Sci.* 55 (2000) 5945.
- [13] D. Neumann, G. Veser, *AICHE J.* 51 (2005) 210.
- [14] D. Neumann, V. Gepert, G. Veser, *Ind. Eng. Chem. Res.* 43 (2004) 4657.
- [15] G. Veser, J. Frauhammer, *Chem. Eng. Sci.* 55 (2000) 2271.
- [16] P.M. Biesheuvel, G.J. Kramer, *AICHE J.* 49 (2003) 1827.
- [17] J. Schicks, D. Neumann, U. Specht, G. Veser, *Catal. Today* 81 (2003) 287.
- [18] D. Neumann, M. Kirchhoff, G. Veser, *Catal. Today* 98 (2004) 565.
- [19] D.A. Hickman, L.D. Schmidt, *J. Catal.* 138 (1992) 267.
- [20] G. Boreskov, Y. Matros, *Appl. Catal. A: General* 5 (1983) 337.
- [21] Y. Matros, G. Bunimovich, *Catal. Rev. Sci. Eng.* 38 (1996) 1.

- [22] U. Nieken, G. Kolios, G. Eigenberger, *Catal. Today* 20 (1994) 355.
- [23] M. Elsner, C. Dittrich, D. Agar, *Chem. Eng. Sci.* 57 (2002) 1607.
- [24] M. Elsner, M. Menge, C. Muller, D. Agar, *Catal. Today* 79 (2003) 487.
- [25] M. Ishida, H. Jin, *Energy* 19 (1994) 415.
- [26] M. Ishida, H. Jin, *Ind. Eng. Chem. Res.* 35 (1996) 2469.
- [27] J. Wolf, M. Anheden, J. Yan, *Fuel* 84 (2005) 993.
- [28] R. Villa, C. Cristiani, G. Groppi, L. Lietti, P. Forzatti, U. Cornaro, S. Rossini, *J. Mol. Catal. A: Chem.* 204 (2003) 637.
- [29] K. Song, Y. Seo, H. Yoon, S. Choi, *Korean J. of Chem. Eng.* 20 (2003) 471.
- [30] T. Mattisson, A. Jardnas, A. Lyngfelt, *Energy&Fuels* 17 (2003) 643.
- [31] M. Johansson, T. Mattisson, A. Lyngfelt, *Ind. Eng. Chem. Res.* 43 (2004) 6978.
- [32] T. Mattisson, M. Johansson, A. Lyngfelt, *Energy&Fuels* 18 (2004) 628.
- [33] P. Cho, T. Mattisson, A. Lyngfelt, *Fuel* 83 (2004) 1215.
- [34] T. Mattisson, M. Johansson, A. Lyngfelt, *Fuel* 85 (2006) 736.
- [35] L.D. Schmidt, M. Huff, *Catal. Today* 21 (1994) 443.
- [36] S.S. Bharadwaj, L.D. Schmidt, *Fuel Proc. Tech.* 42 (1995) 109.
- [37] P.D.F. Vernon, M.L.H. Green, A.K. Cheetham, A.T. Ashcroft, *Catal. Letters* 6 (1990) 181.
- [38] W.J.M. Vermieren, E. Blomsma, P.A. Jacobs, *Catal. Today* 13 (1992) 427.
- [39] K. Heitnes, S. Lindberg, O.A. Rokstad, A. Holmen, *Catal. Today* 21 (1994) 471.
- [40] K. Heitnes, S. Lindberg, O.A. Rokstad, A. Holmen, *Catal. Today* 24 (1995) 211.
- [41] D.A. Hickman, L.D. Schmidt, *Science* 259 (1993) 343.
- [42] O. Deutschmann, L.D. Schmidt, *AICHE J.* 44 (1998) 2465.
- [43] L.L. Raja, R.J. Kee, O. Deutschmann, J. Warnatz, L.D. Schmidt, *Catal. Today* 59 (2000) 47.
- [44] M. Bizzi, G. Saracco, R. Schwiedernoch, O. Deutschmann, *AICHE J.* 50 (2004) 1289.

- [45] P.A. Bui, D.G. Vlachos, P.R. Westmoreland, *Surf. Sci.* 385 (1997) L1029.
- [46] P. Aghalayam, Y.K. Park, D.G. Vlachos, *AICHE J.* 46 (2000) 2017.
- [47] C.T. Goralski, R.P. O'Connor, L.D. Schmidt, *Chem. Eng. Sci.* 55 (2000) 1357.
- [48] K. Heitnes, T. Sperle, O.A. Rokstad, A. Holmen, *Catal. Letters* 45 (1997) 97.
- [49] K. Heitnes, O.A. Rokstad, A. Holmen, *Catal. Letters* 36 (1996) 25.
- [50] M. Annaland, R. Nijssen, *Chem. Eng. Sci.* 57 (2002) 4967.
- [51] B. Glockler, G. Kolios, G. Eigenberger, *Chem. Eng. Sci.* 58 (2003) 593.
- [52] D. Goodwin, www.cantera.org (2003).
- [53] J. Nielsen, *Catal. Today* 19 (1993) 305.
- [54] J. Nielsen, *Catal. Today* 71 (2002) 243.
- [55] S. Chattopadhyay, G. Veser, *AICHE J.* 52 (2006) 2217.
- [56] A. Bell, *Science* 299 (2003) 1688.
- [57] G. Somorjai, Y. Borodko, *Catal. Letters* 76 (2001) 1.
- [58] M. Kirchhoff, U. Specht, G. Veser, *Nanotechnology* 16 (2005) S401.
- [59] R. Missen, C. Mims, B. Saville, John Wiley & Sons, Toronto, (1998).
- [60] I. Gallino, Oregon State University (2003).